PNAS
www.pnas.org

Supplementary Information for

STRUCTURAL DETERMINANTS OF PROTOCADHERIN-15 MECHANICS AND FUNCTION IN HEARING AND BALANCE PERCEPTION

Deepanshu Choudhary[a 1], Yoshie Narui[a 1], Brandon L. Neel[a,b 1], Lahiru N. Wimalasena[a], Carissa F. Klanseck[a], Pedro De-la-Torre[a], Conghui Chen[a], Raul Araya-Secchi[a,c], Elakkiya Tamilselvan[a,d], and Marcos Sotomayor[a,b,d] *

[a] Department of Chemistry and Biochemistry, The Ohio State University
484 W 12th Avenue, Columbus, OH 43210

[b] The Ohio State Biochemistry Program, The Ohio State University
484 W 12th Avenue, Columbus, OH 43210

[c] Niels Bohr Institute, University of Copenhagen, 2100 Copenhagen, Denmark

[d] Biophysics Program, The Ohio State University
484 W 12th Avenue, Columbus, OH 43210

[1] Co-first authors.

* Corresponding author: Marcos Sotomayor.

Email: sotomayor.8@osu.edu

This PDF file includes:

Supplementary text (Methods, Note 1, Note 2, Note 3, Note 4)
Figures S1 to S16
Tables S1 to S10
Legends for Movies S1 to S13
SI References

Other supplementary materials for this manuscript include the following:

Movies S1 to S13

www.pnas.org/cgi/doi/10.1073/pnas.1920444117

Supplementary Information Text

METHODS

Expression and purification of bacterially expressed PCDH15 fragments

Mus musculus (*mm*) and *Homo sapiens* (*hs*) DNA sequences encoding for protein fragments *mm* PCDH15 EC1-2, *hs* PCDH15 EC1-3, *hs* PCDH15 EC1-4 without exon 12a (ex12a-), *mm* CDH23 EC1-2, *hs* PCDH15 EC2-3, *hs* PCDH15 EC3-5 ex12a-, *mm* PCDH15 EC7-8, and *mm* PCDH15 EC9-MAD12 were subcloned into *NdeI* and *XhoI* sites of the pET21a vector. Similarly, *NheI* and *XhoI* sites were used for fragments *mm* PCDH15 EC4-7, EC5-7, and EC6-7. All bacterial constructs had a starting methionine residue and lacked the native signal peptide. Residue numbering in the text and structures corresponds to processed proteins without signal peptide (starting methionine residue is labeled M0). All engineered missense mutations were generated using the QuikChange Lightning mutagenesis kit (Agilent). Insertions of a biotin acceptor peptide (BAP) sequence (p.GLNDIFEAQKIEWHE) at the end of *mm* PCDH15 EC1-2BAP and of exon 12a (p.VPPSGVP) within *hs* PCDH15 EC3-5 (ex12a+) were carried out using standard protocols. All DNA constructs were sequence verified. Protein fragments were expressed in *Escherichia coli* BL21 (Agilent), BL21 CodonPlus(DE3)-RIPL (Agilent), or BL21 Rosetta(DE3) (Novagen) cells, which were cultured in LB or TB media, induced at OD_{600} ~0.6 with 200 μM or 1 mM IPTG and grown at 30°C or 37°C for ~16 h (*SI Appendix*, Table S3). Cells were lysed by sonication in denaturing buffer (20 mM Tris HCl, pH 7.5, 6 M guanidine hydrochloride, 10 mM $CaCl_2$, and 20 mM imidazole). The cleared lysates were loaded onto Ni-Sepharose (GE Healthcare), eluted with denaturing buffer supplemented with 500 mM imidazole and refolded as indicated in *SI Appendix,* Table S3 using MWCO 2000 membranes (Spectra/Por) when applicable. Prior to starting refolding reactions, elution solutions for some PCDH15 fragments were diluted to ~0.5 mg/mL using the denaturing buffer, and then reduced by adding 2 mM DTT to the diluted sample (*hs* PCDH15 EC2-3 WT and mutants, *hs* PCDH15 EC1-3 WT and mutants, *hs* PCDH15 EC1-4 ex12a- WT and mutants, *hs* PCDH15 EC3-5 ex12a+ WT). Refolded proteins were concentrated using Vivaspin 20 or Amicon 15 centrifugal concentrators (10 kDa molecular weight cutoff) and further purified on Superdex S75 or S200 columns (GE Healthcare) in size exclusion chromatography (SEC) buffer as indicated in *SI Appendix,* Table S3. The *hs* PCDH15 EC1-4 ex12a- and *hs* PCDH15 EC1-3 fragments (WT and variants) were concentrated to < 10 mg/mL using Amicon 15 concentrators before purification through SEC. Pure fractions of *hs* PCDH15 EC1-3 G16D/N369D/Q370N and *mm* CDH23 EC1-2 T15E were mixed with about two times molar excess of *mm* CDH23 EC1-2 T15E. The mixture was concentrated and then purified in 20 mM HEPES pH 7.5, 150 mM KCl, and 2 mM $CaCl_2$. All protein samples were concentrated by ultrafiltration to > 1 mg/ml for crystallization or biochemical assays, including multi-angle light scattering (MALS), sedimentation velocity analytical ultracentrifugation (SV-AUC), and small angle X-ray scattering (SAXS) experiments.

Expression and purification of mammalian expressed PCDH15 fragments

Mouse PCDH15 EC1-MAD12 ex12a- (p.Q1 to p.G1327), EC1-3 (p.Q1 to p.N369), EC1-4 ex12a- (p.Q1 to p.N491), and EC9-MAD12 (p.M905 to p.E1360) were subcloned into a pHis-N1 vector (a modified version of the pEGFP-N1 vector from Clontech where the EGFP has been substituted for a hexahistidine tag) using *XhoI* and *KpnI* sites. The native signal sequence was included before the start of EC1 and EC9, mutation p.V250N was introduced in EC1-4 using the QuikChange Lightning mutagenesis kit (Agilent), and all constructs were sequence verified. All protein fragments were expressed by transient transfection of Expi293 cells using ExpiFectamine. After 4-5 days of expression, the conditioned media (CM) was collected and dialyzed overnight against 20 mM Tris HCl, pH 7.5, 150 mM KCl, 50 mM NaCl, and 10 mM $CaCl_2$ to remove EDTA. The CM was concentrated using Amicon 10 kD or 30 kD concentrators and incubated with Ni-Sepharose beads for 1 h. The beads were washed 3 times with 20 mM Tris HCl, pH 8.0, 300 mM NaCl (200 mM NaCl for *mm* PCDH15 EC1-MAD12 ex12a-), 10 mM $CaCl_2$, and 20 mM imidazole, and the target protein was eluted with the same buffer containing 500 mM imidazole. The *mm* PCDH15 EC9-MAD12 protein was further purified on a Superdex S200 16/600 column in 20 mM Tris HCl, pH 7.5, 150 mM KCl, 50 mM NaCl, and 2 mM $CaCl_2$ and concentrated to 8 mg/mL for crystallization. The *mm* PCDH15 EC1-3 and *mm* PCDH15 EC1-4 (wild-type [WT] and p.V250N) protein fragments were purified using the same procedure and concentrated for SEC coupled to MALS analyses. Last, the *mm* PCDH15 EC1-MAD12 ex12a- protein was purified on a Superose 6 10/300 column in 20 mM Tris HCl, pH 8.0, 150 mM KCl, and 5 mM $CaCl_2$ and concentrated for SEC-MALS.

Crystallization and structure determination

Crystals were grown by vapor diffusion at 4°C by mixing protein and reservoir solutions as indicated (*SI Appendix*, Table S4). Cryoprotection buffers were prepared as indicated in *SI Appendix* Table S4. All crystals were cryo-cooled in liquid N_2. X-ray diffraction data sets were collected as indicated in *SI Appendix,* Table S1 and processed with HKL2000 (1). Structures were determined by molecular replacement using PHASER (2). The structure of *mm* PCDH15 EC1-2BAP was solved using repeats EC1-2 from *mm* PCDH15 in the handshake complex with *mm* CDH23 EC1-2 (PDB: 4APX) (3). The *mm* PCDH15 EC1-2 + CDH23 EC1-2 complex (PDB: 4APX) (3) and the *hs* PCDH15 EC2-3 WT fragment (see below) were used to solve the *hs* PCDH15 EC1-3

G16D/N369D/Q370N structure, which was used in combination with the *mm* PCDH15 EC1-2 + CDH23 EC1-2 complex (PDB: 4AQ8) (3) to solve the structure of the heterotetrameric complex *hs* PCDH15 EC1-3 G16D/N369D/Q370N + *mm* CDH23 EC1-2 T15E. Refinement of this heterotetrameric structure used the amplitude-based "Twin Refinement" option in REFMAC5 after achieving an R_{free} value of ~32%. The *hs* PCDH15 EC2-3 WT structure was solved using repeat EC2 from *mm* PCDH15 in the handshake complex with *mm* CDH23 EC1-2 (PDB: 4APX) and EC3 from *hs* PCDH15 EC3-5 ex12a- (PDB: 5T4M) (4), and subsequently used to solve for *hs* PCDH15 EC2-3 V250N. The *hs* PCDH15 EC3-5 ex12a+ structure was solved using *hs* PCDH15 EC3-5 ex12a- (PDB: 5T4M) (4). Refinement of this structure used the amplitude-based "Twin Refinement" option in REFMAC5 after achieving an R_{free} value of ~27%. Initial search models for *mm* PCDH15 EC4-7 were individual EC4 and EC5 repeats from *hs* PCDH15 EC3-5 ex12a- (PDB: 5T4M) (4), and EC7 from *mm* PCDH15 EC7-8 V875A. The *mm* PCDH15 EC5-7 structure was solved using individual EC repeats from *mm* PCDH15 EC4-7. Mouse PCDH15 EC6-7 was solved using EC7 from *mm* PCDH15 EC7-8 V875A as an initial search. The *mm* PCDH15 EC9-MAD12 structure was solved using *Sus scrofa* (*ss*) PCDH15 EC10-MAD12 (PDB: 6BXZ) (5) and *hs* PCDH15 EC8-10 (PDB: 4XHZ) (6). Model building was done with COOT (7) and restrained refinement was performed with REFMAC5 (8) as indicated in the deposited structures. Data collection and refinement statistics are provided in *SI Appendix*, Table S1. Structures were further analyzed using Procheck (9), Whatcheck (10), and Checkmymetal (11) prior to deposition.

Omit maps

Calculation of the composite omit maps for the heterotetrameric *hs* PCDH15 EC1-3 G16D/N369D/Q370N + *mm* CDH23 EC1-2 T15E structure was carried out using the deposited coordinate and map coefficients files and with simulated annealing. The annealing was performed using default parameters, on the entire protein chain, and at an annealing temperature of 5000 K using the 'Composite omit map' program from the Phenix suite. The $2mF_o$-DF_c composite omit map is shown in Fig. S7 *B and C*.

Assignment of crystallographic ions

Inspection of 2Fo-Fc electron density maps during initial stages of refinement depicted positive electron densities at sites 1, 2, and 3 of the linker regions in all structures with the exception of *hs* PCDH15 EC1-3 G16D/N369D/Q370N (missing density at the EC2-3 site 1 in both chains), *hs* PCDH15 EC1-3 G16D/N369D/Q370N + *mm* CDH23 EC1-2 T15E (missing density at the EC2-3 site 1 in both PCDH15 chains), *hs* PCDH15 EC2-3 (missing density at the EC2-3 site 1 of all four chains), *hs* PCDH15 EC3-5 ex12a+ (missing density at the EC3-4 site 1 of all chains and at site 2 of chain C), *mm* PCDH15 EC4-7 (missing density at sites 1 and 2 of EC5-6 linker regions), *mm* PCDH15 EC5-7 I582T (missing density at sites 1 and 2 of EC5-6 linker regions), and *mm* PCDH15 EC9-12 (missing density at EC9-10 and EC11-12 linker regions). Unassigned densities at sites 1, 2, and 3 at the EC repeat linker regions were all initially modeled as Ca^{2+} ions and validated in all structures based on compatibility with the final 2Fo-Fc map, an analysis of distances to coordinating atoms, and an evaluation of B factor values of the ion and surrounding residue atoms. However, there were a few cases in which assignment was difficult:

1) As opposed to the WT, site 1 at the *hs* PCDH15 EC2-3 V250N linker region has positive Fo-Fc density. We tried to assign a Mg^{2+} ion given that the crystallization condition had 150 mM $MgCl_2$, but it resulted in a positive Fo-Fc density near the ion after subsequent refinement by REFMAC. Thus, this site was assigned to a Ca^{2+} ion, which was more compatible with the 2Fo-Fc and Fo-Fc electron density maps.

2) In the *hs* PCDH15 EC3-5 ex12a+ structure, initial assignment of Ca^{2+} at site 2 of the EC3-4 linker region of chain A resulted in a positive value of the Fo-Fc density at the location of the ion. The protein solution buffer had 5 mM $CaCl_2$ and 50 mM NaCl while the crystallization buffer had 200 mM LiCl. Thus, we tried placing a Li^+ ion, which resulted in a large positive value of Fo-Fc density at the site of the ion. In contrast, Na^+ at the location was compatible with the 2Fo-Fc and Fo-Fc electron density maps, its B factor was similar to that of surrounding atoms, and it is also the cation with the closest ionic radius to Ca^{2+}. Thus, a Na^+ ion was placed at this site in the final model for the structure (*SI Appendix,* Fig. S8*B*).

3) In the *mm* PCDH15 EC4-7 structure, the EC4-5 linker initially had a Ca^{2+} assigned at site 2, but the B factor was large compared to surrounding atoms. The protein purification buffer contained 20 mM Tris HCl, pH 8.0, 150 mM NaCl, 50 mM KCl, and 2 mM $CaCl_2$, while the crystallization buffer had 2.0 M magnesium acetate. The Ca^{2+} ion was first replaced by a Mg^{2+} ion but the B factor was still significantly larger than surrounding atoms. The Mg^{2+} ion was replaced by a K^+ ion, which was in good agreement with the 2Fo-Fc and Fo-Fc electron density maps and had a B factor value similar to local atoms. The K^+ ion was kept at site 2 in the EC4-5 linker in the final model.

4) In the *mm* PCDH15 EC6-7 structure, initial assignment of Ca^{2+} at site 1 of the EC6-7 linker resulted in a positive value of the Fo-Fc density at the location of the ion. Since the purification buffer contained 50 mM KCl, we tried placing a K^+ ion, which was compatible with the 2Fo-Fc and Fo-Fc electron density maps and its B factor was similar to that of surrounding atoms. Thus, the K^+ ion was kept at this site in the final model.

Positive electron density was also observed in partial linker regions at protein fragments ends. These sites were assigned to Ca^{2+} ions in all cases (*mm* PCDH15 EC5-7 I582T, site 3 of EC4-5 partial linker region; *mm* PCDH15 EC7-8 V875A, site 3 of EC6-7 partial linker region; *mm* PCDH15 EC9-MAD12, site 3 of EC8-9 partial linker region).

Structural modeling of protein residues with poor electron density

Protein chains were generally modeled using a cutoff of 1.5 rmsd for the contour level of the 2Fo-Fc map in COOT. In some loops, weak electron density was observed at a contour level of 1 rmsd, which allowed us to fit the residues in the density, but resulted in higher B-factor values for those regions. In some of our structures we observed no density for the N- and C- terminal loops even at a contour level of 0.5 rmsd. Such regions of the protein were not built. In addition, some regions of our structures did not have clear density and were not built either. Missing residues in our models include: 1) the cysteine loop, parts of the AB loop containing a 3_{10} helix and the EF loop in EC3 of the *hs* PCDH15 EC1-3 G16D/N369D/Q370N structure; 2) β-strands F and G on both of the CDH23 EC2 repeats and the BC loop of PCDH15 EC1 in chain A of the *hs* PCDH15 EC1-3 G16D/N369D/Q370N + *mm* CDH23 EC1-2 T15E structure; 3) the BC loop in EC2 of all four monomers and the FG loop in EC2 in three of the monomers (A, B, and C) in the *hs* PCDH15 EC2-3 structure; 4) the cysteine loop in EC3, the BC loop in EC2, and the FG loop in EC2 in both chains of the *hs* PCDH15 EC2-3 V250N structure; 5) the BC loop of EC3 in all monomers and the EC5 β-strand A along with the connecting AB loop in chain C of the *hs* PCDH15 EC3-5 ex12a+ structure; 6) the BC loop of EC4 in the *mm* PCDH15 EC4-7 structure; 7) the EF loop of EC8 in the *mm* PCDH15 EC7-8 V875A structure.

SEC-MALS

SEC-MALS experiments were done using an ÄKTAmicro system connected in series with a Wyatt miniDAWN TREOS system. Protein samples of *hs* PCDH15 EC2-3 (> 1 mg/mL) were separated on a Superdex S75 3.2/30 column in 20 mM Tris HCl, pH 8.0, 150 mM KCl, 50 mM NaCl and 2 mM $CaCl_2$.

Bacterially produced protein samples of *hs* PCDH15 EC1-3 and EC1-4 were concentrated to > 1 mg/mL and separated on a Superdex S200 3.2/3.0 column in 20 mM HEPES pH 7.5, 150 mM KCl, and 2 mM $CaCl_2$ for WT or 20 mM Tris HCl, pH 8.0, 150 mM KCl, 50 mM NaCl, and 2 mM $CaCl_2$ for p.L306N/V307N. Mammalian expressed protein fragments of *mm* PCDH15 EC1-3 and EC1-4 ex12a- (WT and p.V250N) at concentrations > 1 mg/mL were separated on a Superdex S200 3.2/3.0 column in 20 mM Tris HCl, pH 8.0, 150 mM KCl, 50 mM NaCl and 2 mM $CaCl_2$. Mammalian expressed *mm* PCDH15 EC1-MAD12 ex12a- (~1.3 mg/mL) was separated on a Superose 6 3.2/30 column in 20 mM Tris HCl, pH 8.0, 150 mM KCl, with either 5 mM $CaCl_2$ or 5 mM EDTA. Absorbance at 280 nm and light scattering were monitored. The scattering information was subsequently converted into molecular weight using a rod-like model (*SI Appendix*, Table S5). The SEC-MALS curves were adjusted for connecting tubing length before plotting. Measurements listed in *SI Appendix* Table S5 were taken from distinct samples.

SAXS

Data from SAXS experiments after SEC were collected at the SIBYLS beamline 12.3.1 in the Advanced Light Source facility (Berkeley, CA) as described (12, 13) (*SI Appendix,* Table S7). A bacterially produced and purified sample of *mm* PCDH15 EC9-MAD12 was used along with an Agilent 1260 series HPLC and a Shodex KW-803 analytical column for data collection at a flow rate of 0.5 ml/min at 20°C (20 mM Tris HCl, pH 8.0, 150 mM KCl, 5 mM $CaCl_2$, and 1 mM TCEP). X-ray exposures lasting 3 s were collected continuously during a ~40 min elution. SAXS frames recorded prior to the protein elution peak were used to subtract all other frames. Buffer subtraction and data reduction was performed at the beamline with SCÅTTER (14).

Further data analysis of the merged SAXS data was carried out with PRIMUS (15) and the ATSAS program suite (16). Estimates of the radius of gyration (R_g) from the Guinier region were measured with PRIMUS. Maximum dimension (D_{max}) of particles was estimated from an indirect Fourier transform of the SAXS profiles using GNOM (17). Values of D_{max} between 140 and 160 Å provided the best solutions. The oligomeric state of the sample was assessed by estimating its molecular weight using the method implemented in the SAXSMoW2 server (18). Search of conformational changes of the dimeric structure in solution was performed by normal modes analysis with SRFLEX (19) using the crystal structure of *mm* PCDH15 EC9-MAD12 (PDB: 6EET) as

starting model. Model scattering intensities were computed from *mm* PCDH15 EC9-MAD12 (PDB: 6EET) and fitted to the experimental SAXS data using FoXS (20).

AUC

Sedimentation velocity AUC experiments were performed in a ProteomeLab XL-I analytical ultracentrifuge (Beckman Coulter) following standard procedures (21–23). Briefly, SEC purified protein samples were loaded into AUC cell assemblies with Epon centerpieces and 12 mm path length. To achieve chemical and thermal equilibrium, the An-50 TI rotor with loaded samples was allowed to equilibrate for ~2 h at 20°C in the centrifuge. The rotor was spun at 50,000 rpm and data was collected using absorption optics. Data analysis was performed with the software SEDFIT (http://sedfitsedphat.nibib.nih.gov), using a continuous sedimentation coefficient distribution model *c*(*S*). Standard values for buffer viscosity (0.01002 poise), density (1 g/ml) and partial specific volume (0.73 ml/g) were used, and confidence level was set to 0.68 as routinely done. The obtained *c*(*S*) distribution was loaded in GUSSI (24). All experiments were done in duplicates from distinct samples. Data was normalized by area under the curve.

Simulated systems

The psfgen, solvate, and autoionize VMD (25) plugins were used to build eleven molecular systems for molecular dynamics (MD) simulations (systems S1 to S11 in *SI Appendix,* Table S10). The *hs* PCDH15 EC1-MAD12 ex12a- + CDH23 EC1-2 model (1,547 residues, ~171.8 kDa, system S1 *hs* heterodimer) was built from fragments *mm* PCDH15 EC1-2 (PDB: 4APX) (3), *hs* PCDH15 EC2-3 (chain D), *hs* PCDH15 EC3-5 ex12a- (PDB: 5T4M, chain A) (4), *mm* PCDH15 EC4-7, *mm* PCDH15 EC7-8 V875A, *hs* PCDH15 EC8-10 (PDB: 4XHZ) (6), and *ss* PCDH15 EC10-MAD12 (PDB: 6BXZ, chain C) (5) as indicated in *SI Appendix,* Table S8 and Fig. S11 *A*-*K*. The *mm* PCDH15 EC1-MAD12 ex12a+ + CDH23 EC1-3 model (1,665 residues, ~184.4 kDa, system S2 *mm* heterodimer) was built from fragments *hs* PCDH15 EC1-3 G16D/N369D/Q370N + *mm* CDH23 EC1-2 (chains B & C, respectively), *hs* PCDH15 EC3-5 ex12a+ (chain B), *mm* PCDH15 EC4-7, *mm* PCDH15 EC7-8 V875A, hs PCDH15 EC8-10 (PDB: 4XHZ) (6), *mm* PCDH15 EC9-MAD12, and *Danio rerio* (*dr*) CDH23 EC1-3 (PDB: 5W4T, chain A) (26) as indicated in *SI Appendix,* Table S8 and Fig. S11 *L*-*V*. The *hs* (PCDH15 EC1-5 ex12a-)$_2$ + (CDH23 EC1-2)$_2$ model (1,587 residues, ~176.6 kDa, system S3 *hs* short tetramer 3 Ca^{2+} / linker) was built from crystal structures of *mm* PCDH15 EC1-2 (PDB: 4APX) (3), *hs* PCDH15 EC2-3 (chain D), and *hs* PCDH15 EC3-5 ex12a- (PDB: 5T4M, chain A) (4). The *mm* (PCDH15 EC1-5 ex12a+)$_2$ + (CDH23 EC1-3)$_2$ model (1,818 residues, ~201.7 kDa, system S7 *mm* short tetramer 3 Ca^{2+} / linker) was assembled using structures *hs* PCDH15 EC1-3 G16D/N369D/Q370N + *mm* CDH23 EC1-2, *hs* PCDH15 EC3-5 ex12a+ (chain B), and *dr* CDH23 EC1-3 (PDB: 5W4T, chain A) (26). All fragments were mutated so as to obtain a model of the species-specific WT proteins (*SI Appendix,* Table S8). The *hs* (PCDH15 EC1-5 ex12a-)$_2$ + *hs* (CDH23 EC1-2)$_2$ systems with less Ca^{2+} ions at the linker regions were built from the model with Ca^{2+}-saturated linkers by removing ions sequentially while maintaining charge neutrality of the systems (systems S4, S5, and S6 *hs* short tetramer with 2, 1, and 0 Ca^{2+} / linker, respectively).

The *hs* (PCDH15 EC1-MAD12 ex12a-)$_2$ + (CDH23 EC1-2)$_2$ tetramer system was assembled from the coordinates obtained from simulation trajectories as follows (*SI Appendix,* Fig. S14*F*; system S8 *hs* long tetramer 3 Ca^{2+} / linker). Chain A of *hs* PCDH15 used the coordinates from simulation S3c for residues 1-238 (chain A at 6.17 ns), whereas residues 239-485 came from simulation S3c (chain B at 6.17 ns), residues 486-1228 came from simulation S1d (118.342 ns), and residues 1229-1342 came from simulation S11c (chain A at 2.88 ns). Chain B of *hs* PCDH15 used the coordinates from simulation S3c for residues 1-367 (chain B at 6.17 ns), whereas residues 368-901 came from simulation S1d (7.057 ns), residues 902-1003 came from simulation S1d (8.332 ns), residues 1004-1126 came from simulation S1d (117.069 ns), and residues 1127-1342 came from simulation S11c (chain B at 2.88 ns). The *hs* (CDH23 EC1-2)$_2$ fragments came from simulation S3c (chains C & D at 6.17 ns).

The *mm* (PCDH15 EC1-MAD12 ex12a+)$_2$ + (CDH23 EC1-3)$_2$ tetramer system was assembled from the coordinates obtained from simulation trajectories and crystal structures as follows (*SI Appendix,* Fig. S14*G*; systems S9 and S10 *mm* long tetramer 3 Ca^{2+} / linker). Residues 3-116, 125-164, and 182-199 of CDH23 EC1-3 came from the crystal structure of *hs* PCDH15 EC1-3 G16D/N369D/Q370N + *mm* CDH23 EC1-2 (chains C and D), while residues 114-121(+3), 162-178(+3), and 197-315(+3) for both chain C and D came from the crystal structure of *dr* CDH23 EC1-3 (5W4T; chain A) (26). Residues 1-359 of chains A and B in the *mm* PCDH15 EC1-MAD12 ex12a+ model came from the crystal structure of *hs* PCDH15 EC1-3 G16D/N369D/Q370N + *mm* CDH23 EC1-2 (chains A and B), whereas residues 360-493 in chain A came from simulation S2b (chain A at 0.19 ns). Residues 494-600 in chain A of PCDH15 came from the equilibration simulation S2a at 2.502 ns, whereas residues 601-913 came from the constant velocity SMD simulation S2c at 1.1 ns, and residues 914-1348 came from the constant velocity SMD simulation S11d at 61.694 ns. Residues 360-369 in chain B of PCDH15 came

from the constant velocity SMD simulation S2b at 0.19 ns, whereas residues 370-495 came from the constant velocity SMD simulation S2b at 2.755 ns, residues 496-597 came from the equilibration simulation S2a at 4.182 ns, residues 598-800 came from constant velocity SMD simulation S2c at 8.1 ns, residues 801-911 come from constant velocity SMD simulation S2c at 9.24 ns, residues 912-1021 came from constant velocity SMD simulation S11d at 34.384 ns, and residues 1022-1348 came from constant velocity SMD simulation S11d at 61.694 ns. Coordinates for tetrameric complexes are available upon request.

All protein structures and models described above, along with crystallographic water molecules, had hydrogen atoms automatically added by psfgen. Residues D, E, K and R were assumed charged. Histidine residues were assumed neutral, and their protonation state was chosen to favor the formation of evident hydrogen bonds. Systems were solvated in explicit water, neutralized, and ionized with randomly placed ions so as to mimic a physiological endolymph environment with 150 mM KCl. The *mm* (PCDH15 EC1-MAD12 ex12a+)$_2$ + *mm* (CDH23 EC1-3)$_2$ tetramer was solvated in two different water boxes, a smaller elongated system for SMD (S9) and a larger system for long free-dynamics equilibrations (S10).

Computational modeling of systems with fewer bound Ca^{2+} ions

Tip links are found in fluid environments with low Ca^{2+}. In the cochlear endolymph, the bulk Ca^{2+} concentration ranges from 20 to 40 μM (27, 28) and the sub-tectorial space Ca^{2+} concentration possibly goes up to 300 μM (29). Vestibular endolymph Ca^{2+} concentration might range from 90 to 150 μM. Experimental measurements of *mm* CDH23 EC1-2 Ca^{2+}-binding affinities (30) suggest that sites 1, 2, and 3 at this canonical linker region have dissociation constants K_{D1} ~71 μM, K_{D2} ~44 μM, and K_{D3} ~5 μM, respectively. Dissociation constants for non-canonical linker regions in PCDH15 might be larger (4). Therefore, it is possible that some, or even all sites are not occupied by Ca^{2+} ions under some physiological conditions. In all cases, however, we expect that dissociation constants will follow the same trend with $K_{D1} > K_{D2} > K_{D3}$. Hence, to mimic low-Ca^{2+} conditions in simulations, we removed ions from binding sites sequentially. We removed first all the Ca^{2+} ions at site 1 to build the 2 Ca^{2+} system (simulations S4a-d). To build the 1 Ca^{2+} system (simulations S5a-d), the Ca^{2+} ions at site 1 and 2 were removed. Lastly, to build the 0 Ca^{2+} system, all Ca^{2+} ions were removed (simulations S6a-d; *SI Appendix,* Table S10).

MD simulations using NAMD

MD simulations were performed using NAMD 2.11, 2.12, and 2.13 (31), the CHARMM36 force field for proteins with the CMAP correction, and the TIP3P model for water (32). A cutoff of 12 Å (with a switching function starting at 10 Å) was used for van der Waals interactions. Periodic boundary conditions were used along with the Particle Mesh Ewald method to compute long-range electrostatic forces without cutoff and with a grid point density of >1 Å^{-3}. A uniform 2 fs integration time step was used together with SHAKE. Langevin dynamics was utilized to enforce constant temperature T = 300 K with a damping coefficient of 0.1 ps^{-1}, unless otherwise stated. Constant pressure simulations (*NpT*) at 1 atm were conducted using the hybrid Nosé-Hoover Langevin piston method with a 200 fs decay period and a 100 fs damping time constant.

Simulations and analysis tools

Each system was energy-minimized and equilibrated in the *NpT* ensemble, and the resulting state was used to perform subsequent equilibrium and SMD simulations (*SI Appendix,* Table S10). Constant-velocity stretching simulations used the SMD method and the NAMD Tcl forces interface (33–36), whereby Cα atoms of specific terminal residues were attached to independent virtual springs of stiffness k_s = 1 kcal mol^{-1} Å^{-2}. For SMD simulations of dimeric (simulations S11b-d) and heterotetrameric systems (simulations S3b-d, S4b-d, S5b-d, S6b-d, S7b-e, S8b-d, S9b-e), these springs were connected to virtual slabs attached to a third stretching spring (k_s = 1 kcal mol^{-1} Å^{-2}). For some SMD simulations of dimeric and heterotetrameric systems (simulations S2e-f and S9f-g) the center of mass (COM) of Cα atoms from *mm* PCDH15 MAD12 were attached to similar virtual springs (k_s = 1 kcal mol^{-1} Å^{-2}). The free ends of the stretching springs were moved away from the protein in opposite directions at a constant velocity. The stretching direction was set along the *x*-axis matching the vector connecting terminal regions of the proteins in the corresponding simulated complexes. Applied forces were computed using the extension of the virtual springs. Protein stiffness was computed through linear regression fits of force versus end-to-end distance plots. Maximum force peaks and their averages were computed from 50-ps running averages used to eliminate local fluctuations. The end-to-end distance in constant-velocity SMD simulations of systems S3 to S11 (*SI Appendix,* Table S10) was computed as the separation between the center-of-mass of the Cα atoms stretched on one end and the center-of-mass of the Cα atoms stretched in the opposite direction on the other end of the system. Principal axes of EC repeats were computed using the Orient VMD plugin. Sequence alignments were performed with MUSCLE. Plots and curve fits were prepared with Xmgrace. Molecular images were created with the molecular graphics program VMD (25). PCDH15 ectodomain sequences were compared among various species using data obtained from the NCBI protein database (*SI*

Appendix, Table S2). Ectodomain sequences equivalent to *hs* PCDH15 CD1-1 (without exon 12a, unless indicated) were split into their respective EC repeats prior to alignment, which was done using the ClustalW algorithm (37) within Geneious (38) to determine the percent sequence identity for each EC repeat (*SI Appendix*, Figs. S1 and S2*C*). Aligned sequences were loaded into JalView (39) and colored based on sequence conservation with a 45% conservation threshold. Comparison of EC repeats within the human PCDH15 protein was carried out by aligning individual EC repeats to each other using ClustalW on Geneious. The alignment (*SI Appendix,* Fig. S2*A*) was imported into the Sequence Identity and Similarity (SIAS) server (40) to obtain the sequence identity matrix in *SI Appendix,* Fig. S2*D*. Structural comparisons and computation of core RMSD were done using COOT (7).

DATA DEPOSITION AND AVAILABILITY

Coordinates for all structures presented here have been deposited in the Protein Data Bank with entry codes 6N22 (*mm* PCDH15 EC1-2BAP), 6MFO (*hs* PCDH15 EC1-3 G16D/N369D/Q370N), 6N2E (*hs* PCDH15 EC1-3 G16D/N369D/Q370N + *mm* CDH23 EC1-2 T15E), 5ULY (*hs* PCDH15 EC2-3), 6EB5 (*hs* PCDH15 EC2-3 V250N), 6E8F (*hs* PCDH15 EC3-5 ex12a+), 5W1D (*mm* PCDH15 EC4-7), 6BXU (*mm* PCDH15 EC5-7 I582T), 6BWN (*mm* PCDH15 EC6-7), 5TPK (*mm* PCDH15 EC7-8 V875A), and 6EET (*mm* PCDH15 EC9-MAD12). Other raw data and data sets generated and/or analyzed during the current study are available from the corresponding author on reasonable request.

NOTE 1: REFOLDING AND GLYCOSYLATION

Most of the protein fragments we used for structure determination were refolded from bacterial inclusion bodies. It is generally accepted, since Anfinsens's work (41), that when proteins are refolded into a single conformation, this conformation most likely represents the thermodynamically most stable, native fold of the protein. In the case of enzymes, measuring catalytic activity can directly test refolding success. Cadherins, however, are not enzymes, and a different set of criteria must be used to determine whether refolding results in a native state. We used SEC to test all our refolded protein fragments and worked with samples from single and well-defined (monodisperse) peaks, excluding any aggregates. A monodisperse SEC peak also suggests lack of multiple conformations. In addition, successful and reproducible crystallization, achieved for all our protein fragments, indicated highly homogenous samples. A comparison between refolded and native cadherin structures shows core RMSD values below 2.5 Å (*SI Appendix*, Table S11). These analyses included bacterially expressed and native *mm* CDH23 EC1-2 (3MVS) (42) compared to bacterially expressed and refolded *mm* CDH23 EC1-2 (2WHV; core RMSD 2.4 Å) (30) as well as native glycosylated *mm* PCDH15 EC1-3 (6CV7) (43) compared to our bacterially expressed and refolded *hs* PCDH15 EC1-3 G16D/N369D/Q370N in two structures (RMSDs of 1.7 Å for 6MFO and 1.5 Å for 6NE2). The small structural differences observed between these protein structures confirm that our cadherin refolding protocols result in native states.

Glycosylation in mammalian cells (absent in bacterially produced proteins) may also alter the structure of a protein and its native state, yet again a direct structural comparison between proteins produced in bacterial and mammalian expression systems reveals only minor differences (*SI Appendix*, Table S11). For instance, bacterially expressed and refolded *ss* PCDH15 EC10-MAD12 (6BXZ) compares well with the same fragment within the structure of the native glycosylated *mm* PCDH15 EC9-MAD12 (6EET; core RMSD 1.5 Å). Similarly, bacterially expressed and refolded *hs* PCDH1 EC1-4 (6BX7) (44) compares well with two structures of the same native glycosylated protein (6MGA and 6VFP; core RMSD of 0.7 Å for both) (44, 45). Glycosylation, however, can affect the oligomerization state and crystal packing of cadherin proteins (46). This might be especially important for the antiparallel *trans* and X-dimer configurations of PCDH15 EC1-3 G16D/N369D/Q370N, as discussed in the main text.

Interestingly, glycosylation is observed in our *mm* PCDH15 EC9-MAD12 structure at five sites, with O-linked sugars clearly discernible at residues p.S996, p.S998, and p.T1000 in EC9, and N-linked sugars at p.N1063 in EC10 and at p.N1154 in EC11 (Fig. 4 *C-E*; *SI Appendix,* Fig. S9). Glycosylation has also been observed in published structures at p.N1063 and p.N1154, but not at the other three sites (47). Clear electron density at additional glycosylation sites p.N1043 and p.S1141 (as seen in PDBs: 6C10 and 6C13) (47) is not present in our structure. While glycosylation at p.S1141 would sterically hinder the dimeric interface in one of the published PCDH15 structures (PDB: 6C13), none of the other modeled sugars in all available structures that cover this region interfere with bending and dimerization directly.

NOTE 2: DIMERIC CONFORMATION OF *mm* PCDH15 EC9-MAD12 IN SOLUTION

SAXS data can provide information about the size and shape of a protein in solution. The radius of gyration (R_g) of bacterially produced *mm* PCDH15 EC9-MAD12 from Guinier (R_g = 46.7 ± 2.9 Å) and SAXS profile analyses

(R_g = 47.3 ± 0.2 Å with maximum dimension D_{max} = 160 Å) are in excellent agreement with each other and with the R_g obtained from the *mm* PCDH15 EC9-MAD12 structure (R_g = 42.01 Å). These results further suggest that the overall shape of the dimer observed in the crystallographic structure is maintained in solution. However, comparison of the SAXS data to X-ray intensities modeled from the *mm* PCDH15 EC9-MAD12 crystal structure revealed some discrepancies reflected by a large χ^2 value obtained for the fitting (χ^2 = 6.52) and by a clear dip in the *q*-region 0.1 – 0.25 Å^{-1} observed in the modeled intensities but absent in the experimental data (*SI Appendix*, Fig. S10*A*). X-ray intensities calculated from models obtained using a normal-mode analysis (SREFLEX) (19) fit the experimental data better than the crystal structure (χ^2 = 1.38) and lack the dip in the *q*-region 0.1 – 0.25 Å^{-1} (*SI Appendix,* Fig. S10*A*). The best model shows changes in orientation and rotation of EC9 along with loss of symmetry (*SI Appendix,* Fig. 10*E*), consistent with asymmetry observed in SAXS-derived models of *ss* PCDH15 EC10-MAD12 (5). Analysis of the Kratky plot (*SI Appendix,* Fig. S10*D*) indicates that while the protein is folded in solution, there is significant flexibility. Overall, SAXS data strongly supports a dimeric conformation of *mm* PCDH15 EC9-MAD12 that is asymmetric and flexible in solution.

NOTE 3: MOLECULAR MECHANISMS OF INHERITED DEAFNESS

Our structural models of PCDH15 show the location of three segments that are deleted in individuals with inherited deafness and Usher syndrome. The first in-frame deletion (p.E272 to p.Q509; Fig. 5*I*) causes Usher syndrome (moderate to profound deafness, vestibular dysfunction, and impaired vision) and takes out a large part of EC3 (β-strands B to G), all EC4, and a short piece of EC5 (β-strand A). Such large protein deletion may cause misfolding and poor localization, although it is possible that the resulting protein product folds with a hybrid repeat formed by β-strand A of EC3 and β-strands B to G of EC5, thus shortening the ectodomain by two EC repeats. This shortened PCDH15 might be mechanically compromised and might be unable to form the X-dimer mediated by the EC2-EC3 linker region. A second in-frame deletion (p.G936-p.K982; Fig. 5*J*) causes deafness and vestibular dysfunction in mice (*Av*-6J) and takes out β-strands C, D, E, and part of β-strand F in EC9 (48, 49). However, functional tip links are observed in hair cells from these mice, suggesting that the protein product is properly folded and trafficked, but perhaps unstable (49). The last in-frame deletion involves elimination of a single residue (p.V767) (50), which results in non-syndromic deafness and might affect the register and stability of β-strand F in EC7, thus compromising the mechanical stability of PCDH15 (51), but not enough to alter vestibular function.

Missense mutations implicated in inherited deafness located throughout the PCDH15 ectodomain (15 sites) can be segregated in at least four groups (*SI Appendix,* Table S9). In the first one we included two mutations (p.I108N and p.R113G) that are known to interfere with the PCDH15-CDH23 handshake bond (3, 52–54). Three mutations that presumably alter Ca^{2+} binding at site 3 directly [p.D157G (55, 56) and p.D989G (57) at the EC1-2 and EC8-9 linker regions, respectively] or indirectly [p.G241D (52) at the EC2-3 linker region] are in the second group. Four more mutations [p.L408P (58), p.V507D (59), p.G1130R (60), p.S1267P (58)] are likely to disrupt proper folding, either because side chains involved in hydrogen bonding at β strands are mutated to proline residues, or because side chains pointing towards the hydrophobic core of an EC repeat are replaced by large hydrophilic residues. Intriguingly, our last group includes six mutations for which an evaluation of their structural impact is difficult. Four of them (p.G79R, p.R257H, p.P294L, and p.R941C) might not be causative of inherited deafness (60). The p.R1013H mutation, which has been shown to cause profound non-syndromic hearing impairment (61), is located near the PCDH15 EC9-10 kink, yet how it could perturb PCDH15 structure and dynamics is unclear. The last mutation, p.D414A (*SI Appendix*, Fig. S8*A*), has been suggested to be positively selected in East-Asian populations (62), but it has also been associated to inherited deafness (63). Prior structural analyses suggest that this polymorphism, common in many South Asian exomes, is unlikely to cause a severe loss-of-function phenotype (4). Our *hs* PCDH15 EC3-5 ex12a+ structure provides a view of the p.D414 site in the context of the CD2-1 isoform that includes a segment encoded by exon 12a: p.V(414+1)PPSGVP(414+7). In this structure, the side-chain of p.D414 is pushed closer to the monomer and to p.K410 when compared to the *hs* PCDH15 EC3-5 structure without exon 12a (PDB: 5T4M) (4). It is possible that a p.D414:p.K410 salt bridge rigidifies the EC3-4 linker region, or changes its affinity for Ca^{2+} in the context of the ex12a+ isoform only, but how losing the p.D414 side chain could cause an evolutionary advantage or a loss-of-function phenotype remains unclear.

NOTE 4: DISCUSSION

Two recent studies (43, 47) have provided important insights into PCDH15's structure using alternate and complementary approaches to those used here. Medium resolution (~11 Å) cryo-EM images of PCDH15 EC8-MAD12 and its transmembrane domain in complex with TMHS (47) eloquently revealed a highly dynamic EC8-10 ectodomain with either one or both monomers displaying kinked EC9-10 conformations that are consistent with our EC9-MAD12 structure and simulations. In the images reported by Ge *et al.* (47), ~20% of the recorded

conformations showed a bent conformation at this linker, while the refined straight model came from ~14% of conformations, thus suggesting that bending-unbending transitions may play a role in tip-link mechanics. However, it was unclear whether kinks and spontaneous bending-unbending dynamics were compatible with the complete dimeric ectodomain, as repeats EC1-7 were missing. Elegant structural models from negative staining EM images of longer PCDH15 ectodomain fragments (EC1-EC11 and EC1-MAD12) revealed flexural flexibility (43) and were nicely consistent with parallel dimerization at both the EC2-3 contacts (confirmed by a high resolution structure of PCDH15 EC1-3) (43) and the EC11-MAD12 segments. However, reconstructions and averages may have neglected significant bending and flexibility observed in raw images [Figure S8 in (43)], and resolution of the envelope (~20 Å) was not high enough to visualize details of PCDH15. Our structures, models, and simulations, obtained independently from the two studies mentioned above, not only fill in the missing pieces by providing a high-resolution and detailed view of the entire dimeric PCDH15 ectodomain, but also test its elasticity and dynamics *in silico*. Altogether, these data strongly support a model in which PCDH15 has two points of *cis* dimerization (EC2-3 and EC11-MAD12) and flexible linker regions at EC3-4, EC5-6, and EC9-10 that, along with unrolling of MAD12, may contribute to the overall elasticity of PCDH15.

A pair of exquisite single-molecule force spectroscopy experiments have also started to elucidate the elastic response of the PCDH15 monomer (51, 64). In the first set of experiments using an optical trap, the monomeric PCDH15 EC1-EC11 p.V250D protein fragment stretched in the presence of different Ca^{2+} concentrations (3 mM, 20 μM, and 1 mM EDTA) behaved as a soft entropic spring, with an effective spring constant that varied from < 0.5 mN/m to ~6 mN/m before rupture (extensibility between 100 nm and 150 nm). Three types of unfolding events (among many) were robustly identified, with extensions of ~4 nm (A_U), ~15 nm (B_U), and ~35 nm (C_U). The last type of unfolding event is consistent with rupture of an entire EC repeat and was more frequently observed in the absence of Ca^{2+}. In a second set of stretching experiments at various Ca^{2+} concentrations (1 mM, 300 μM, 30 μM, and 1 mM EGTA) using an atomic force microscope, selected monomers of the PCDH15 EC1-EC11 WT ectodomain were shown to be mechanically resilient with a well defined saw-tooth pattern even at 30 μM Ca^{2+}. Unfolding events with protein extensions of ~34 nm were accompanied by Ca^{2+}-dependent intermediates of shorter extensions of ~3.4 nm ("calcium rivets"). The overall mechanical response of PCDH15 was found to be less well defined and with force peaks of lower magnitude in the absence of Ca^{2+}. Comparison of these experimental results with predictions from our simulations is difficult, as in both studies the experiments did not include CDH23 bound to PCDH15 nor its MAD12 and were performed at slow stretching speeds equivalent to 1 Hz (51) mimicking low sound pressure levels (64). However, our predictions of reduced unfolding force peaks from low-Ca^{2+} simulations of various cadherins (3, 30, 65, 66), including PCDH15 as presented here, are consistent with a reduction in the magnitude of force peaks and an absence of well defined unfolding patterns as observed in *in vitro* experiments carried out without Ca^{2+} (51, 64). The events associated with shorter extensions (~3.4 nm and ~4 nm) observed in both sets of experiments are consistent with double force peaks monitored in simulations of CDH23 EC1-2 and PCDH15 EC3-5 for intermediates with broken linkers (4, 30). In addition, the predicted effective spring constants for the PCDH15 EC9-10 fragment at 0.02 nm/ns, k_1 ~8.4 mN/m (~5 nm extensibility) (6), and for the heterodimeric PCDH15 EC1-MAD12 + CDH23 EC1-2 complex at 0.1 nm/ns, k_1 ~3 mN/m (~10 nm extensibility), are within the range of those measured experimentally (51), although extensibilities differ. Our simulations suggest that this soft elasticity stems from unbending of kinked linker regions (EC9-10) and elongation of flexible linkers (EC3-4 and EC5-6) in the presence of saturating Ca^{2+} concentrations, rather than from each EC repeat behaving as an individual part of a freely jointed chain (51). Importantly, the elastic response of the monomeric PCDH15 ectodomain will be influenced by unrolling and unfolding of MAD12 (5), not present in both sets of force spectroscopy experiments (51, 64). Since PCDH15 most likely functions as a *cis* dimer in the tip link (53), the elastic response of the entire dimeric PCDH15 ectodomain, including the mechanically weak MAD12, needs to be taken into account.

Our simulations of the *hs* and *mm* $(PCDH15\ EC1\text{-}MAD12)_2$ + $(CDH23\ EC1\text{-}2/3)_2$ tetrameric complexes predict a stiffer elastic response (k_1 ~24 mN/m at 0.02 nm/ns and saturating Ca^{2+} concentrations) than that monitored for the monomer, with limited extensibility (~5 nm). Yet this estimate for the spring constant represents an upper bound (see Fig. 6*C* inset), given the fast stretching speeds used in simulations and the possibility that further equilibration of our models results in additional bending of EC9-10 and the other flexible linker regions of PCDH15 (EC3-4 and EC5-6). A completely relaxed state with bent linkers will be softer than a pre-stretched initial conformation. Thus, our data suggests that the degree of bending of various linker regions in the initial state of the dimeric PCDH15 molecules, controlled in part by the Ca^{2+} concentration around it, will determine whether it behaves as a soft or stiff spring. Our data also suggests that dimerization of PCDH15 as well as binding to CDH23 will have a significant impact on the conformational space available to the PCDH15 monomers and their response to force upon tetramer formation (Fig. 7*B*).

Whether tip links made of PCDH15 and CDH23 act as soft gating springs or stiff cables conveying tension *in vivo* has been an open question for decades (67, 68). SMD simulations of *mm* CDH23 EC1-2 saturated with Ca^{2+} ions bound at its four sites (three at the EC1-2 linker and one at the EC1 tip) revealed a stiff fragment and large unfolding force peaks that were Ca^{2+}-dependent. In absence of structural information from any other tip-link fragment at the time, the tip link was suggested to be stiff under the assumption that all other EC repeats would behave similarly (30). Yet further structural and computational work revealed flexible (4) and elastic elements (6) within PCDH15, and some atypical linkers in CDH23 (26). These data suggested that a kinked PCDH15 EC9-10 could provide Ca^{2+}-independent elasticity and at the same time withstand the tip-link resting tension (69), thus supporting a model in which the lower end of the tip link formed by PCDH15 could be soft, while the upper part of the tip link formed by CDH23 could be stiff (6). Our data partially supports this model: The structure of *mm* PCDH15 EC9-MAD12 reveals that the EC9-10 kink is still present in the context of a longer protein fragment and there are additional points of Ca^{2+}-independent elasticity in PCDH15 (particularly stemming from EC3-4 and EC5-6) that, all together, render the monomeric PCDH15 EC1-MAD12 soft (k_1 ~3 mN/m at 0.1 nm/ns, ~10 nm extensibility). However, while PCDH15 EC9-10 is still kinked in the context of the PCDH15 *cis* dimer, our heterotetrameric models of the PCDH15 EC1-MAD12 dimer are significantly stiffer than the heterodimeric models of PCDH15 EC1-MAD12 (k_1 ~24 mN/m at 0.02 nm/ns, ~5 nm extensibility). Unrolling and unfolding of MAD12 along with the Ca^{2+}-dependent response of various linker regions add another layer of complexity to the elastic response of PCDH15. Unfolding of MADs in PCDH15 and CDH23 could add significant extensibility to the tip link (up to ~30 nm per MAD) (5), thus providing an explanation to experiments in which extreme stimuli, likely inducing tip link extensions of ~100 nm, do not compromise the integrity of the mechanotransduction apparatus (70–72). In addition, the elastic response of PCDH15 (including MAD12) might be modified by interactions with TMHS (47) and other components of the transduction apparatus that may in turn help prevent unrolling and unfolding, or that might provide additional elasticity and extensibility as predicted for ankyrin repeats connected to the transduction channel complex formed by TMC and CIB proteins (65, 73–76). Additional simulations in which the center of mass of MAD12s were stretched, rather than their C-terminal Cα atoms, resulted in MAD12 unrolling without unfolding, followed by CDH23 unbinding (Movies 12 and 13). In this scenario, other components of the transduction apparatus would hold MAD12 through contacts with non C-terminal atoms thereby preventing its unfolding. However, it is unclear how such interactions would occur *in vivo*. Furthermore, at very low Ca^{2+} concentrations, PCDH15 might behave as a set of independent, freely jointed repeats (51, 66), with resting tension keeping these chains pre-stretched. Thus, depending on binding partners and the conditions in which PCDH15 is found and stretched, it might behave as a soft or stiff element with variable extensibility depending on unfolding behavior (Fig. 7*B*; *SI Appendix*, Fig. S16).

Biophysical experiments with bullfrog saccular hair cells stimulated *ex vivo* with a flexible fiber first identified the gating spring, which was estimated to have a stiffness of k ~0.5 mN/m in either 1 mM or 4 mM Ca^{2+} saline (67). Similar experiments using an optical trap estimated the gating spring stiffness to be k ~0.5 mN/m (4 mM Ca^{2+} saline) (77), and a recent study using calibrated fluid-jet stimulation determined a gradient of gating spring stiffness along the mammalian cochlea ranging from ~0.5 mN/m to ~1.7 mN/m in inner hair cells and from ~1.3 mN/m to 3.7 mN/m in outer hair cells (stiffness measurements done with 1.5 mM Ca^{2+} saline). Interestingly, the resting tension per tip link was also found to vary along the cochlea, from ~5.9 pN to ~16 pN for inner hair cells, and from ~4.7 pN to ~34 pN for outer hair cells. Maximal tip-link resting tension was estimated to be ~50 pN. In all cases, the gating-spring stiffness and resting tension per tip link were indirectly estimated; we lack direct information on what forces each tip link is experiencing and we do not know whether resting tension is applied as a constant or fluctuating force, and whether force stimuli from sound is faithfully mimicked by constant loading-rate stretching of tip-link molecules.

Laser velocimetry experiments from chinchilla cochlear hair cells *in vivo* indicate that the basilar membrane can move as fast as 0.01 m/s for loud sound (> 80 dB SPL) (78). Volumetric optical coherence tomography vibrometry data from mouse (79) is consistent with the chinchilla measurements and indicate that peak stereocilia displacements in cochlear hair cells range between ~10 nm to ~150 nm in response to sounds that go from 10 dB SPL (~6 kHz) to 80 dB SPL (~10 kHz) *in vivo*. These data are in agreement with *in situ* estimates of mouse and guinea pig stereocilia displacements (80, 81), and suggest that stereocilia can move as fast as 0.0015 m/s in normal hearing, and perhaps even faster for very loud sounds. Thus, stretching speeds used in our simulations (down to 0.02 nm/ns) are about one order of magnitude faster than those experienced by tip links *in vivo*, yet there is abundant theoretical, computational, and experimental work that can be used to interpret results at these high force loading rates (82–85). As stretching speed and loading rates increase, unbinding and unfolding forces are naturally larger, a phenomenon that is well documented in experiments (84) and simulations (83) and that is well understood theoretically (82, 85). While we cannot rule out that the sequence and type of events (unfolding *vs*. unbinding) observed at fast stretching speeds in simulations will be different at slower stretching speeds, our simulations were carried out at stretching speeds that are slower than

those that may favor unfolding of terminal ends (86) and provide specific predictions that can be tested and challenged experimentally *in vitro*.

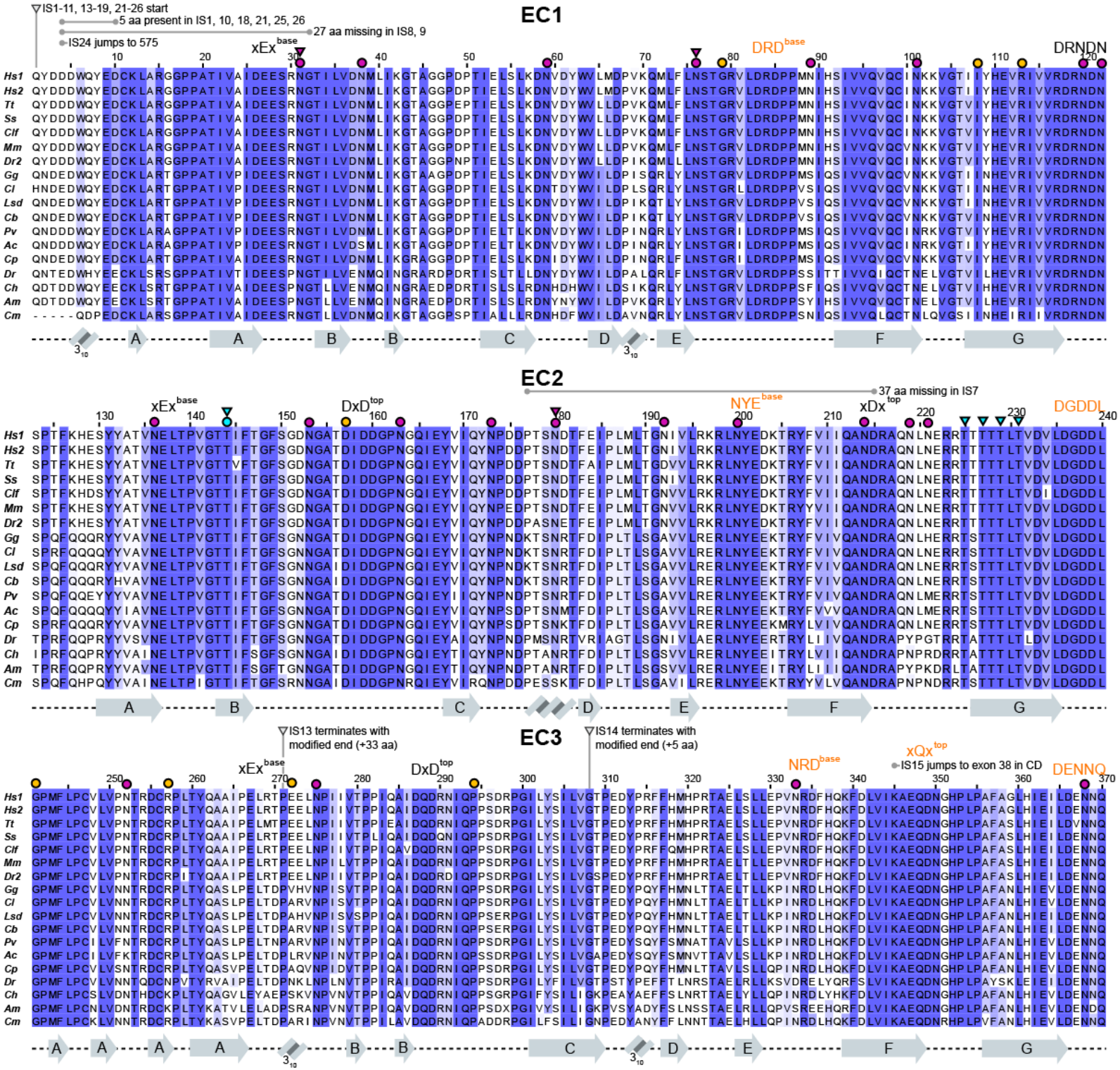
EC1
IS1-11, 13-19, 21-26 start
5 aa present in IS1, 10, 18, 21, 25, 26
27 aa missing in IS8, 9
IS24 jumps to 575
xEx base
DRD base
DRNDN
EC2
37 aa missing in IS7
xEx base
DxD top
NYE base
xDx top
DGDDL
EC3
IS13 terminates with modified end (+33 aa)
IS14 terminates with modified end (+5 aa)
xEx base
DxD top
NRD base
xQx top
IS15 jumps to exon 38 in CD
DENNQ
Hs1
Hs2
Tt
Ss
Clf
Mm
Dr2
Gg
Cl
Lsd
Cb
Pv
Ac
Cp
Dr
Ch
Am
Cm

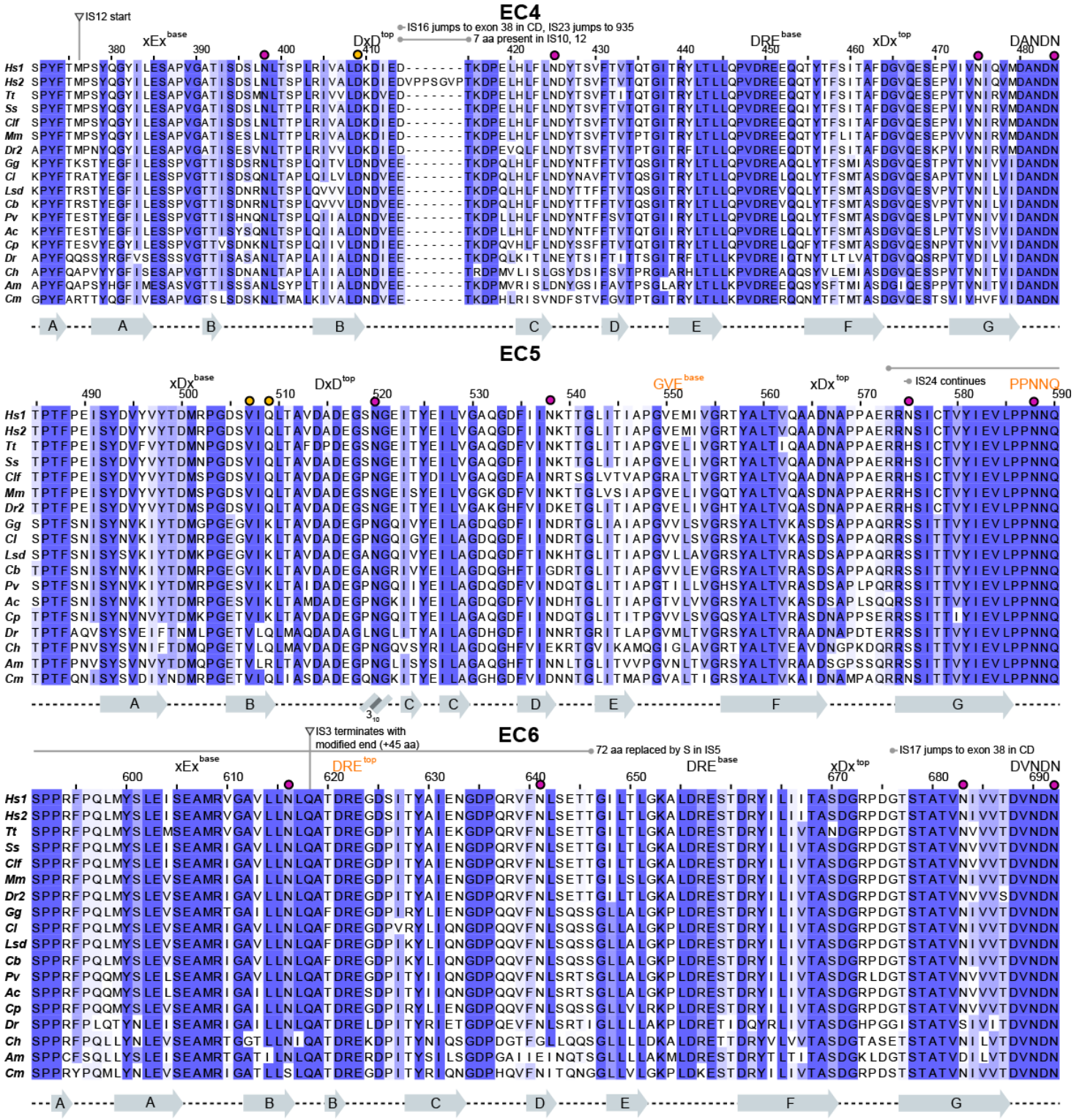
EC4
IS12 start
xEx base
DxD top
IS16 jumps to exon 38 in CD, IS23 jumps to 935
7 aa present in IS10, 12
DRE base
xDx top
DANDN
Hs1 SPYFTMPSYQGYILESAPVGATISDSLNLTSPLRIVALDKDIED-------TKDPELHLFLNDYTSVFTVTQTGITRYLTLLQPVDREEQQTYTFSITAFDGVQESEPVIVNIQVMDANDN
Hs2 SPYFTMPSYQGYILESAPVGATISDSLNLTSPLRIVALDKDIEDVPPSGVPTKDPELHLFLNDYTSVFTVTQTGITRYLTLLQPVDREEQQTYTFSITAFDGVQESEPVIVNIQVMDANDN
Tt SPYFTMPSYQGYILESAPVGATISDSMNLTSPLRIVVLDKDVED-------TKDPELHLFLNDYTSVFTITQTGITRYLTLLQPVDREEQQTYIFSITAFDGVQESEPVTVNIRVMDANDN
Ss SPYFTMPSYQGYILESAPVGATISDSLNLTTPLRIVALDKDIED-------TKDPELHLFLNDYTSVFTVTQTGITRYLTLLQPVDREEQQIYTFSITAFDGVQESEPVIVNIRVMDANDN
Clf SPYFTMPSYQGYILESAPVGATISDSLNLTTPLRIVALDKDIED-------TKDPELHLFLNDYTSVFTVTQTGITRYLTLLQPVDREEQQTYTFSITAFDGVQESEPVIVNIRVMDANDN
Mm SPYFTMPSYQGYILESAPVGATISESLNLTTPLRIVALDKDIED-------TKDPELHLFLNDYTSVFTVTPTGITRYLTLLQPVDREEQQTYTFLITAFDGVQESEPVVVNIRVMDANDN
Dr2 APYFTMPNYQGYILESAPVGATISESVNLTTPLRIVVLDKDIED-------TKDPEVQLFLNDYTSVFTVTPTGITRFLTLLQPVDREEQDTYIFSITAFDGVQESKPVIVNIRVMDANDN
Gg KPYFTKSTYEGFILESSPVGTTISDSRNLTSPLQITVLDNDVEE-------TKDPQLHLFLNDYNTFFTVTQSGITRYLTLLQPVDREAQQLYTFSMIASDGVQESTPVTVNIVVIDANDN
Cl KPYFTRATYEGFILESSPVGTTISDSQNLTAPLQILVLDNDVEE-------TKDPQLHLFLNDYNAVFTVTQSGITRYLTLLQPVDRELQQLYTFSMTASDGVQESAPVTVNILVIDANDN
Lsd KPYFTRSTYEGFILESSPVGTTISDNRNLTSPLQVVVLDNDVEE-------TKDPQLHLFLNDYTTFFTVTQSGITRYLTLLQPVDREVQQLYTFSMTASDGVQESVPVTVNILVIDANDN
Cb KPYFTRSTYEGFILESSPVGTTISDNRNLTSPLQVVVLDNDVEE-------TKDPQLHLFLNDYTTFFTVTQSGITRYLTLLQPVDREVQQLYTFSMTASDGVQESVPVTVNILVIDANDN
Pv KPYFTESTYEGFILESSPVGTTISHNQNLTSPLQIIALDNDVEE-------TKDPLLHLFLNDYNTFFSVTQTGIIRYLTLLQPVDRELQQLYTFSMTASDGVQESLPVTVNIVVIDANDN
Ac KPYFTESTYEGFILESSPVGTTISYSQNLTSPLQIIALDNDVEE-------TKDPLLHLFLNDYNTFFTVTQTGIIRYLTLLQPVDRELQQLYTFSMTASDGVQESLPVTVSIVVIDANDN
Cp KPYFTESVYEGYILESSPVGTTVSDNKNLTSPLQIIVLDNDIEE-------TKDPQVHLFLNDYSSFFTVTQTGITRYLTLLQPVDRELQQFYTFSMTASDGVQESNPVTVNIVVIDANDN
Dr APYFQQSSYRGFVSESSSVGTTISASANLTAPLAIIALDNDIEE-------TKDPQLKITLNEYTSIFTITTSGITRFLTLLKPVDREIQTNYTLTLVATDGVQQSRPVTVDILVIDANDN
Ch APYFQAPVYYGFISESAPVGTTISDNANLTAPLAIIALDNDIEE-------TRDPMVLISLGSYDSIFSVTPRGIARHLTLLKPVDREAQQSYVLEMIASDGVQESSPVTVNITVIDANDN
Am APYFQAPSYHGFIMESASVGTTISSSANLSYPLTIIALDNDVEE-------TKDPMVRISLDNYGSIFAVTPSGLARYLTLLKPVDREQQSYSFTMIASDGIQESPPVTVNITVIDANDN
Cm GPYFARTTYQGFIVESAPVGTSLSDSKNLTMALKIVALDNDVEE-------TKDPHLRISVNDFSTVFGVTPTGITRYLTLLKPVDREQQNYTFTMTASDGVQESTSVIVHVFVIDANDN
A A B B C D E F G
EC5
xDx base
DxD top
GVE base
xDx top
IS24 continues
PPNNQ
Hs1 TPTFPEISYDVYVYTDMRPGDSVIQLTAVDADEGSNGEITYEILVGAQGDFIINKTTGLITIAPGVEMIVGRTYALTVQAADNAPPAERRNSICTVYIEVLPPNNQ
Hs2 TPTFPEISYDVYVYTDMRPGDSVIQLTAVDADEGSNGEITYEILVGAQGDFIINKTTGLITIAPGVEMIVGRTYALTVQAADNAPPAERRNSICTVYIEVLPPNNQ
Tt TPTFPEISYDVFVYTDMNPGDSVIQLTAFDPDEGSNGEITYEILVGAQGDFVINKTTGLITIAPGVELIVGRTYALTIQAADNAPPAERRHSICTVYIEVLPPNNQ
Ss TPTFPEISYDVYVYTDMNPGDSVIQLTAVDADEGSNGEITYEILVGAQGDFIINKTTGLITIAPGVELIVGRTYALTVQAADNAPPAERRHSICTVYIEVLPPNNQ
Clf TPTFPEISYDVYVYTDMSPGDSVIQLTAVDADEGPNGEITYDILVGAQGDFAINRTSGLVTVAPGRALTVGRTYALTVQAADNAPPAERRHSICTVYIEVLPPNNQ
Mm TPTFPEISYDVYVYTDMSPGDSVIQLTAVDADEGSNGEISYEILVGGKGDFVINKTTGLVSIAPGVELIVGQTYALTVQASDNAPPAERRHSICTVYIEVLPPNNQ
Dr2 TPTFPEISYDVYVYTDMSPGDSVIQLTAVDADEGSNGEITYEILVGAKGHFVIDKETGLITIAPGVELIVGHTYALTVQASDNAPPAERRHSICTVYIEVLPPNNQ
Gg SPTFSNISYNVKIYTDMGPGEGVIKLTAVDADEGPNGQIVYEILAGDQGDFIINDRTGLIAIAPGVVLSVGRSYALTVKASDSAPPAQRRSSITTVYIEVLPPNNQ
Cl SPTFSNISYNVKIYTDMRPGEGVIKLTAVDADEGPNGQIGYEILAGDQGDFIINDRTGLITIAPGVVLSVGRSYALTVKASDSAPPAQRRSSITTVYIEVLPPNNQ
Lsd SPTFSNISYSVKIYTDMKPGEGVIKLTAVDADEGANGQIVYEILAGDQGDFTINKHTGLITIAPGVLLAVGRSYALTVRASDSAPPAQRRSSITTVYIEVLPPNNQ
Cb TPTFSNISYNVKIYTDMRPGEGVIKLTAVDADEGANGRIVYEILAGDQGHFTIGDRTGLITIAPGVVLEVGRSYALTVRASDSAPPAQRRSSITTVYIEVLPPNNQ
Pv SPTFSNISYNVKIYTDMRPGESVIKLTAIDADEGPNGQIIYEILAGDQGDFVINDQTGLITIAPGTILLVGHSYALTVRASDSAPLPQRRSSITTVYIEVLPPNNQ
Ac SPTFSNISYNVKIYTDMRPGESVIKLTAMDADEGPNGKIIYEILAGDQGDFVINDHTGLITIAPGTVLVVGRSYALTVKASDSAPLSQQRSSITTVYIEVLPPNNQ
Cp TPTFSNISYNVNVYTDMKPGETVIKLTAVDADEGPNGQITYEILAGAQGDFIINDQTGLITITPGVVLSVGQSYALTVRASDNAPPSERRSSITTIYIEVLPPNNQ
Dr TPTFAQVSYSVEIFTNMLPGETVLQLMAQDADAGLNGLITYAILAGDHGDFIINNRTGRITLAPGVMLTVGRSYALTVRAADNAPDTERRSSITTVYIEVLPPNNQ
Ch TPTFPNVSYSVNIFTDMQPGETVLQLMAVDADEGPNGQVSYRILAGDQGHFVIEKRTGVIKAMQGIGLAVGRTYALTVEAVDNGPKDQRRSSITTVYIEVLPPNNQ
Am TPTFPNVSYSVNVYTDMQPGETVLRLTAVDADEGPNGLISYSILAGAQGHFTINNLTGLITVVPGVNLTVGRSYALTVRAADSGPSSQRRSSITTVYIEVLPPNNQ
Cm TPTFQNISYSVDIYNDMRPGETVIQLIASDADEGQNGKITYEILAGGHGDFVIDNNTGLITMAPGVALTIGRSYALTVKAIDNAMPAQRRNSITTVYIEVLPPNNQ
A A B 3₁₀ C C D E F G
EC6
IS3 terminates with modified end (+45 aa)
72 aa replaced by S in IS5
IS17 jumps to exon 38 in CD
xEx base
DRE top
DRE base
xDx top
DVNDN
Hs1 SPPRFPQLMYSLEISEAMRVGAVLLNLQATDREGDSITYAIENGDPQRVFNLSETTGILTLGKALDRESTDRYILIITASDGRPDGTSTATVNIVVTDVNDN
Hs2 SPPRFPQLMYSLEISEAMRVGAVLLNLQATDREGDSITYAIENGDPQRVFNLSETTGILTLGKALDRESTDRYILIITASDGRPDGTSTATVNIVVTDVNDN
Tt SPPRFPQLMYSLEMSEAMRVGAVLLNLQATDREGDPITYAIEKGDPQRVFNLSETTGILTLGKALDRESTDRYILIVTANDGRPDGTSTATVNVVVTDVNDN
Ss SPPRFPQLMYSLEISEAMRIGAVLLNLQATDREGDPITYAIENGDPQRVFNLSETTGILTLGKALDRESTDRYILIVTASDGRPDGTSTATVNVVVTDVNDN
Clf SPPRFPQLMYSLEISEAMRIGAVLLNLQATDREGDPITYAIENGDPQRVFNLSETTGILTLGKALDRESTDRYILIVTASDGRPDGTSTATVNVVVTDVNDN
Mm SPPRFPQLMYSLEVSEAMRIGAILLNLQATDREGDPITYAIENGDPQRVFNLSETTGILSLGKALDRESTDRYILIVTASDGRPDGTSTATVNIVVTDVNDN
Dr2 SPPRFPQLMYSLEVSEAMRIGAVLLNLQATDREGDPITYAIENGDPQRVFNLSETTGILTLGKALDRESTDRYILIVTASDGRPDGTSTATVNVVVSDVNDN
Gg SPPRFPQLMYSLEVSEAMRTGAILLNLQAFDREGDPIRYLIENGDPQQVFNLSQSSGLLALGKPLDRESTDRYILIVTASDGRPDGTSTATVNIVVTDVNDN
Cl SPPRFPQLMYSLEVSEAMRIGAVLLNLQAFDREGDPVRYLIQNGDPQQVFNLSQSSGLLALGKPLDRESTDRYILIVTASDGRPDGTSTATVNIVVTDVNDN
Lsd SPPRFPQLMYSLEVSEAMRIGAVLLNLQAFDREGDPIKYLIQNGDPQQVFNLSQSSGLLALGKPLDRESTDRYILIVTASDGRPDGTSTATVNIVVTDVNDN
Cb SPPRFPQLMYSLEVSEAMRIGAVLLNLQAFDREGDPIKYLIQNGDPQQVFNLSQSSGLLALGKPLDRESTDRYILIVTASDGRPDGTSTATVNIVVTDVNDN
Pv SPPRFPQQMYSLELSEAMRIGAVLLNLQATDREGDPITYIIQNGDPQQVFNLSRTSGLLALGKPLDRESTDRYILIVTASDGRPDGTSTATVNVVVTDVNDN
Ac SPPRFPQQMYSLELSEAMRIGAILLNLQATDRESDPITYIIQNGDPQQVFNLSRTSGLLALGKPLDRESTDRYILIVTASDGRPDGTSTATVNVVVTDVNDN
Cp SPPRFPQQMYSLEVSEAMRIGAILLNLQATDREGDPIRYLIENGDPQQVFNLSQSSGLLVLRKPLDRESTDRYILIVTASDGRPDGTSTATVNVVVTDVNDN
Dr SPPRFPLQTYNLEISEAMRIGAILLNLQATDRELDPITYRIETGDPQEVFNLSRTIGLLLLAKPLDRETTIDQYRLIVTASDGHPGGISTATVSIVITDVNDN
Ch SPPRFPQLLYNLEVSEAMRTGGTLLNIQATDREKDPITYNIQSGDPDGTFGLLQQSGLLLLDKALDRETTDRYVLVVTASDGTASETSTATVNILVTDVNDN
Am SPPCFSQLLYSLEISEAMRTGATILNLQATDRERDPITYSILSGDPGAIIEINQTSGLLLLAKMLDRESTDRYTLTITASDGKLDGTSTATVDILVTDVNDN
Cm SPPRYPQMLYNLEVSEAMRIGATLLSLQATDREGDPITYRIQNGDPHQVFNITQNGGLLVLGKPLDKESTDRYILIVTASDGRPDSTSTATVNIVVTDVNDN

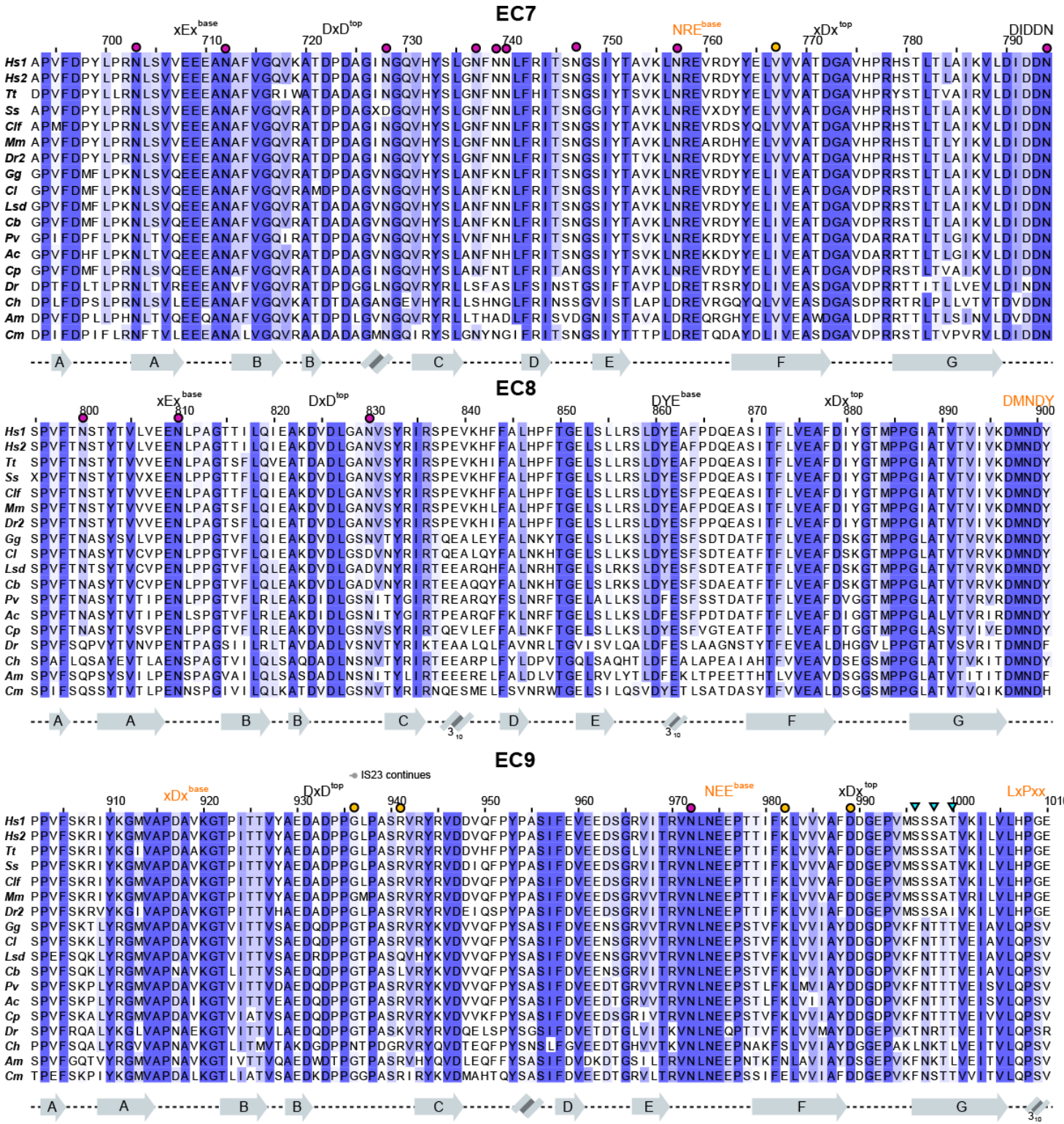
EC7
xEx base
DxD top
NRE base
xDx top
DIDDN
700 710 720 730 740 750 760 770 780 790
Hs1 APVFDPYLPRNLSVVEEEANAFVGQVKATDPDAGINGQVHYSLGNFNNLFRITSNGSIYTAVKLNREVRDYYELVVVATDGAVHPRHSTLTLAIKVLDIDDN
Hs2 APVFDPYLPRNLSVVEEEANAFVGQVKATDPDAGINGQVHYSLGNFNNLFRITSNGSIYTAVKLNREVRDYYELVVVATDGAVHPRHSTLTLAIKVLDIDDN
Tt DPVFDPYLLRNLSVVEEEANAFVGRIWATDADAGINGQVHYSLGNFNNLFHITSNGSIYTSVKLNREVRDYYELVVVATDGAVHPRYSTLTVAIRVLDIDDN
Ss APVFDPYLPRNLSVVEEEANAFVGQVRATDPDAGXDGQVHYSLGNFNNLFRITSNGGIYTAVKLNREVXDYYELVVVATDGAVHPRHSTLTLAIKVLDIDDN
Clf APMFDPYLPRNLSVVEEEANAFVGQVRATDPDAGINGQVHYSLGNFNNLFRITSNGSIYTAVKLNREVRDSYQLVVVATDGAVHPRHSTLTLAIKVLDIDDN
Mm APVFDPYLPRNLSVVEEEANAFVGQVRATDPDAGINGQVHYSLGNFNNLFRITSNGSIYTAVKLNREARDHYELVVVATDGAVHPRHSTLTLYIKVLDIDDN
Dr2 APVFDPYLPRNLSVVEEEANAFVGQVRATDPDAGINGQVYYSLGNFNNLFRITSNGSIYTTVKLNREVRDYYELVVVATDGAVHPRHSTLTLAIKVLDIDDN
Gg GPVFDMFLPKNLSVQEEEANAFVGQVRATDPDAGVNGQVHYSLANFKNLFRITSNGSIYTAVKLNREVRDYYELIVEATDGAVDPRRSTLTLAIKVLDIDDN
Cl GPVFDMFLPKNLSVQEEEANAFVGQVRAMDPDAGVNGQVHYSLANFKNLFRITSNGSIYTAVKLNREVRDYYELIVEATDGAVDPRRSTLTLAIKVLDIDDN
Lsd GPVFDMFLPKNLSVQEEEANAFVGQVRATDADAGVNGQVHYSLANFNNLFRITSNGSIYTAVKLNREVRDYYELIVEATDGAVDPRRSTLTLAIKVLDIDDN
Cb GPVFDMFLPKNLSVQEEEANAFVGQVRATDADAGVNGQVHYSLANFKNLFRITSNGSIYTAVKLNREVRDYYELIVEATDGAVDPRRSTLTLAIKVLDIDDN
Pv GPIFDPFLPKNLTVQEEEANAFVGQIRATDPDAGVNGQVHYSLVNFNHLFRITSNGSIYTSVKLNREKRDYYELIVEATDGAVDARRATLTLGIKVLDIDDN
Ac GPVFDHFLPKNLTVQEEEANAFVGQVRATDPDAGVNGQVRYSLANFNHLFRITSNGSIYTSVKLNREKKDYYELIVEATDGAVDARRTTLTLGIKVLDIDDN
Cp GPVFDMFLPRNLSVQEEEANAFVGQVRATDADAGINGQVHYSLANFNTLFRITANGSIYTAVKLNREVRDYYELIVEATDGAVDPRRSTLTVAIKVLDIDDN
Dr DPTFDLTLPRNLTVREEEANVFVGQVRATDPDGGLNGQVRYRLLSFASLFSINSTGSIFTAVPLDRETRSRYDLIVEASDGAVDPRRTTITLLVEVLDINDN
Ch DPLFDPSLPRNLSVLEEEANAFVGQVKATDTDAGANGEVHYRLLSHNGLFRINSSGVISTLAPLDREVRGQYQLVVEASDGASDPRRTRLPLLVTVTDVDDN
Am DPVFDPLLPHNLTVQEEQANAFVGQVKATDPDLGVNGQVRYRLLTHADLFRISVDGNISTAVALDREQRGHYELVVEAWDGALDPRRTTLTLSINVLDVDDN
Cm DPIFDPIFLRNFTVLEEEANALVGQVRAADADAGMNGQIRYSLGNYNGIFRITSNGSIYTTTPLDRETQDAYDLIVEASDGAVDPRRSTLTVPVRVLDIDDN
A A B B C D E F G
EC8
xEx base
DxD top
DYE base
xDx top
DMNDY
800 810 820 830 840 850 860 870 880 890 900
Hs1 SPVFTNSTYTVLVEENLPAGTTILQIEAKDVDLGANVSYRIRSPEVKHFFALHPFTGELSLLRSLDYEAFPDQEASITFLVEAFDIYGTMPPGIATVTVIVKDMNDY
Hs2 SPVFTNSTYTVLVEENLPAGTTILQIEAKDVDLGANVSYRIRSPEVKHFFALHPFTGELSLLRSLDYEAFPDQEASITFLVEAFDIYGTMPPGIATVTVIVKDMNDY
Tt SPVFTNSTYTVVVEENLPAGTSFLQVEATDADLGANVSYRIRSPEVKHIFALHPFTGELSLLRSLDYEAFPDQEASITFLVEAFDIYGTMPPGIATVTVIVKDMNDY
Ss XPVFTNSTYTVVXEENLPPGTTFLQIEAKDVDLGANVSYRIRSPEVKHFFALHPFTGELSLLRSLDYESFPDQEASITFLVEAFDIYGTMPPGIATVTVIVKDMNDY
Clf SPVFTNSTYTVVVEENLPAGTTFLQIEAKDVDLGANVSYRIRSPEVKHFFALHPFTGELSLLRSLDYESFPEQEASITFLVEAFDIYGTMPPGIATVTVIVKDMNDY
Mm SPVFTNSTYTVVVEENLPAGTSFLQIEAKDVDLGANVSYRIRSPEVKHLFALHPFTGELSLLRSLDYEAFPDQEASITFLVEAFDIYGTMPPGIATVTVIVKDMNDY
Dr2 SPVFTNSTYTVVVEENLPAGTSFLQIEATDVDLGANVSYRIRSPEVKHIFALHPFTGELSLLRSLDYESFPPQEASITFLVEAFDIYGTMPPGIATVTVIVKDMNDY
Gg SPVFTNASYSVLVPENLPPGTVFLQIEAKDVDLGSNVTYRIRTQEALEYFALNKYTGELSLLKSLDYESFSDTDATFTFLVEAFDSKGTMPPGLATVTVRVKDMNDY
Cl SPVFTNASYTVCVPENLPPGTVFLQIEAKDVDLGSDVNYRIRTQEALQYFALNKHTGELSLLKSLDYESFSDTEATFTFLVEAFDSKGTMPPGLATVTVRVKDMNDY
Lsd SPVFTNTSYTVCVPENLPPGTVFLQLEAKDVDLGADVNYRIRTEEARQHFALNRHTGELSLRKSLDYESFSDTEATFTFLVEAFDSKGTMPPGLATVTVRVKDMNDY
Cb SPVFTNASYTVCVPENLPPGTVFLQLEAKDVDLGADVNYRIRTEEAQQYFALNKHTGELSLRKSLDYESFSDAEATFTFLVEAFDSKGTMPPGLATVTVRVKDMNDY
Pv SPVFTNASYTVTIPENLPPGTVFLRLEAKDIDLGSNITYGIRTREARQYFSLNRFTGELSLLKSLDFESFSSTDATFTFLVEAFDVGGTMPPGLATVTVRVRDMNDY
Ac SPVFTNASYTVTIPENLSPGTVFLRLEAKDIDLGSNITYGIRTPEARQFFKLNRFTGELSLLKSLDFESFPDTDATFTFLVEAFDIGGTMPPGLALVTVRIRDMNDY
Cp SPVFTNASYTVSVPENLPPGTVFLRLEAKDVDLGSNVSYRIRTQEVLEFFALNKFTGELSLLKSLDYESFVGTEATFTFLVEAFDTGGTMPPGLASVTVIVEDMNDY
Dr SPVFSQPVYTVNVPENTPAGSIILRLTAVDADLVSNVTYRIKTEAALQLFAVNRLTGVISVLQALDFESLAAGNSTYTFEVEALDHGGVLPPGTATVSVRITDMNDF
Ch SPAFLQSAYEVTLAENSPAGTVILQLSAQDADLNSNVTYRIRTEEARPLFYLDPVTGQLSAQHTLDFEALAPEAIAHTFVVEAVDSEGSMPPGLATVTVKITDMNDY
Am SPVFSQPSYSVILPENSPAGVAILQLSASDADLNSNITYLIRTEEERELFALDLVTGELRVLYTLDFEKLTPEETTHTLVVEAVDSGGSMPPGLATVTITITDMNDF
Cm SPIFSQSSYTVTLPENNSPGIVILQLKATDVDLGSNVTYRIRNQESMELFSVNRWTGELSILQSVDYETLSATDASYTFVVEALDSGGSMPPGLATVTVQIKDMNDH
A A B B C 3 10 D E 3 10 F G
EC9
IS23 continues
xDx base
DxD top
NEE base
xDx top
LxPxx
910 920 930 940 950 960 970 980 990 1000 1010
Hs1 PPVFSKRIYKGMVAPDAVKGTPITTVYAEDADPPGLPASRVRYRVDDVQFPYPASIFEVEEDSGRVITRVNLNEEPTTIFKLVVVAFDDGEPVMSSSATVKILVLHPGE
Hs2 PPVFSKRIYKGMVAPDAVKGTPITTVYAEDADPPGLPASRVRYRVDDVQFPYPASIFEVEEDSGRVITRVNLNEEPTTIFKLVVVAFDDGEPVMSSSATVKILVLHPGE
Tt PPVFSKRIYKGIVAPDAAKGTPITTVYAEDADPPGLPASRVRYRVDDVHFPYPASIFDVEEDSGLVITRVNLNEEPTTIFKLVVVAFDDGEPVMSSSATVKILVLHPGE
Ss PPVFSKRIYKGMVAPDAVKGTPITTVYAEDADPPGLPASRVRYRVDDIQFPYPASIFDVEEDSGRVITRVNLNEEPTTIFKLVVVAFDDGEPVMSSSATVKILVLHPGE
Clf PPVFSKRIYKGMVAPDAVKGTPITTVYAEDADPPGLPASRVRYRVDDVQFPYPASIFDVEEDSGRVITRVNLNEEPTTIFKLVVVAFDDGEPVMSSSATVKILVLHPGE
Mm PPVFSKRIYKGMVAPDAVKGTPITTVYAEDADPPGMPASRVRYRVDDVQFPYPASIFDVEEDSGRVVTRVNLNEEPTTIFKLVVVAFDDGEPVMSSSATVRILVLHPGE
Dr2 PPVFSKRVYKGIVAPDAVKGTPITTVHAEDADPPGLPASRVRYRVDEIQSPYPASIFDVEEDSGRVITRVNLNEEPTTIFKLVVIAFDDGEPVMSSSAIVKILVLHPGE
Gg SPVFSKTLYRGMVAPDAVKGTVITTVSAEDQDPPGTPASRVRYKVDVVQFPYSASIFDVEENSGRVVTRVNLNEEPSTVFKLVVIAYDDGDPVKFNTTTVEIAVLQPSV
Cl SPVFSKKLYRGMVAPDAVKGTVITTVSAEDQDPPGTPASRVRYKVDVVQFPYSASIFDVEENSGRVVTRVNLNEEPSTVFKLVVIAYDDGDPVKFNTTTVEIAVLQPSV
Lsd SPEFSQKLYRGMVAPDAVKGTVITTVSAEDRDPPGTPASQVHYKVDVVQFPYSASIFDVEENSGRVVTRVNLNEEPSTVFKLVVIAYDDGDPVKFNTTTVEIAVLQPSV
Cb SPVFSQKLYRGMVAPNAVKGTLITTVSAEDQDPPGTPASLVRYKVDVVQFPYSASIFDVEENSGRVITRVNLNEEPSTVFKLVVIAYDDGDPVKFNTTTVEIAVLQPSV
Pv SPVFSKPLYRGMVAPDAVKGTVITTVDAEDQDPPGTPASRVRYKVDVVQFPYSASIFDVEEDTGRVVTRVNLNEEPSTLFKLMVIAYDDGDPVKFNTTTVEISVLQPSV
Ac SPVFSKPLYRGMVAPDAIKGTVITTVEAEDQDPPGTPASRVRYKVDVVQFPYSASIFDVEEDTGRVVTRVNLNEEPSTLFKLVIIAYDDGDPVKFNTTTVEISVLQPSV
Cp SPVFSKALYRGMVAPDAVKGTVIATVSAEDQDPPGTPASRVRYKVDVVKFPYSASIFDVEEDSGRIVTRVNLNEEPSTVFKLVVIAYDDGDPVKFNTTTVEIVVLQPSV
Dr SPVFRQALYKGLVAPNAEKGTVITTVLAEDQDPPGTPASKVRYRVDQELSPYSGSLFDVETDTGLVITKVNLNEQPTTVFKLVVMAYDDGEPVKTNRTTVEITVLQPSR
Ch PPVFSQALYRGVVAPNAVKGTLITMVTAKDGDPPNTPDGRVRYQVDTEQFPYSNSLFGVEEDTGHVVTKVNLNEEPNAKFSLVVIAYDGGEPAKLNKTLVEITVLQPSV
Am SPVFGQTVYRGMVAPNAVKGTIVTTVQAEDWDTPGTPASRVHYQVDLEQFFYSASIFDVDKDTGSILTRVNLNEEPNTKFNLAVIAYDSGEPVKFNKTLVEITVLQPSV
Cm TPEFSKPIYKGMVAPDALKGTLIATVSAEDKDPPGGPASRIRYKVDMAHTQYSASIFDVEEDTGRVLTRVNLNEEPSSIFELVVIAFDDGEPVKFNSTTVVITVLQPSV
A A B B C D E F G 3 10

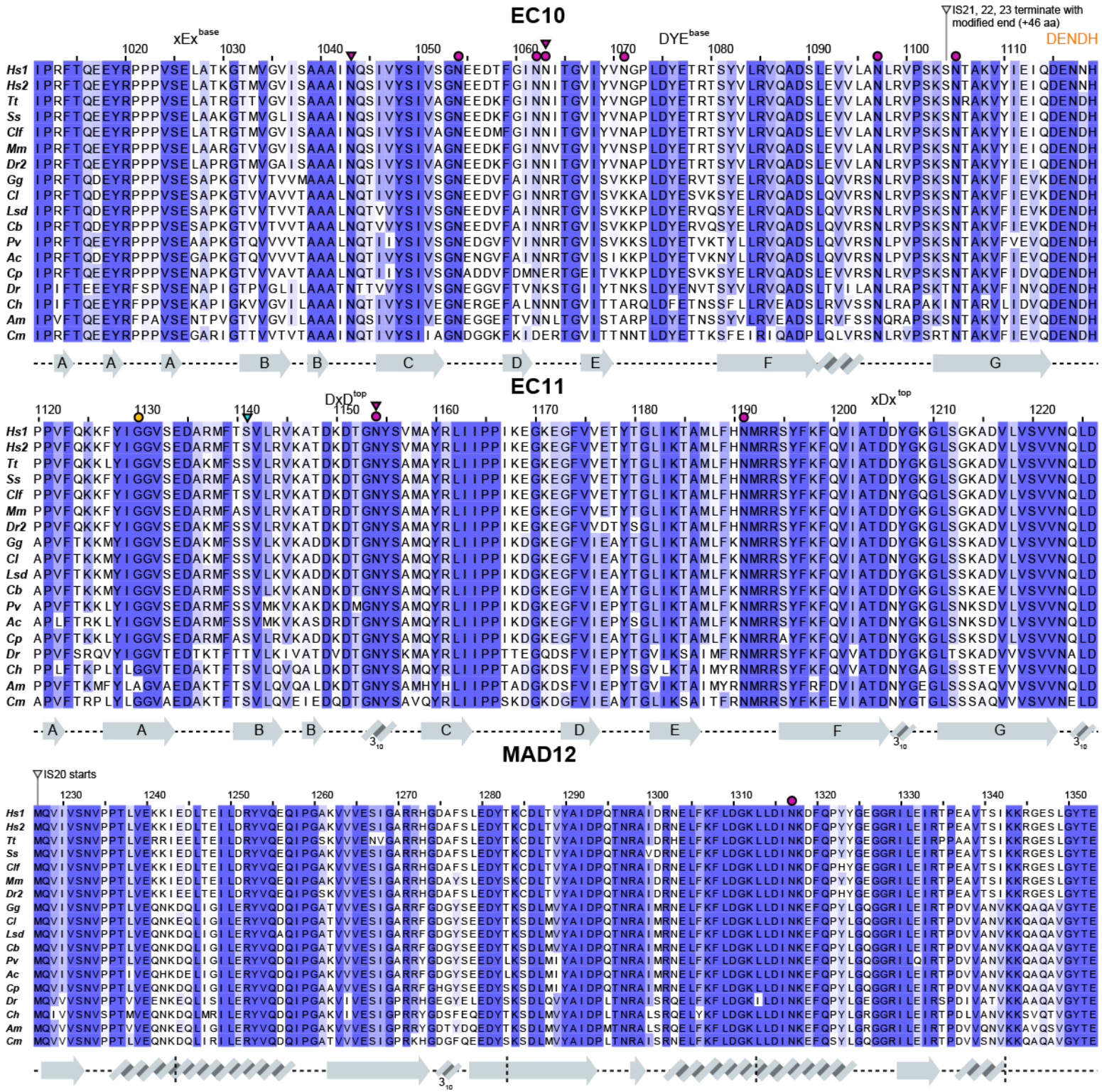
EC10
IS21, 22, 23 terminate with modified end (+46 aa)
DENDH
xEx base
DYE base
1020 1030 1040 1050 1060 1070 1080 1090 1100 1110
Hs1 IPRFTQEEYRPPPVSELATKGTMVGVISAAAINQSIVYSIVSGNEEDTFGINNITGVIYVNGPLDYETRTSYVLRVQADSLEVVLANLRVPSKSNTAKVYIEIQDENNH
Hs2 IPRFTQEEYRPPPVSELATKGTMVGVISAAAINQSIVYSIVSGNEEDTFGINNITGVIYVNGPLDYETRTSYVLRVQADSLEVVLANLRVPSKSNTAKVYIEIQDENNH
Tt IPRFTQEEYRPPPVSELATRGTTVGVISAAAINQSIVYSIVAGNEEDKFGINNITGVIYVNGPLDYETRTSYVLRVQADSLEVVLANLRVPSKSNRAKVYIEIQDENDH
Ss IPRFTQEEYRPPPVSELAAKGTMVGLISAAAINQSIVYSIVSGNEEDKFGINNITGVIYVNAPLDYETRTSYVLRVQADSLEVVLANLRVPSKSNTAKVYIEIQDENDH
Clf IPRFTQEEYRPPPVSELATRGTMVGVISAAAINQSIVYSIVAGNEEDMFGINNITGVIYVNAPLDYETRTSYVLRVQADSLEVVLANLRVPSKSNTAKVYIEIQDENDH
Mm IPRFTQEEYRPPPVSELAARGTVVGVISAAAINQSIVYSIVAGNEEDKFGINNVTGVIYVNSPLDYETRTSYVLRVQADSLEVVLANLRVPSKSNTAKVYIEIQDENDH
Dr2 IPRFTQEEYRPPPVSELAPRGTMVGAISAAAINQSIVYSIVAGNEEDKFGINNITGVIYVNAPLDYETRTSYVLRVQADSLEVVLANLRVPSKSNTAKVYIEIQDENDH
Gg IPRFTQDEYRPPPVSESAPKGTVVTVVMAAALNQTIVYSIVSGNEEDVFAINNRTGVISVKKPLDYERVTSYELRVQADSLQVVRSNLRVPSKSNTAKVFIEVKDENDH
Cl IPRFTQDEYRPPPVSESAPKGTVVAVVTAAALNQTIVYSIVSGNEEDVFGINNRTGVISVKKALDYESVKSYELRVQADSLQVVRSNLRVPSKSNTAKVFIEVKDENDH
Lsd IPRFTQDEYRPPPVSESAPKGTVVTVVTAAALNQTVVYSIVSGNEEDVFAINNRTGVISVKKPLDYERVQSYELRVQADSLQVVRSNLRVPSKSNTAKVFIEVKDENDH
Cb IPRFTQDEYRPPPVSESAPKGTVVTVVTAAALNQTVVYSIVSGNEEDVFAINNRTGVISVKKPLDYERVQSYELRVQADSLQVVRSNLRVPSKSNTAKVFIEVKDENDH
Pv IPRFTQEEYRPPPVSEAAPKGTQVVVVTAAALNQTIIYSIVSGNEDGVFVINNRTGVISVKKSLDYETVKTYLLRVQADSLQVVRSNLPVPSKSNTAKVFVEVQDENDH
Ac IPRFTQDEYRPPPVSEGAPKGTQVVVVTAAALNQTIVYSIVSGNENGVFAINNRTGVISIKKPLDYETVKNYLLRVQADSLQVVRSNLPVPSKSNTAKVFIEVQDENDH
Cp IPRFTQEEYRPPPVSENAPKGTVVVAVTAAALNQTIIYSIVSGNADDVFDMNERTGEITVKKPLDYESVKSYELRVQADSLEVVRSNLRVPSKSNTAKVFIDVQDENDH
Dr IPIFTEEEYRFSPVSENAPIGTPVGLILAAATNTTVVYSIVSGNEGGVFTVNKSTGIIYTNKSLDYENVTSYVLRVQADSLTVILANLRAPSKTNTAKVFINVQDENDH
Ch IPIFTQEEYRFPPVSEKAPIGKVVGVILAAAINQTIVYSIVEGNERGEFALNNNTGVITTARQLDFETNSSFLLRVEADSLRVVSSNLRAPAKINTARVLIDVQDENDH
Am IPVFTQEEYRFPAVSENTPVGTVVGVILAAAINQSIVYSIVEGNEGGEFTVNNLTGVISTARPLDYETNSSYVLRVFSSNQRAPSKSNTAKVYIEVQDENDH
Cm IPRFTQEEYRPPPVSEGARIGTTVVTVTAAAINQTIVYSIIAGNDGGKFKIDERTGVITTNNTLDYETTKSFEIRIQADPLQLVRSNLRVPSRTNTAKVFIEVQDENDH
A A A B B C D E F G
EC11
DxD top
xDx top
1120 1130 1140 1150 1160 1170 1180 1190 1200 1210 1220
Hs1 PPVFQKKFYIGGVSEDARMFTSVLRVKATDKDTGNYSVMAYRLIIPPIKEGKEGFVVETYTGLIKTAMLFHNMRRSYFKFQVIATDDYGKGLSGKADVLVSVVNQLD
Hs2 PPVFQKKFYIGGVSEDARMFTSVLRVKATDKDTGNYSVMAYRLIIPPIKEGKEGFVVETYTGLIKTAMLFHNMRRSYFKFQVIATDDYGKGLSGKADVLVSVVNQLD
Tt PPVFQKKLYIGGVSEDAKMFSSVLRVKATDKDTGNYSAMAYRLIIPPIKEGKEGFVVETYTGLIKTAMLFHNMRRSYFKFQVIATDDYGKGLSGKADVLVSVVNQLD
Ss PPVFQKKFYIGGVSEDARMFASVLRVKATDKDTGNYSAMAYRLIIPPIKEGKEGFVVETYTGLIKTAMLFHNMRRSYFKFQVIATDDYGKGLSGKADVLVSVVNQLD
Clf PPVFQKKFYIGGVSEDARMFTSVLRVKATDKDTGNYSAMAYRLIIPPIKEGKEGFVVETYTGLIKTAMLFHNMRRSYFKFQVIATDNYGQGLSGKADVLVSVVNQLD
Mm PPVFQKKFYIGGVSEDARMFASVLRVKATDRDTGNYSAMAYRLIIPPIKEGKEGFVVETYTGLIKTAMLFHNMRRSYFKFQVIATDDYGKGLSGKADVLVSVVNQLD
Dr2 PPVFQKKFYIGGVSEDAKMFSSVLRVKATDKDTGNYSAMAYRLIIPPIKEGKEGFVVDTYSGLIKTAMLFHNMRRSYFKFQVIATDDYGKGLSGKADVLVSVVNQLD
Gg APVFTKKMYIGGVSEDAKMFSSVLKVKADDKDTGNYSAMQYRLIIPPIKDGKEGFVIEAYTGLIKTAMLFKNMRRSYFKFQVIATDDYGKGLSSKADVLVSVVNQLD
Cl APVFTKKMYIGGVSEDAKMFSSVLKVKADDKDTGNYSAMQYRLIIPPIKDGKEGFVIEAYTGLIKTAMLFKNMRRSYFKFQVIATDNYGKGLSSKADVLVSVVNQLD
Lsd APVFTKKMYIGGVSEDARMFSSVLKVKADDKDTGNYSAMQYRLIIPPIKDGKEGFVIEAYTGLIKTAMLFKNMRRSYFKFQVIATDDYGKGLSSKADVLVSVVNQLD
Cb APVFTKKMYIGGVSEDARMFSSVLKVKANDKDTGNYSAMQYRLIIPPIKDGKEGFVIEAYTGLIKTAMLFKNMRRSYFKFQVIATDDYGKGLSSKAEVLVSVVNQLD
Pv APVFTKKLYIGGVSEDARMFSSVMKVKAKDKDMGNYSAMQYRLIIPPIKDGKEGFVIEPYTGLIKTAMLFKNMRRSYFKFQVIATDNYGKGLSNKSDVLVSVVNQLD
Ac APLFTRKLYIGGVSEDARMFSSVMKVKASDRDTGNYSAMQYRLIIPPIKDGKEGFVIEPYSGLIKTAMLFKNMRRSYFKFQVIATDNYGKGLSNKSDVLVSVVNQLD
Cp APVFTKKLYIGGVSEDARMFASVLRVKADDKDTGNYSAMQYRLIIPPIKDGKEGFVIEAYTGLIKTAMLFKNMRRAYFKFQVIATDNYGKGLSSKSDVLVSVVNQLD
Dr PPVFSRQVYIGGVTEDTKTFTTVLKIVATDVDTGNYSKMAYRLIIPPTTEGQDSFVIEPYTGVIKSAIMFRNMRRSYFKFQVVATDDYGKGLTSKADVVVSVVNALD
Ch PPLFTKPLYLGGVTEDAKTFTSVLQVQALDKDTGNYSAMQYRLIIPPTADGKDSFVIEPYSGVLKTAIMYRNMRRSYFKFQVVATDNYGAGLSSSTEVVVSVVNQLD
Am PPVFTKMFYLAGVAEDAKTFTSVLQVQALDKDTGNYSAMHYHLIIPPTADGKDSFVIEPYTGVIKTAIMYRNMRRSYFRFDVIATDNYGEGLSSSAQVVVSVVNQLD
Cm APVFTRPLYLGGVAEDAKTFTSVLQVEIEDQDTGNYSAVQYRLIIPPSKDGKDGFVIEAYTGLIKSAITFRNMRRSYFKFEVIATDNYGTGLSSSAQVVVSVVNELD
A A B B 3 10 C D E F 3 10 G 3 10
MAD12
IS20 starts
1230 1240 1250 1260 1270 1280 1290 1300 1310 1320 1330 1340 1350
Hs1 MQVIVSNVPPTLVEKKIEDLTEILDRYVQEQIPGAKVVVESIGARRHGDAFSLEDYTKCDLTVYAIDPQTNRAIDRNELFKFLDGKLLDINKDFQPYYGEGGRILEIRTPEAVTSIKKRGESLGYTE
Hs2 MQVIVSNVPPTLVEKKIEDLTEILDRYVQEQIPGAKVVVESIGARRHGDAFSLEDYTKCDLTVYAIDPQTNRAIDRNELFKFLDGKLLDINKDFQPYYGEGGRILEIRTPEAVTSIKKRGESLGYTE
Tt MQVIVSNVPPTLVERRIEELTEILDRYVQEQIPGSKVVVENVGARRHGDAFSLEDYTKCDLTVYAIDPQTNRAIDRHELFKFLDGKLLDINKDFQPYYGEGGRILEIRPPAAVTSIKKRGESLGYTE
Ss MQVIVSNVPPTLVEKKIEDLTEILDRYVQEQIPGAKVVVESIGARRHGDAFSLEDYTKCDLTVYAIDPQTNRAVDRNELFKFLDGKLLDINKDFQPYYGEGGRILEIRTPEAVTSIKKRGESLGYTE
Clf MQVIVSNVPPTLVEKKIEDLTEILDRYVQEQIPGAKVVVESIGARRHGDAFSLEDYTKCDLTVYAIDPQTNRAIDRNELFKFLDGKLLDINKDFQPHYGEGGRILEIRTPEAVTSIKKRGESLGYTE
Mm MQVIVSNVPPTLVEKKIEDLTEILDRYVQEQIPGAKVVVESIGARRHGDAYSLEDYSKCDLTVYAIDPQTNRAIDRNELFKFLDGKLLDINKDFQPYYGEGGRILEIRTPEAVTSIKKRGESLGYTE
Dr2 MQVIVSNVPPTLVEKKIEELTEILDRYVQEQIPGSKVVVESIGARRHGDAFSLEDYTKCDLTVYAIDPQTNRAIDRNELFKFLDGKLLDINKDFQPHYGEGGRILEIRTPEAVTSIKKRGESLGYTE
Gg MQVIVSNVPPTLVEQNKDQLIGILERYVQDQIPGATVVVESIGARRFGDGYSEEDYTKSDLMVYAIDPQTNRAIMRNELFKFLDGKLLDINKEFQPYLGQGGRILEIRTPDVVANVKKQAQAVGYTE
Cl MQVIVSNVPPTLVEQNKEQLIGILERYVQDQIPGATVVVESIGARRFGDGYSEEDYTKSDLMVYAIDPQTNRAIMRNELFKFLDGKLLDINKEFQPYLGQGGRILEIRTPDVVANVKKQAQAVGYTE
Lsd MQVIVSNVPPTLVEQNKDQLIGILERYVQAQIPGATVVVESIGARRFGDGYSEEDYTKSDLMVYAIDPQTNRAIMRNELFKFLDGKLLDINKEFQPYLGQGGRILEIRTPDVVANVKKQAQAVGYTE
Cb MQVIVSNVPPTLVEQNKDQLIGILERYVQDQIPGATVVVESIGARRFGDGYSEEDYTKSDLMVYAIDPQTNRAIMRNELFKFLDGKLLDINKEFQPYLGQGGRILEIRTPDVVANVKKQAQAVGYTE
Pv MQVIVSNVPPTLVEQNKDQLIGILERYVQDQIPGAKVVVESIGARRYGDGYSEEDYLKSDLMIYAIDPQTNRAIMRNELFKFLDGKLLDINKEFQPYLGQGGRILQIRTPDVVANVKKQAQAVGYTE
Ac MQVIVSNVPPTIVEQHKDELIGILERYVQDQIPGAKVVVESIGARRFGDGYSEEDYLKSDLMIYAIDPQTNRAIMRNELFKFLDGKLLDINKEFQPYLGQGGRILEIRTPDVVANVKKQAQAVGYTE
Cp MQVIVSNVPPTLVEQNKDQLIGILERYVQDQIPGAAVVVESIGARRFGHGYSEEDYSKSDLMIYAIDPQTNRAIMRNELFKFLDGKLLDINKEFQPYLGQGGRILEIRTPDVVANVKKQAQAVGYTE
Dr MQVVVSNVPPTVVEENKEQLISILERYVQDQIPGAKVIVESIGPRRHGEGYELEDYSKSDLQVYAIDPLTNRAISRQELFKFLDGKILDINKEFQPYLGEGGRILEIRSPDIVATVKKAAQAVGYTE
Ch MQIVVSNVSPTMVEQNKDQLMRILERYVQDQIPGAKVIVESIGPRRYGDSFEQEDYTKSDLMVYAIDPLTNRALSRQELYKFLDGKLLDINKEFQPYLGRGGRILEIRTPDLVANVKKSVQTVGYTE
Am MQVVVSNVPPTVVEQNKEQLIGILERYVQDQIPGAKVVVESIGPRRYGDTYDQEDYTKSDLMVYAIDPMTNRALSRQELFKFLDGKLLDINKEFQPYLGRGGRILEIRTPDVVQNVKKAVQSVGYTE
Cm MQVVVSNVPPTLVEQNKDQLIRILERYVQDQIPGATVVVESIGPRKHGDGFQEEDYSKSDLMVYAIDPLTNRAISRNELFKFLDGKLLDINKEFQSYLGQGGRILEIRTPDVVSNVKKQAQAVGYTE
3 10

Fig. S1. Sequence alignment of PCDH15 ectodomains from different species. Multiple sequence alignments comparing sequences of each PCDH15 EC repeat from 17 different species and two different human isoforms (*SI Appendix*, Table S2). Each alignment is colored by sequence similarity with white being the lowest similarity and blue being the highest (see *SI Appendix,* Methods). Some columns may not be colored if deletions or changes to residue type are present (e.g. polar amino acid to hydrophobic). Ca^{2+}-binding motif sequences are labeled on top of each alignment, with orange color for atypical motifs. Ca^{2+}-binding motifs of an EC repeat coordinating the N-terminal Ca^{2+} ions are designed as "top" while the Ca^{2+}-binding motifs coordinating C-terminal Ca^{2+} ions are designed as "bottom". Disease mutation sites are highlighted with yellow circles. Predicted sites of N- and O-linked glycosylation are marked with red and cyan circles, respectively. Experimentally observed glycosylation sites are marked with red and cyan triangles. Annotations related to various *mm* PCDH15 isoforms (labeled IS-1 to IS-26) are marked with grey triangles above each alignment. UniProt accession numbers for IS1-26 are Q99PJ1-1 to Q99PJ1-26, respectively. Secondary structure elements are displayed underneath each alignment. Species were chosen based on sequence availability and taxonomical diversity.

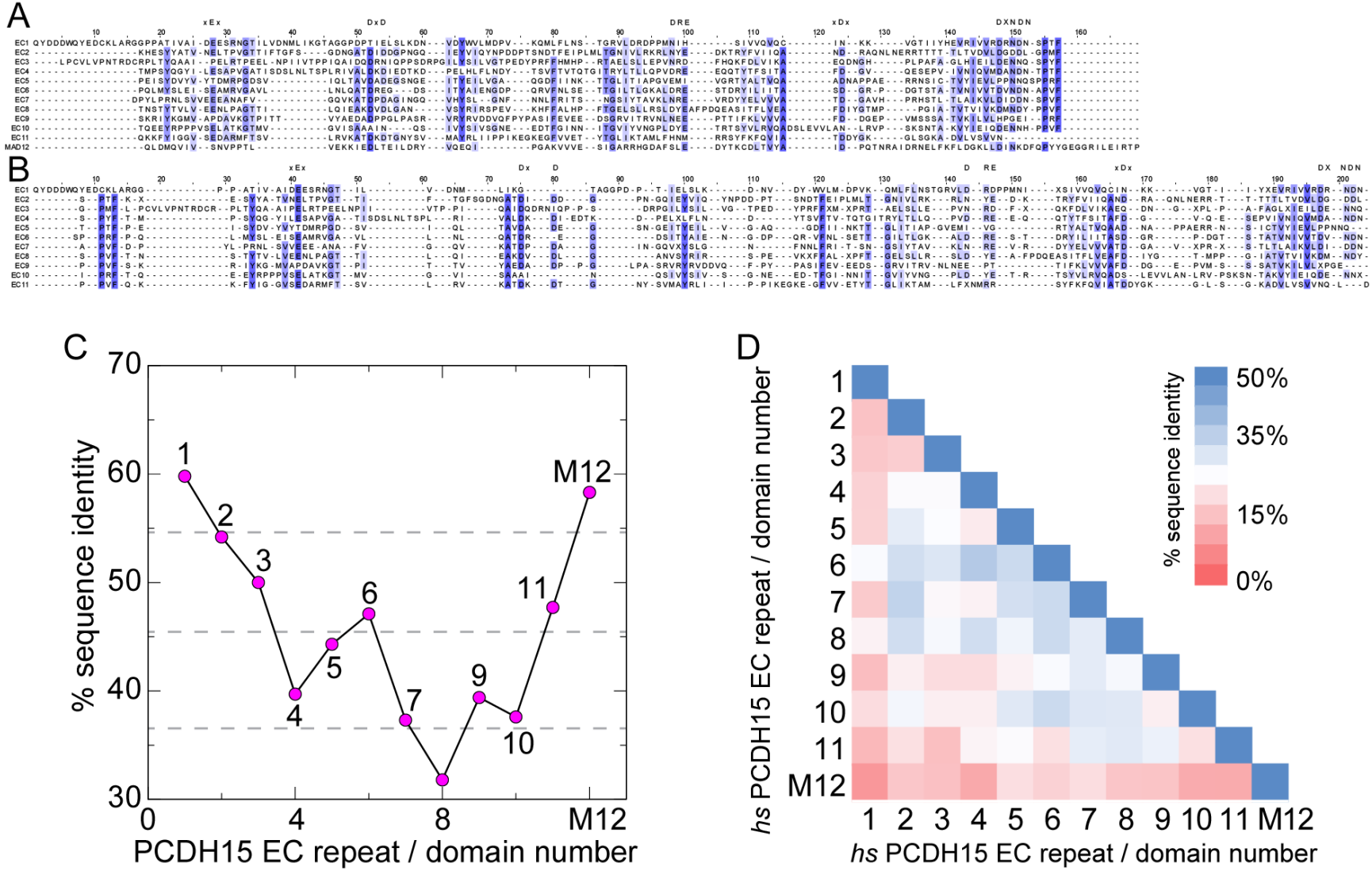

Fig. S2. Sequence alignments and conservation for PCDH15 EC repeats and MAD12. (*A*) Pairwise multiple sequence alignment of *hs* PCDH15 CD1-1 (NP_001136235.1) EC1 to MAD12. (*B*) Structure-based sequence alignment of PCDH15 CD1-1 EC1-EC11 repeats. Ca^{2+}-binding motif sequences are labeled on top of the alignments. (*C*) Plot of percent sequence identity of each PCDH15 EC repeat and MAD12 (M12) among 17 species against repeat/domain number (*SI Appendix,* Table S2). The most conserved regions of the protein include EC1 and MAD12, whereas EC8 is the least conserved. The average sequence identity is 45.6 ± 8.9% (gray dashed lines). (*D*) Heat map of a sequence identity matrix among EC-repeats and MAD12 for *hs* PCDH15 CD1-1 (NP_001136235.1). Sequence alignment from *A* was used as input to compute % sequence identity (see *SI Appendix*, Methods).

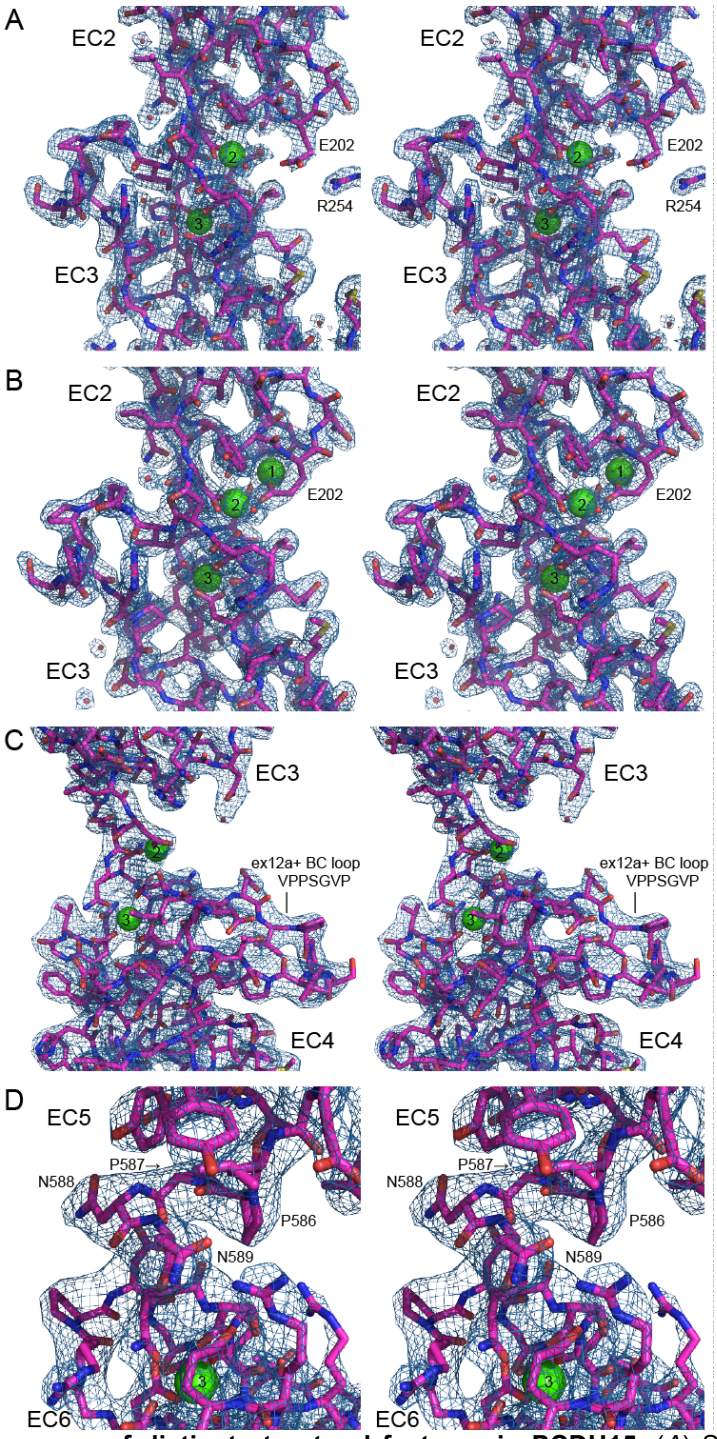

Fig. S3. Electron density maps of distinct structural features in PCDH15. (*A*) Stereo view of the 2Fo-Fc electron density map (blue mesh) of *hs* PCDH15 EC2-3 WT (PDB: 5ULY; chain D in purple) showing a detail of its linker region with two Ca^{2+} ions (green spheres). Water molecules are shown as red spheres. Residue p.E202 interacts with p.R254 and hence is not involved in Ca^{2+} coordination. (*B*) Similar stereo view for the *hs* PCDH15 EC2-3 V250N structure (PDB: 6EB5; chain A). The linker region has three Ca^{2+} ions with residue p.E202 coordinating the ion at site 1. Notably, the cysteine loop carrying p.R254 is too flexible in the absence of the X-dimer interface and is not seen in this structure. (*C*) Stereo view of the 2Fo-Fc electron density map (shown as in *A*) for the *hs* PCDH15 EC3-5 ex12a+ structure highlighting the enlarged BC loop in EC4 (p.V(414+1)PPSGVP(414+7)). (*D*) Stereo view of the 2Fo-Fc electron density map (shown as in *A*) for the EC5-6 linker region in the *mm* PCDH15 EC4-7 structure (PDB: 5W1D). All maps are contoured at 2.0 σ.

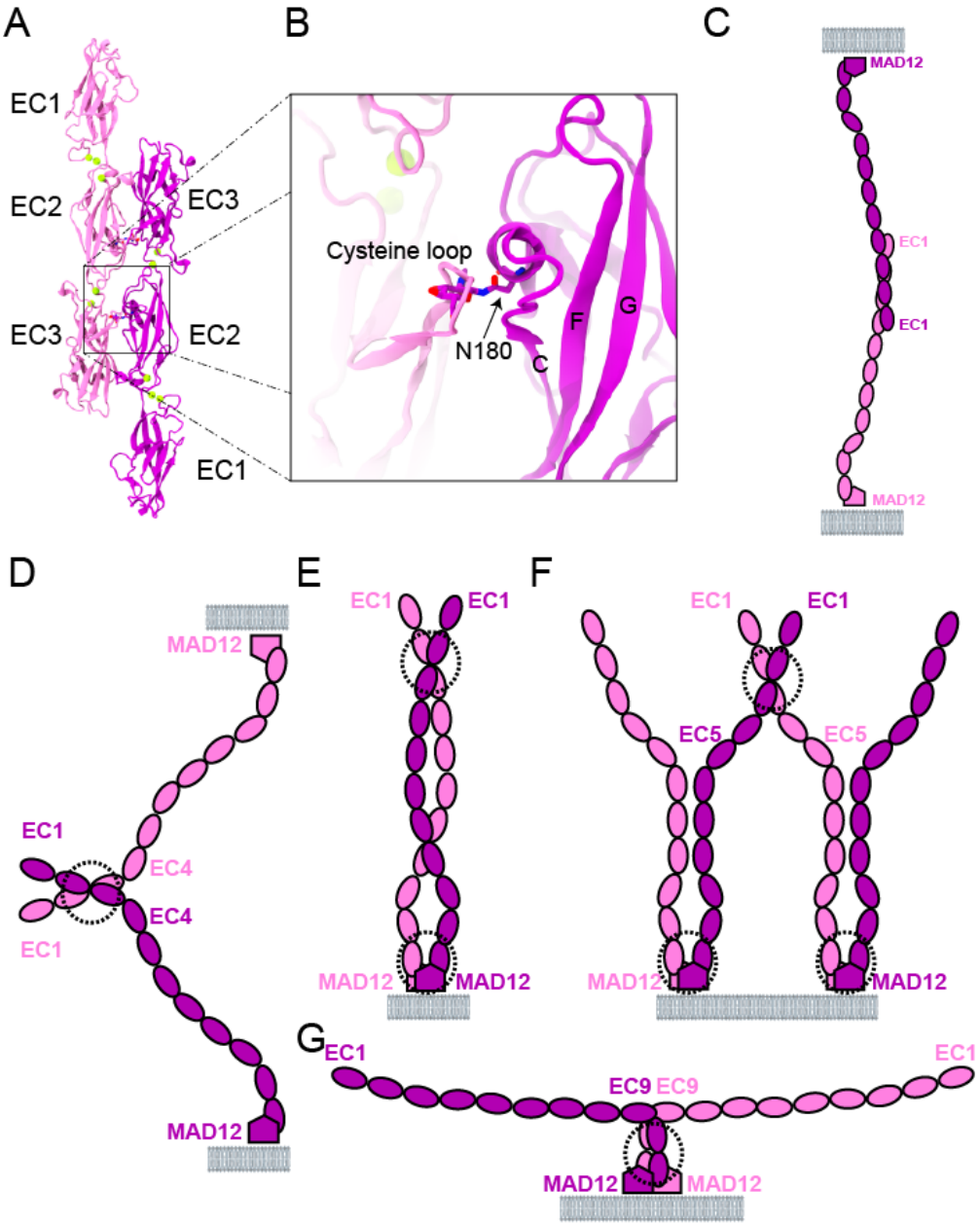

Fig. S4. Glycosylation site at an antiparallel PCDH15 dimer interface and schematics of various potential modes of PCDH15 dimerization. (*A*) To probe the location and effects of potential glycosylation sites on the antiparallel dimer structure of *hs* PCDH15 EC1-3 G16D/N369D/Q370N (PDB: 6MFO; protein expressed in bacteria), the glycosylated *mm* PCDH15 EC1-3 structure (PDB: 6CV7; protein expressed in mammalian cells) (43) was superposed on the structure of the antiparallel dimer. Ribbon representation of the *mm* PCDH15 EC1-3 monomers (mauve and purple) forming an antiparallel *trans* dimer highlighting a steric clash (black box). (*B*) Detail of the cysteine loop clashing with p.N180 carrying a sugar moiety. The same cysteine loop is not visible in the *hs* PCDH15 EC1-3 G16D/N369D/Q370N structure (PDB: 6MFO). (*C*) Schematic representation of a potential antiparallel *trans* PCDH15-PCDH15 tip link if the cysteine loop rearranges and the aperture angle between EC2-3 repeats decreases to avoid steric clashes. (*D-F*) Modes of *trans* (*D*) and *cis* (*E-F*) dimerization that can be mediated by the PCDH15 EC2-3 X-dimer interface presented here and in Dionne *et al* (43). Immature transient PCDH15 tip links (87, 88) might adopt the *trans* configuration shown in *D* (similar to the rightmost configuration in Fig. 3*C*). Dashed circles indicate sites of dimerization. (*G*) Parallel dimerization mediated by MAD12 (5, 47) along with a fully bent EC9-10 linker (6) results in monomers pointing in opposite directions and parallel to the membrane plane.

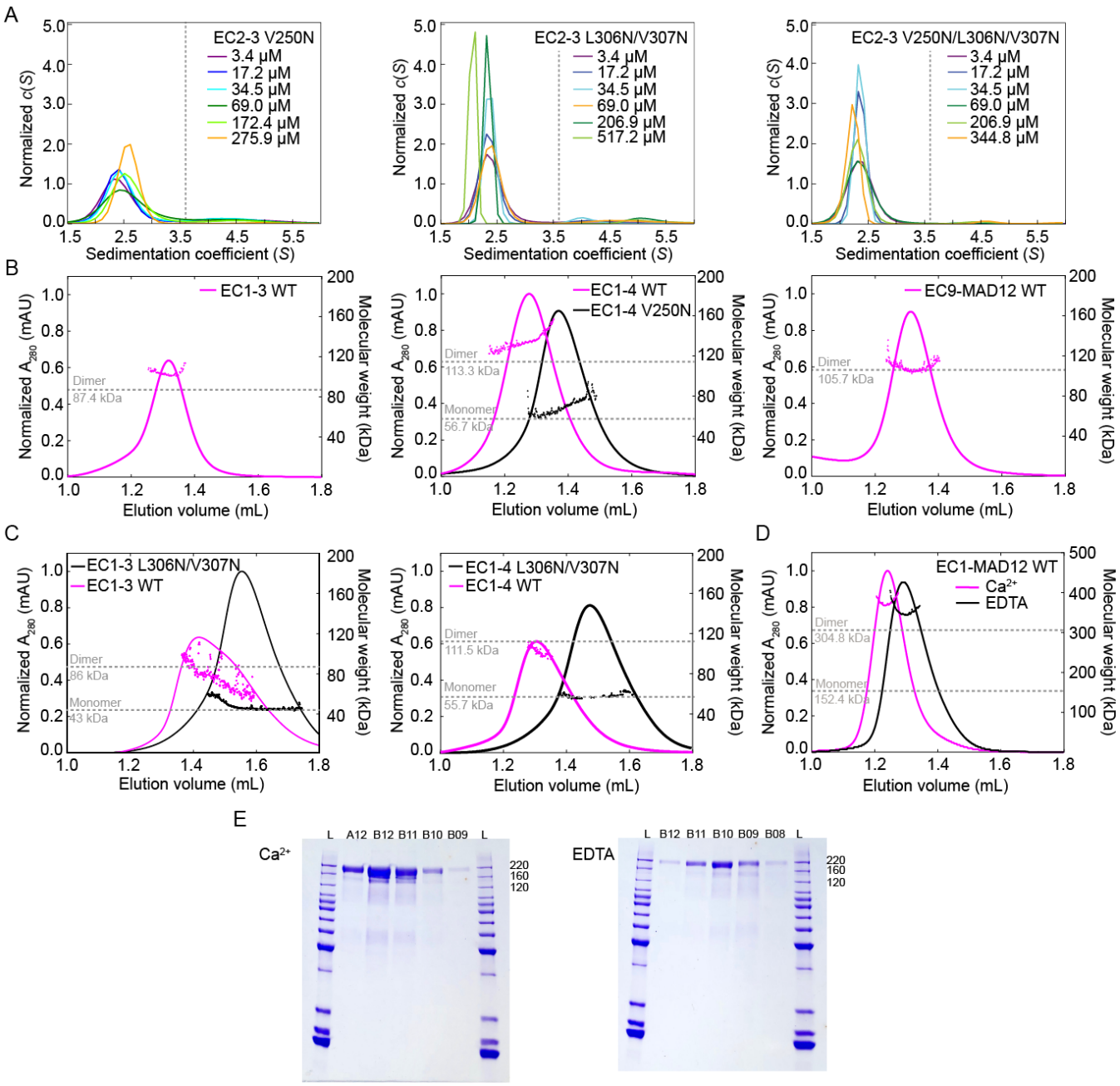

Fig. S5. Dimerization of PCDH15 in solution. (*A*) Results from AUC experiments for point mutants in the *hs* PCDH15 EC2-3 dimer interface. Plots show normalized sedimentation coefficient distributions *c*(*S*) at varying concentrations of bacterially expressed *hs* PCDH15 EC2-3 p.V250N (left panel), p.L306N/p.V307N (middle), and p.V250N/p.L306N/p.V307N (right). Dotted gray line represents the sedimentation coefficient (*S*) value of WT dimer (Fig. 2*C*). All mutants are monomeric in solution. (*B*) SEC-MALS results for glycosylated *mm* PCDH15 EC1-3 WT (left panel), *mm* PCDH15 EC1-4 ex12a- WT and p.V250N mutant (middle), and *mm* PCDH15 EC9-MAD12 (right) protein fragments using a Superdex S200 3.2/30 column. Horizontal dashed lines indicate theoretical molar mass for unglycosylated monomer and dimer. (*C*) SEC-MALS results for bacterially expressed *hs* PCDH15 EC1-3 WT and p.L306N/p.V307N mutant (left panel), and *hs* PCDH15 EC1-4 WT and p.L306N/p.V307N mutant (right panel) using a Superdex S200 3.2/30 column. (*D*) SEC-MALS results for mammalian expressed *mm* PCDH15 EC1-MAD12 ex12a- in the presence of Ca^{2+} (magenta) and EDTA (black) using a Superose 6 3.2/30 column. Notably, the protein is still dimeric in the absence of Ca^{2+}. (*E*) Coomassie stained SDS-PAGE of eluted fractions from experiments in *D*.

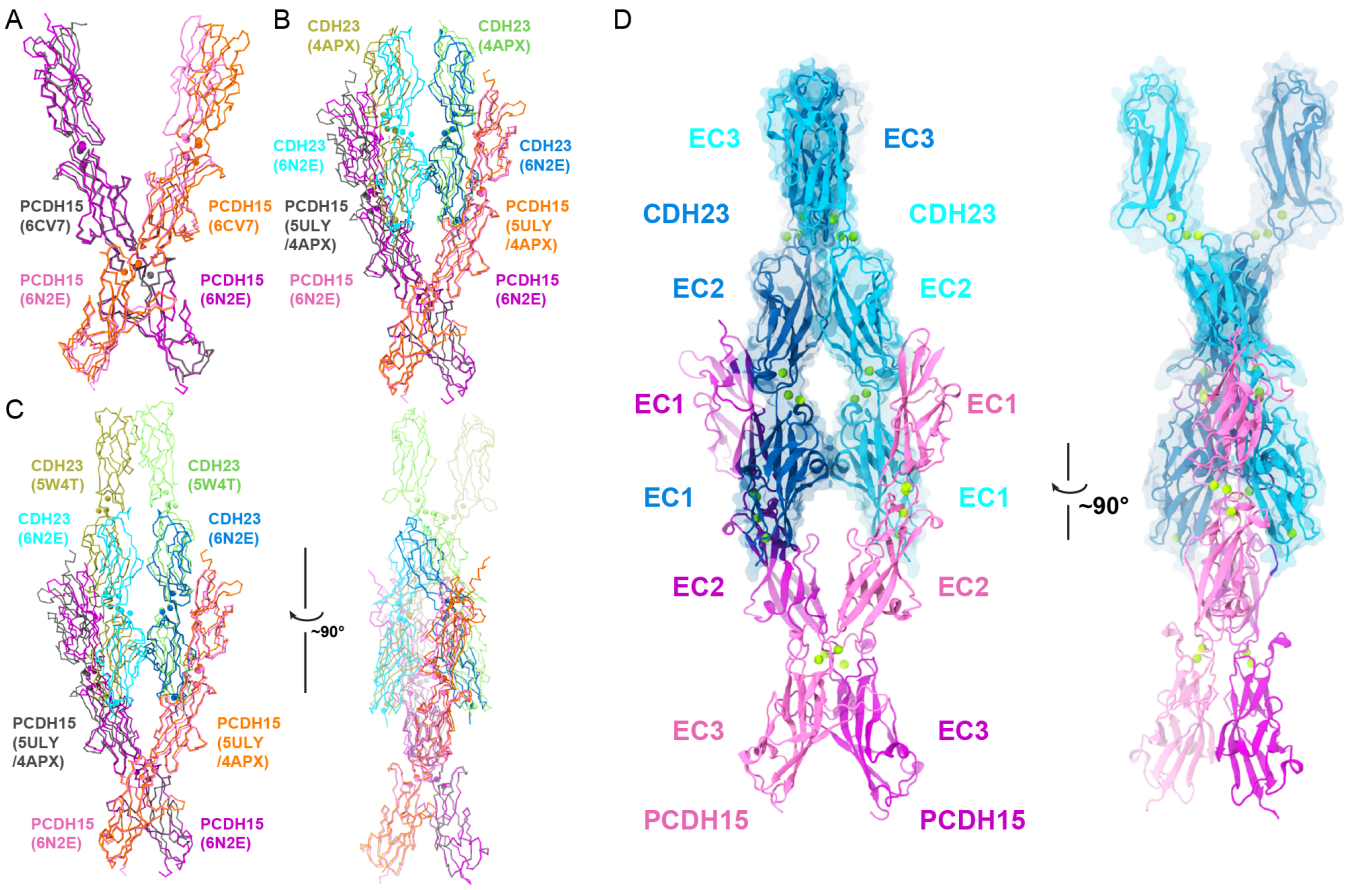

Fig. S6. Structural comparison of PCDH15 X-dimer based tetrameric assemblies and a model of PCDH15 EC1-3 in complex with CDH23 EC1-3. (*A*) Superposition of *mm* PCDH15 EC1-3 (PDB: 6CV7; gray and orange) (43) and *hs* PCDH15 EC1-3 G16D/N369D/Q370N (PDB: 6N2E; mauve and purple; *mm* CDH23 EC1-2 T15E is not shown). Repeats EC3 from one monomer (gray and purple) were structurally aligned. The "scissor" is less open in the structure when PCDH15 is bound to CDH23 EC1-2 (PDB: 6N2E), with a smaller separation between EC1-2 repeats of the two PCDH15 monomers. (*B*) Superposition of the *hs* PCDH15 EC1-3 G16D/N369D/Q370N (mauve and purple) + *mm* CDH23 EC1-2 T15E (blue and cyan) tetramer complex structure (PDB: 6N2E) with a tetramer model (orange, gray, green, and tan) created by using the X-dimer conformation observed in *hs* PCDH15 EC2-3 (PDB: 5ULY) and the *mm* PCDH15 EC1-2 + *mm* CDH23 EC1-2 handshake interaction (PDB: 4APX) (3). A similar model was also reported by Dionne *et al* (43). In the tetrameric crystal structure, repeat EC1 of PCDH15 from one monomer moves towards the other, thus bringing the two CDH23 EC1-2 molecules closer to each other. (*C*) Superposition of the *hs* PCDH15 EC1-3 G16D/N369D/Q370N (mauve and purple) + *mm* CDH23 EC1-2 T15E (blue and cyan) tetramer complex structure (PDB: 6N2E) with a tetramer model (orange, gray, green, and tan) created by incorporating the *dr* CDH23 EC1-3 structure (PDB: 5W4T) (26) to the tetramer model generated in panel *B* through alignment of CDH23 EC1-2 monomers. (*D*) A model of CDH23 EC1-3 (blue and cyan) in complex with the PCDH15 EC1-3 X-dimer (mauve and purple). Ca^{2+} ions are shown in green. Model was generated by aligning CDH23 EC1-2 repeats from the *dr* CDH23 EC1-3 structure (PDB: 5W4T) (26) and from the *hs* PCDH15 EC1-3 G16D/N369D/Q370N (mauve and purple) + *mm* CDH23 EC1-2 T15E (blue and cyan) tetramer complex structure (PDB: 6N2E). This tetrameric arrangement suggests that CDH23 dimerization involves repeats beyond EC3.

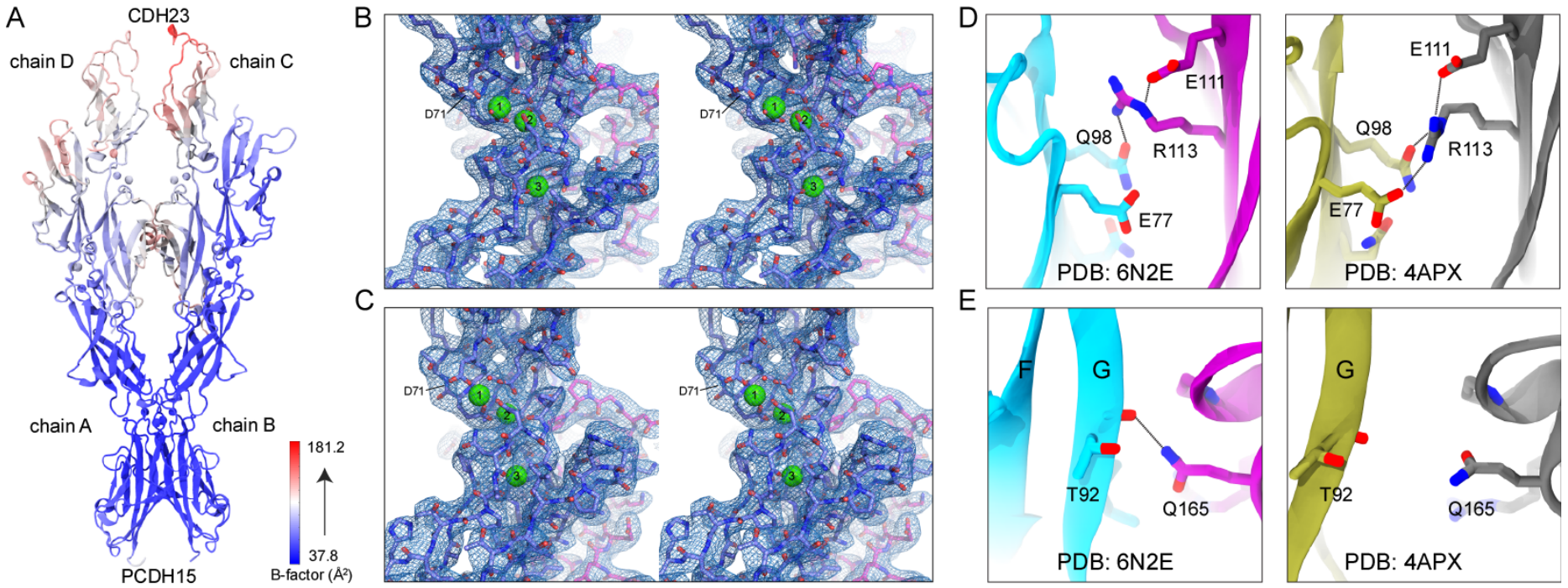

Fig. S7. Flexibility and presence of CDH23 monomers in the tetramer structure. (*A*) Ribbon diagram of the *hs* PCDH15 EC1-3 G16D/N369D/Q370N + *mm* CDH23 EC1-2 T15E structure (PDB: 6N2E) colored by B-factor varying from blue (low) to red (high). The EC2 repeats of CDH23 (chain C and D) and the EC1 repeat of PCDH15 (chain A) have large B factor values (red). (*B-C*) Stereo representations of the composite omit electron density map for CDH23 EC1-2 linkers contoured at 0.75 σ (blue mesh) for chains C (top) and D (bottom), respectively. CDH23 residues are depicted as blue sticks, PCDH15 residues are depicted as mauve sticks, Ca^{2+} ions are shown as green spheres. Ca^{2+} ions are clearly seen in the map, corroborating the presence of CDH23 in the complex. (*D*) Left panel shows details of the interface between CDH23 (chain C, cyan) and PCDH15 (chain D, purple) in the *hs* PCDH15 EC1-3 G16D/N369D/Q370N + *mm* CDH23 EC1-2 T15E structure (PDB: 6N2E). Residue p.R113 in PCDH15 does not interact with p.E77 in CDH23, as also observed for a handshake structure involving isoform N2 of PCDH15 (PDBs: 4XXW) (89). Right panel shows the same detail for the *mm* PCDH15 EC1-2 (gray) + *mm* CDH23 EC1-2 (tan) complex (PDB: 4APX) (3). Residue p.R113 is oriented towards the interface forming more favorable interactions with p.E77. (*E*) Left panel shows residue p.Q165 of PCDH15 making a favorable hydrogen bond with the backbone carbonyl of CDH23's p.T92 (β-strand G of EC1) in the *hs* PCDH15 EC1-3 G16D/N369D/Q370N + *mm* CDH23 EC1-2 T15E structure (PDB: 6N2E). The same interaction is not observed in the structure of the *mm* PCDH15 EC1-2 + *mm* CDH23 EC1-2 complex (PDB: 4APX) (3) due to an increased separation between the CDH23 N-terminus and the PCDH15 EC2 repeat. Colors as in *D*.

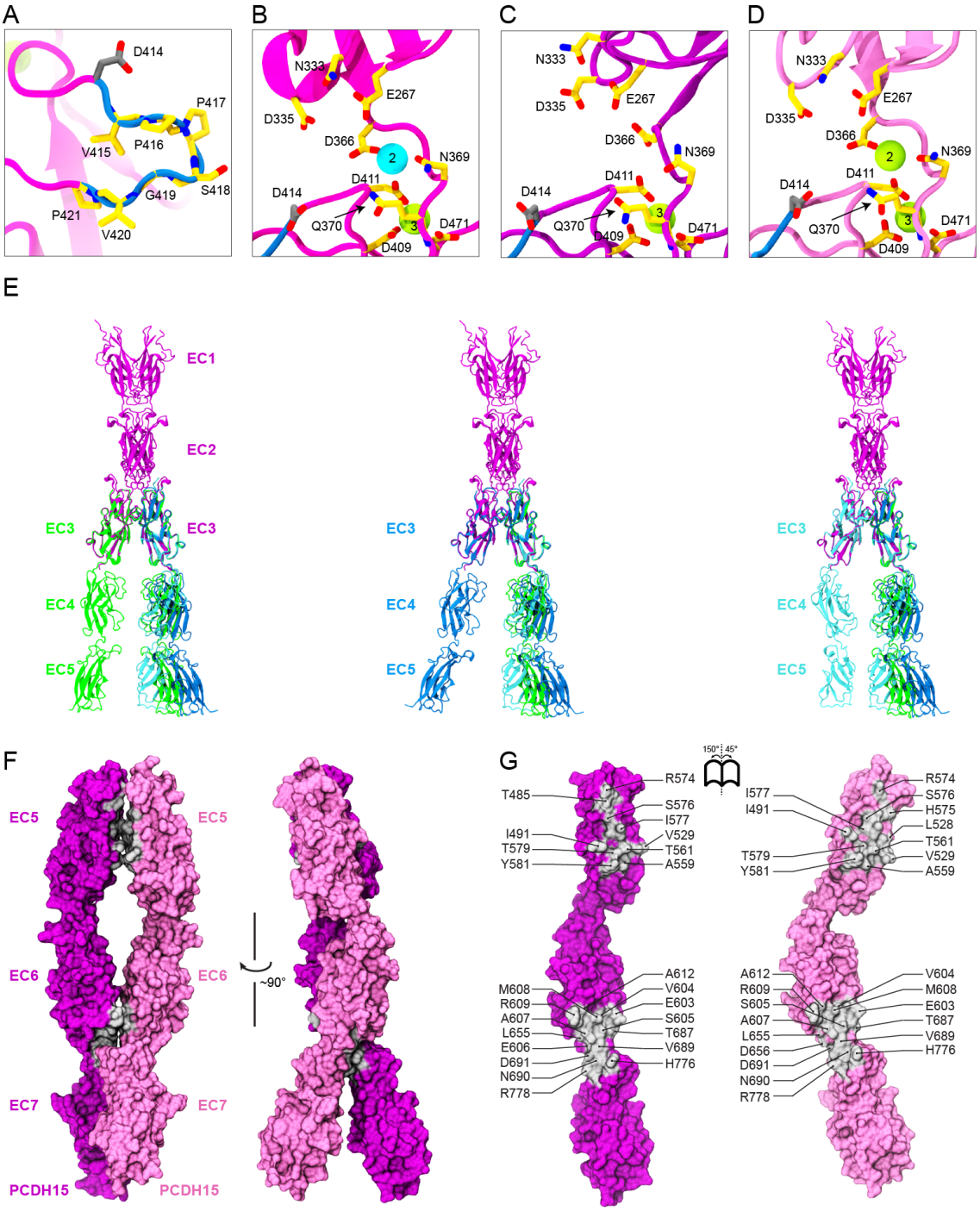

Fig. S8. Structural details of the PCDH15 EC3-4 linker, conformational diversity of PCDH15's ectodomain, and a crystallographic interface in PCDH15 EC5-7. (*A*) Detail of the insertion p.V(414+1)PPSGVP(414+7) encoded by exon 12a (blue backbone). Relevant residues are shown in stick representation and labeled. Some backbone atoms are omitted for clarity. Residue p.D414, thought to be under positive selection (62) and involved in inherited deafness (63) is shown in gray. (*B-D*) Detail of *hs* PCDH15 EC3-4 linker region for the three different molecules observed in the asymmetric unit of the *hs* PCDH15 EC3-5 ex12a+ structure. Shown as in *A*. Sodium is in cyan. (*E*) Overlap of different conformations of *hs* PCDH15 EC3-5 ex12a+ (green, blue, cyan for different molecules in the asymmetric unit) and the PCDH15 monomers from the heterotetrameric *hs* PCDH15 EC1-3 G16D/N369D/Q370N + *mm* CDH23 EC1-2 T15E structure. All possible conformations are devoid of steric clashes and compatible with the X-dimer arrangement. (*F*) Molecular surface representation of two *mm* PCDH15 EC5-7 I582T monomers (mauve and purple) in the asymmetric unit. Two perpendicular views are shown. (*G*) Interaction surface exposed with interfacing residues listed and shown in silver.

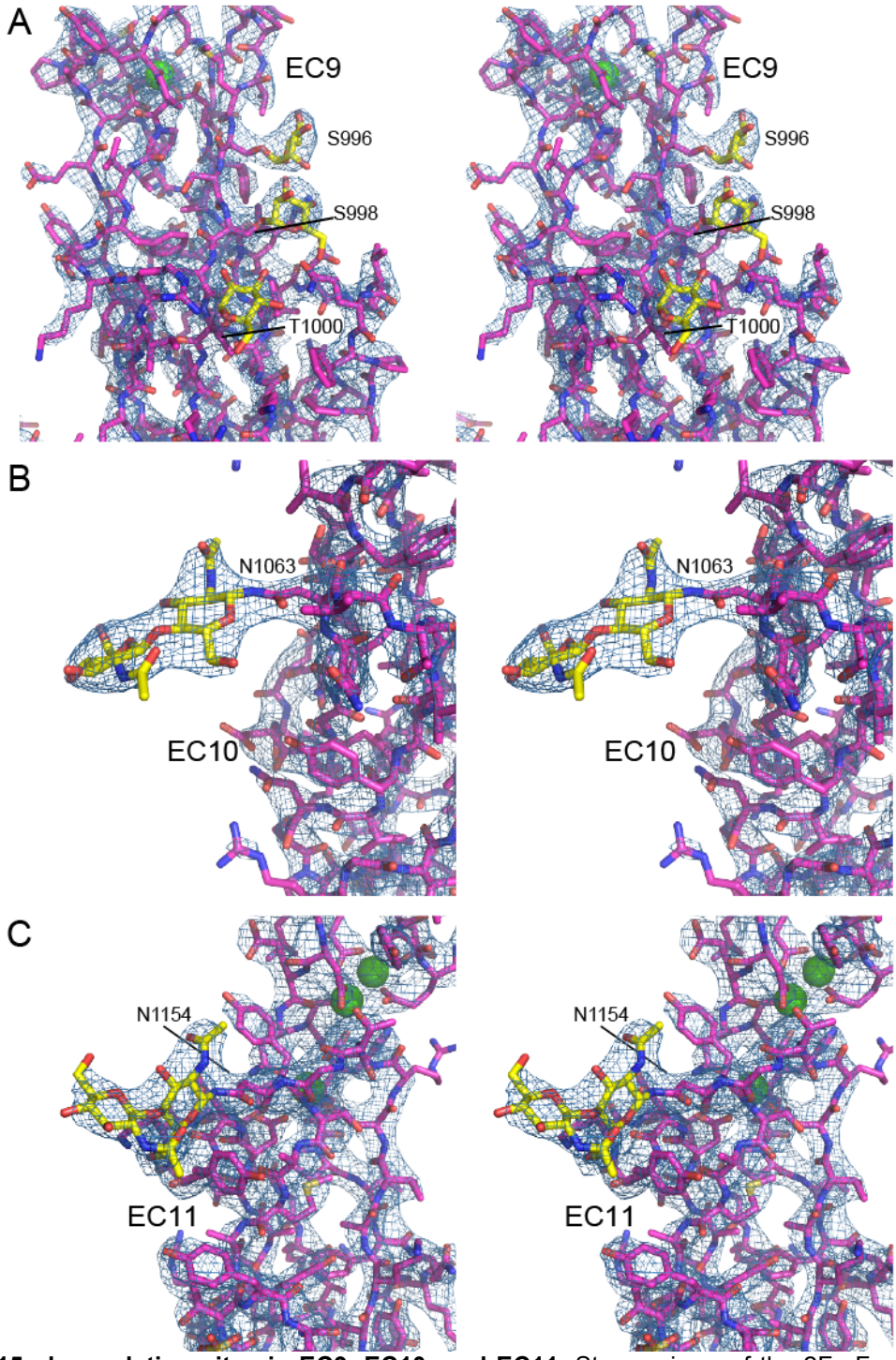

Fig. S9. PCDH15 glycosylation sites in EC9, EC10, and EC11. Stereo views of the 2Fo-Fc electron density map (blue mesh; contoured at 2.0 σ) for the *mm* PCDH15 EC9-MAD12 structure (PDB: 6EET). (*A*) Detail of glycosylation sites on EC9. (*B*) Detail of glycosylation site on EC10. (*C*) Detail of glycosylation site on EC11.

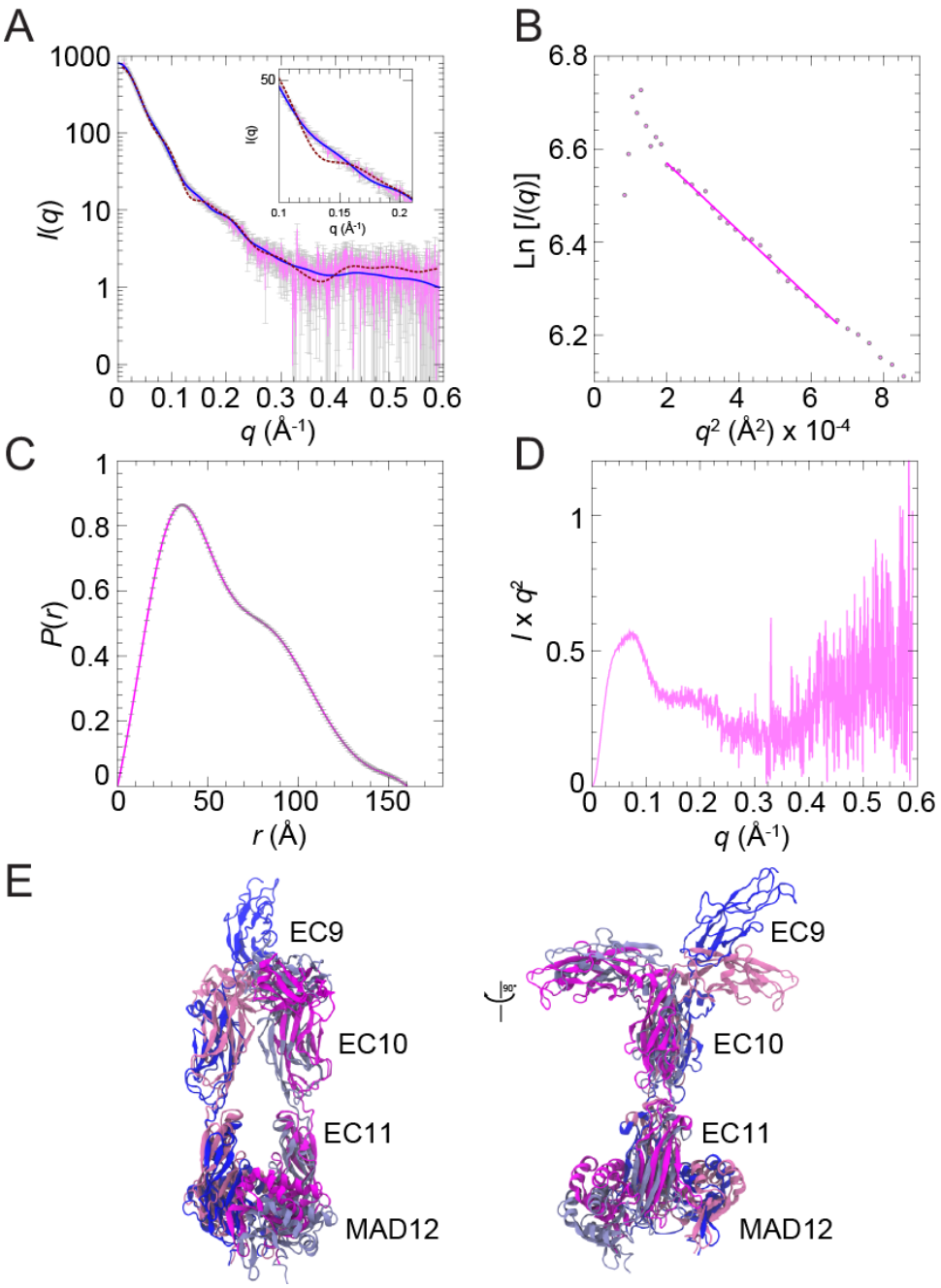

Fig. S10. Dimerization and flexibility of the PCDH15 EC9-MAD12 fragment determined by SAXS. (*A*) X-ray scattering intensity as a function of the scattering vector *q* (SAXS profile) for the bacterially produced *mm* PCDH15 EC9-MAD12. Predicted scattering intensities from the structure obtained with FoXS are shown in maroon-dashed lines (χ^2 = 6.52), while the theoretical scattering curve obtained from flexible refinement with SREFLEX is shown in blue (χ^2 = 1.38). (*B*) Guinier plot of SAXS data in the low *q* region. The magenta solid line shows the linear fit from which the gradient of the slope ($-R_g^2/3$) was used to estimate R_g. (*C*) Real-space pair distribution function *P*(*r*). (*D*) Kratky plot indicating the presence of folded and flexible protein. (*E*) Two views of a representative model of *mm* PCDH15 EC9-MAD12 from flexible refinement with SREFLEX (dark and light blue) superposed to the crystal structure of *mm* PCDH15 EC9-MAD12 (magenta and mauve).

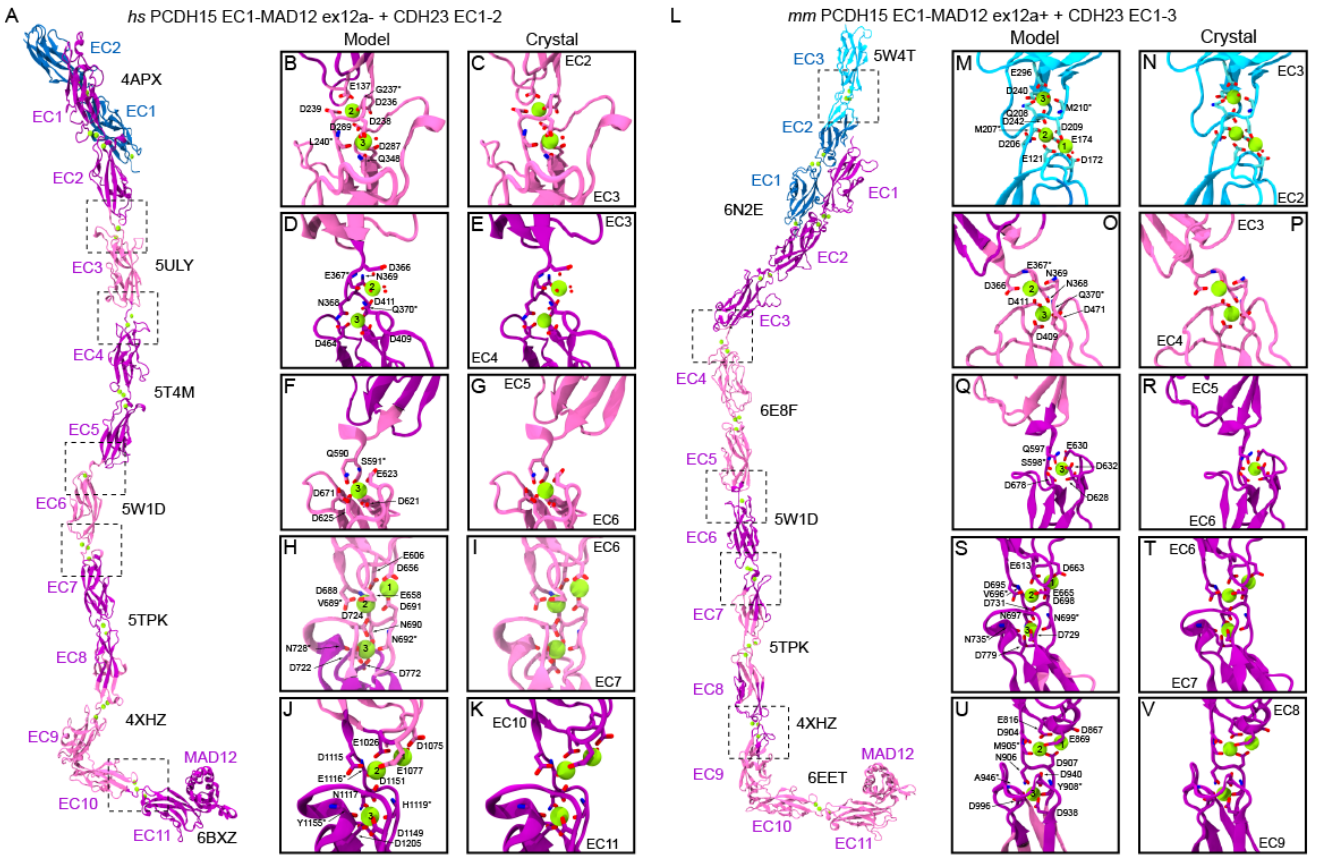

Fig. S11. Overall view and details of the complete *hs* and *mm* PCDH15 ectodomain models. (*A*) Ribbon representation of the entire *hs* PCDH15 EC1-MAD12 ex12a- ectodomain (mauve and purple) bound to *hs* CDH23 EC1-2 (blue). The alternating colors (mauve and purple) highlight different crystal structures used to assemble the model (PDB codes indicated for each in black). Regions inside the dotted boxes highlight select fusion points between crystal structures. Crystallographic water molecules (red spheres), Ca^{2+} ions (green spheres), and Ca^{2+}-coordinating residues at these points are highlighted and labeled in insets. For structures with multiple chains in the asymmetric unit the following chains were used: chain D of 5ULY; chain A of 5T4M; and chain C of 6BXZ. (*B-C*) Detail of the fused PCDH15 EC2-3 linker region in the model (PDBs: 4APX + 5ULY) and of the same linker region in a crystal structure (PDB: 5ULY). (*D-E*) Detail of the fused PCDH15 EC3-4 linker region in the model (PDBs: 5ULY + 5T4M) and of the same linker region in a crystal structure (PDB: 5T4M). (*F-G*) Detail of the fused PCDH15 EC5-6 linker region (PDBs: 5T4M + 5W1D) and of the same linker region in a crystal structure (PDB: 5W1D). (*H-I*) Detail of the fused PCDH15 EC6-7 linker region in the model (PDBs: 5W1D + 5TPK) and of the same linker region in a crystal structure (5W1D). (*J-K*) Detail of the fused PCDH15 EC10-11 linker region in the model (PDBs: 4XHZ + 6BXZ) and of the same linker region in a crystal structure (6BXZ). (*L*) Ribbon representation of the entire *mm* PCDH15 EC1-MAD12 ex12a+ ectodomain (mauve and purple) bound to *mm* CDH23 EC1-3 (blue and cyan). The alternating colors (mauve and purple; blue and cyan) highlight different crystal structures used to assemble the model (PDB codes indicated for each in black). Regions inside the dotted boxes highlight select fusion points between crystal structures. Crystallographic water molecules (red spheres), Ca^{2+} ions (green spheres), and Ca^{2+}-coordinating residues at these points are highlighted and labeled in insets. For structures with multiple chains in the asymmetric unit the following chains were used: chains B & C of 6N2E; chain A of 5W4T; and chain B of 6E8F. (*M-N*) Detail of the fused CDH23 EC2-3 linker region in the model (PDBs: 5W4T + 6N2E) and of the same linker region in a crystal structure (PDB: 5W4T), respectively. (*O-P*) Detail of the fused PCDH15 EC3-4 linker region in the model (PDBs: 6N2E + 6E8F) and of the same linker region in a crystal structure (PDB: 6E8F). (*Q-R*) Detail of the fused PCDH15 EC5-6 linker region (PDBs: 6E8F + 5W1D) and of the same linker region in a crystal structure (PDB: 5W1D). (*S-T*) Detail of the fused EC6-7 linker region in the model (PDBs: 5W1D + 5TPK) and of the same linker region in a crystal structure (5W1D). (*U-V*) Detail of the fused EC8-9 linker region in the model (PDBs: 4XHZ + 6EET) and of the same linker region in a crystal structure (4XHZ).

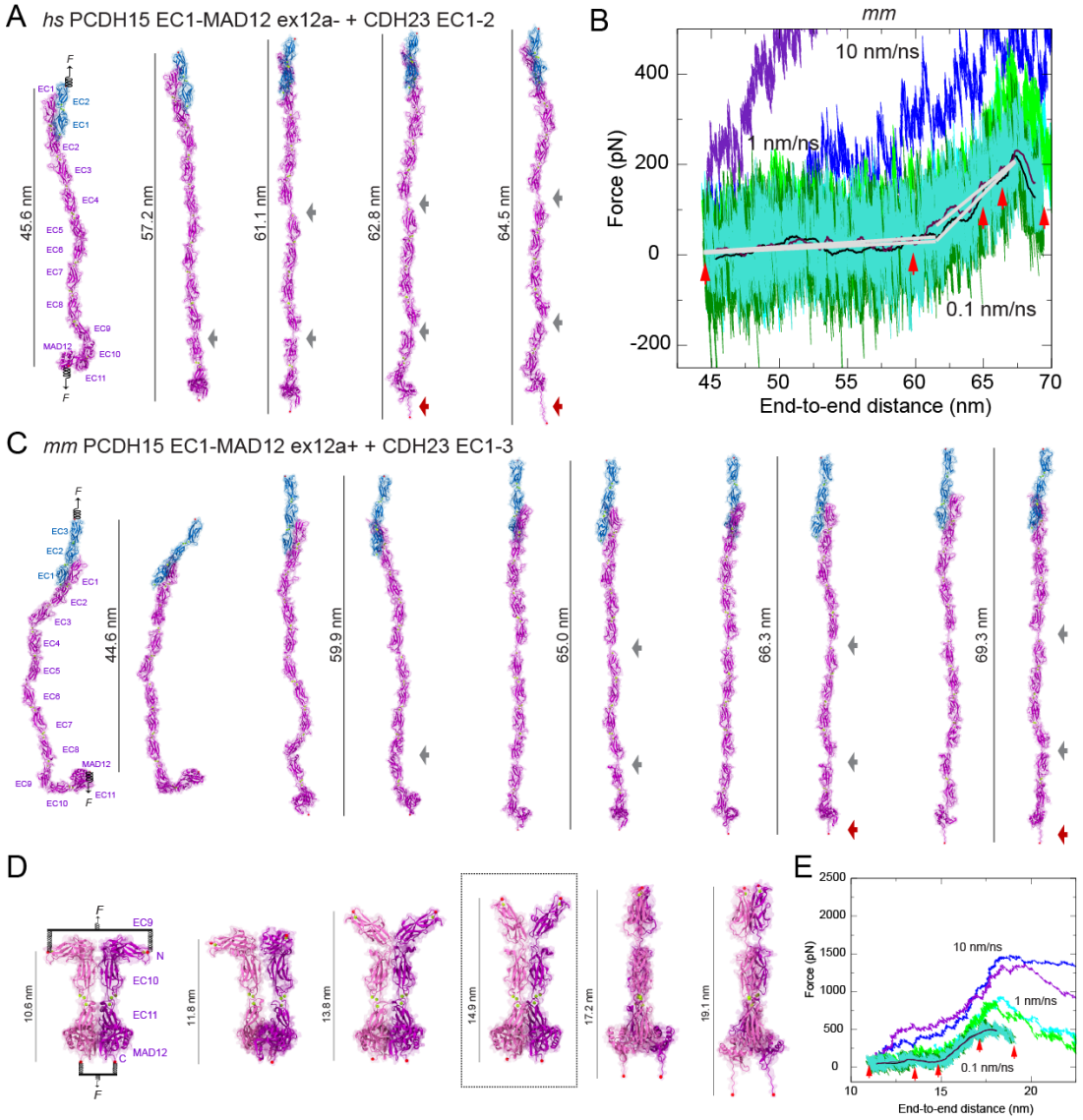

Fig. S12. Elasticity of the monomeric PCDH15 ectodomain and the dimeric PCDH15 EC9-MAD12. (*A*) Snapshots of the monomeric *hs* PCDH15 EC1-MAD12 ex12a- + CDH23 EC1-2 system during stretching simulation S1d (0.1 nm/ns; *SI Appendix*, Table S10). Stretched C-terminal Cα atoms are shown as red spheres. Springs indicate position and direction of applied forces. Gray arrows highlight stretching of PCDH15 EC linkers (EC9-10 followed by EC5-6). Dark red arrow indicates unfolding of PCDH15 MAD12's C-terminal end. Views are rotated versions of snapshots shown in Fig. 5*K* (~90°). (*B*) Force versus end-to-end distance for constant velocity stretching of *mm* PCDH15 EC1-MAD12 ex12a+ + CDH23 EC1-3 at 10 nm/ns (S2b, purple and blue), 1 nm/ns (S2c, bright green and cyan), and 0.1 nm/ns (S2d, dark green and turquoise; 10-ns running averages shown in black and maroon; gray lines are fits used to determine elasticity of the complex). Red arrowheads indicate time-points for simulation S2d illustrated in panel *C*. (*C*) Snapshots of the monomeric *mm* PCDH15 EC1-MAD12 ex12a+ + CDH23 EC1-3 system during stretching simulation S2d (0.1 nm/ns; *SI Appendix,* Table S10). Interestingly, straightening of the bent monomeric PCDH15 conformation, before any unfolding happens, is soft and leads to a ~15.5 nm smooth extension. (*D*) Snapshots showing the dimeric *mm* PCDH15 EC9-MAD12 system in its crystallographic conformation (left) and during stretching simulation S11d (0.1 nm/ns; *SI Appendix*, Table S10). Stretched N- and C-terminal Cα atoms are shown as red spheres. Stretching was carried out by attaching two slabs to springs that were in turn attached to the terminal ends of each protein monomer. Slabs were moved in opposite directions at constant speed through individual springs. Dashed box highlights conformation corresponding to a force minimum. (*E*) Force applied to each of the slabs versus protein separation for stretching simulations of *mm* PCDH15 EC9-MAD12 (simulation S11b-d). Traces are for constant velocity simulations at 10 nm/ns (purple and blue), 1 nm/ns (bright green and cyan), and 0.1 nm/ns (dark green and turquoise with 10-ns running averages in black and maroon). Red arrowheads indicate time-points for simulation S11d illustrated in panel *D*. The force profile shows a clear dip at 14.9 nm, suggesting the existence of an alternate stable state with semi-extended EC9 repeats (dashed box in *D*).

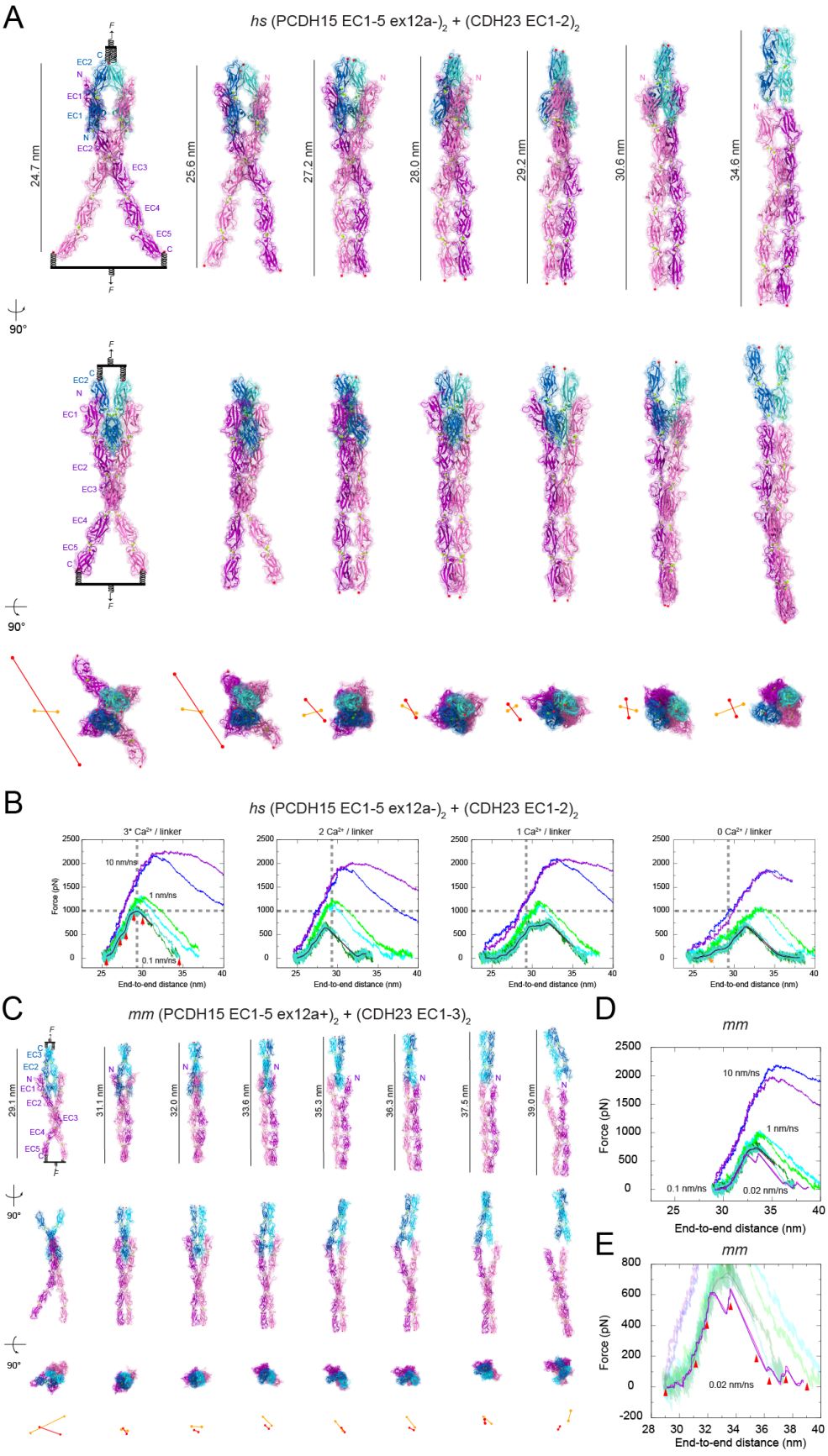
A
hs (PCDH15 EC1-5 ex12a-)2 + (CDH23 EC1-2)2
24.7 nm
25.6 nm
27.2 nm
28.0 nm
29.2 nm
30.6 nm
34.6 nm
EC1
EC2
EC3
EC4
EC5
90°
B
hs (PCDH15 EC1-5 ex12a-)2 + (CDH23 EC1-2)2
3* Ca2+ / linker
2 Ca2+ / linker
1 Ca2+ / linker
0 Ca2+ / linker
10 nm/ns
1 nm/ns
0.1 nm/ns
Force (pN)
End-to-end distance (nm)
C
mm (PCDH15 EC1-5 ex12a+)2 + (CDH23 EC1-3)2
29.1 nm
31.1 nm
32.0 nm
33.6 nm
35.3 nm
36.3 nm
37.5 nm
39.0 nm
D
mm
10 nm/ns
1 nm/ns
0.1 nm/ns
0.02 nm/ns
Force (pN)
End-to-end distance (nm)
E
mm
0.02 nm/ns
Force (pN)
End-to-end distance (nm)

Fig. S13. *In silico* strength of short *trans* heterotetrameric PCDH15 + CDH23 bonds. (*A*) Snapshots of the heterotetrameric *hs* (PCDH15 EC1-5 ex12a-)$_2$ and (CDH23 EC1-2)$_2$ system during stretching simulation S3d (0.1 nm/ns; *SI Appendix,* Table S10). Slabs were connected to stretching springs and moved in opposite directions. Label for N-terminus of one of the PCDH15 monomers highlights its rotation. Two perpendicular side views and a top view are shown in top, middle, and bottom panels. Position of C-terminal Cα atoms for PCDH15 and CDH23 monomers are shown next to top views in red and orange, respectively. Lines between these positions illustrate closing of parallel monomers as well as relative angle and rotations of PCDH15 with respect to CDH23 monomers observed throughout the trajectory. (*B*) Force applied to each of the slabs versus protein separation (see *SI Appendix,* Methods) for constant velocity stretching simulations of *hs* (PCDH15 EC1-EC5 ex12a-)$_2$ + (CDH23 EC1-2)$_2$ systems with all Ca^{2+}-binding sites occupied (S3b-d; 3 Ca^{2+} ions per linker except for PCDH15 EC2-3 and EC3-4 linkers), with 2 Ca^{2+} ions per linker (S4b-d; Ca^{2+}-binding sites 2 and 3), with 1 Ca^{2+} ion per linker (S5b-d; Ca^{2+}-binding site 3), and without bound Ca^{2+} ions (S6b-d). Traces are for constant velocity simulations at 10 nm/ns (purple and blue), 1 nm/ns (bright green and cyan), and 0.1 nm/ns (dark green and turquoise with 10-ns running averages in black and maroon). Gray dashed lines indicate magnitude and position of force peak at the slowest stretching speed tested with all Ca^{2+}-binding sites occupied. Red arrowheads in leftmost panel indicate time-points for simulation S3d illustrated in *A*. Orange arrowhead in rightmost panel indicates soft elastic response region. (*C*) Snapshots of the heterotetrameric *mm* (PCDH15 EC1-5 ex12a+)$_2$ and (CDH23 EC1-3)$_2$ system during stretching simulation in which slabs were connected to stretching springs and moved in opposite directions (S7e, 0.02 nm/ns, *SI Appendix,* Table S10, Movie S5). Side and top views are shown as in panel *A*. (*D*) Force applied to each of the slabs versus protein separation (see *SI Appendix,* Methods) for stretching simulations of *mm* (PCDH15 EC1-5)$_2$ and (CDH23 EC1-3)$_2$ (S7b-e). Traces are for constant velocity simulations at 10 nm/ns (purple and blue), 1 nm/ns (bright green and cyan), 0.1 nm/ns (dark green and turquoise with 10-ns running averages in black and maroon), and 0.02 nm/ns (10-ns running averages in magenta and indigo). (*E*) Detail of plot in panel *D.* A double-force peak during unbinding suggests the existence of an intermediate state. Red arrowheads indicate time-points for simulation S7e illustrated in panel *C*.

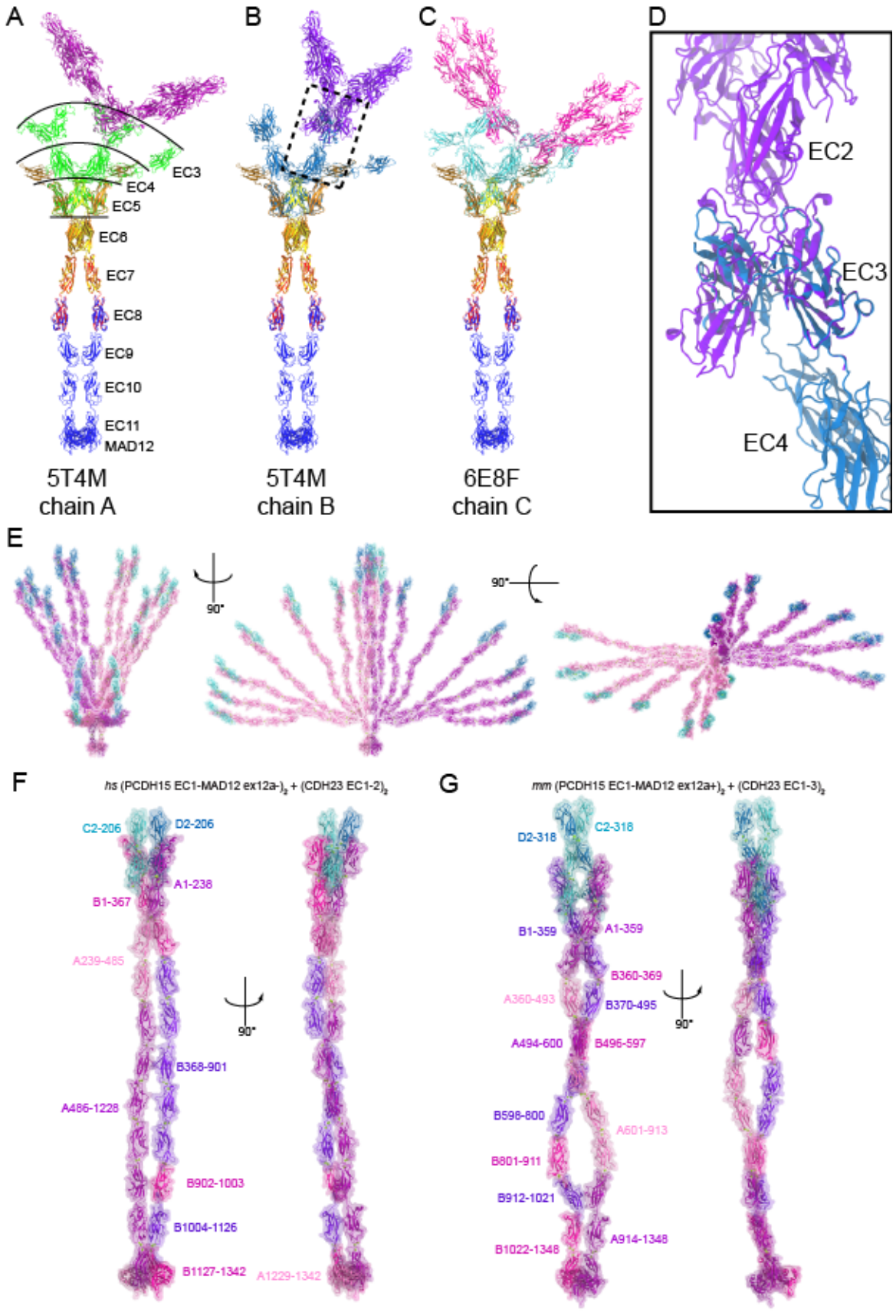
A
B
C
D
EC3
EC4
EC5
EC6
EC7
EC8
EC9
EC10
EC11
MAD12
5T4M
chain A
5T4M
chain B
6E8F
chain C
EC2
EC3
EC4
E
90°
90°
F
hs (PCDH15 EC1-MAD12 ex12a-)2 + (CDH23 EC1-2)2
C2-206
D2-206
A1-238
B1-367
A239-485
B368-901
A486-1228
B902-1003
B1004-1126
B1127-1342
A1229-1342
90°
G
mm (PCDH15 EC1-MAD12 ex12a+)2 + (CDH23 EC1-3)2
D2-318
C2-318
B1-359
A1-359
B360-369
A360-493
B370-495
A494-600
B496-597
B598-800
A601-913
B801-911
B912-1021
B1022-1348
A914-1348
90°

Fig. S14. Assembly of PCDH15 parallel dimers. (*A*) Use of crystallographic and cryo-EM structures to assemble the PCDH15 parallel dimer. The homodimeric cryo-EM structure of *mm* PCDH15 EC8-MAD12 (blue; PDB: 6C13) (47) and the crystal structure of *mm* PCDH15 EC7-8 V875A (red) were superimposed using EC8. Chain A (orange) and chain B (yellow) of *mm* PCDH15 EC5-7 I582T and *mm* PCDH15 EC4-7 (brown) were superimposed using EC7 of *mm* PCDH15 EC7-8 V875A. Chain A of *hs* PCDH15 EC3-5 ex12a- (green; PDB: 5T4M) (4) was overlapped with EC4 or EC5. The *hs* PCDH15 EC1-3 G16D/N369D/Q370N + *mm* CDH23 EC1-2 T15E structure (purple) was overlapped using EC3 (only two shown for clarity). The PCDH15 EC1-MAD12 parallel dimer constructed solely from the crystal and cryo-EM structures mentioned above was not compatible with the EC2-3-mediated X-dimer. (*B*) Similar to panel *C* but using chain B of *hs* PCDH15 EC3-5 ex12a- (blue; PDB: 5T4M) (4). The overlap of EC3 of *hs* PCDH15 EC1-3 G16D/N369D/Q370N + *mm* CDH23 EC1-2 T15E (purple) came close to an X-dimer conformation. (*C*) Similar to panel *C* but using chain C of *hs* PCDH15 EC3-5 ex12a+ (cyan). The overlap of EC3 of *hs* PCDH15 EC1-3 G16D/N369D/Q370N + *mm* CDH23 EC1-2 T15E (purple) was not compatible with an X-dimer conformation. (*D*) Detail from panel *B* showing the closest the structures come to creating the PCDH15 X-dimer mediated by EC2-3. The overlap of EC3 of *hs* PCDH15 EC3-5 ex12a- chain B (blue: 5T4M) and of *hs* PCDH15 EC1-3 G16D/N369D/Q370N + *mm* CDH23 EC1-2 T15E (purple) is on the right side. The other EC3 (left side) of *hs* PCDH15 EC1-3 G16D/N369D/Q370N + *mm* CDH23 EC1-2 T15E did not align well to the closest available EC3 from a PCDH15 EC3-5 structure. (*E*) Multiple views of the *hs* PCDH15 EC1-MAD12 ex12a- + CDH23 EC1-2 system during stretching simulation S1d (0.1 nm/ns, *SI Appendix*, Table S10, 0 – 70 ns) overlapped on the crystal structure of *mm* PCDH15 EC9-MAD12. Snapshots were taken every 10 ns (one at 35 ns). None of the depicted states is compatible with the EC2-3 X-dimer. (*F*) Details of the structures and simulation trajectory coordinates used to assemble the human (PCDH15 EC1-11+MAD12 ex12a-)$_2$ and (CDH23 EC1-2)$_2$ heterotetramer. Residue ranges for pieces of PCDH15 (A,B) and CDH23 (C,D) chains from different structures and simulation snapshots are labeled (see *SI Appendix,* Methods). (*G*) Details of the structures and simulation trajectory coordinates used to assemble the mouse (PCDH15 EC1-11+MAD12 ex12a+)$_2$ and (CDH23 EC1-3)$_2$ heterotetramer. Residue ranges for pieces of PCDH15 (A,B) and CDH23 (C,D) chains from different structures and simulation snapshots are labeled (see *SI Appendix,* Methods).

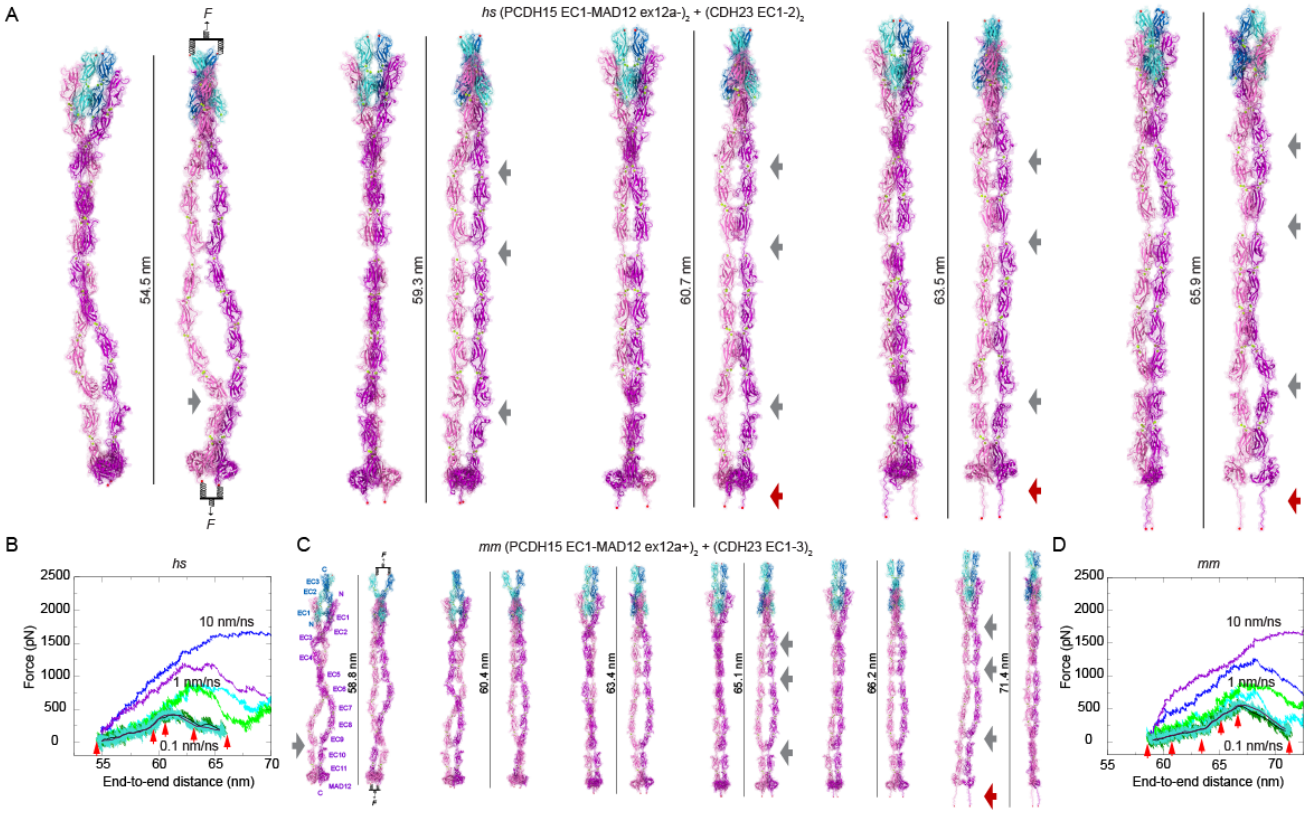

Fig. S15. Mechanics of PCDH15 ectodomains as part of an heterotetrameric complex with CDH23. (*A*) Snapshots of the heterotetrameric *hs* (PCDH15 EC1-MAD12 ex12a-)$_2$ + (CDH23 EC1-2)$_2$ system during stretching simulation S8d (0.1 nm/ns). Stretched C-terminal Cα atoms are shown as red spheres. Stretching was carried out by attaching two slabs to springs that were in turn attached to the terminal ends of each protein monomer. Slabs were moved in opposite directions at constant speed through individual springs. Gray arrows highlight location of flexible PCDH15 EC linkers (EC9-10, EC5-6, and EC3-4). Dark red arrow indicates unfolding of PCDH15 MAD12's C-terminal end. (*B*) Force applied to slabs versus protein separation (see *SI Appendix,* Methods and Table S10) for constant velocity stretching simulations of the *hs* (PCDH15 EC1-MAD12 ex12a-)$_2$ + (CDH23 EC1-2)$_2$ system at 10 nm/ns (S8b, purple and blue), 1 nm/ns (S8c, bright green and cyan), and 0.1 nm/ns (S8d, dark green and turquoise with 10-ns running averages in black and maroon). Red arrowheads indicate time-points for simulation S8d illustrated in *A*. (*C*) Snapshots of the heterotetrameric *mm* (PCDH15 EC1-MAD12 ex12a+)$_2$ + (CDH23 EC1-3)$_2$ system during stretching simulation S9d (0.1 nm/ns). Shown as in *A*. (*D*) Force applied to slabs versus protein separation (also shown in Fig. 6*C*; see *SI Appendix,* Methods and Table S10) for constant velocity stretching simulations of the *mm* (PCDH15 EC1-MAD12 ex12a+)$_2$ + (CDH23 EC1-3)$_2$ system at 10 nm/ns (S9b, purple and blue), 1 nm/ns (S9c, bright green and cyan), and 0.1 nm/ns (S9d, dark green and turquoise with 10-ns running averages in black and maroon). Red arrowheads indicate time-points for simulation S9d illustrated in *C*.

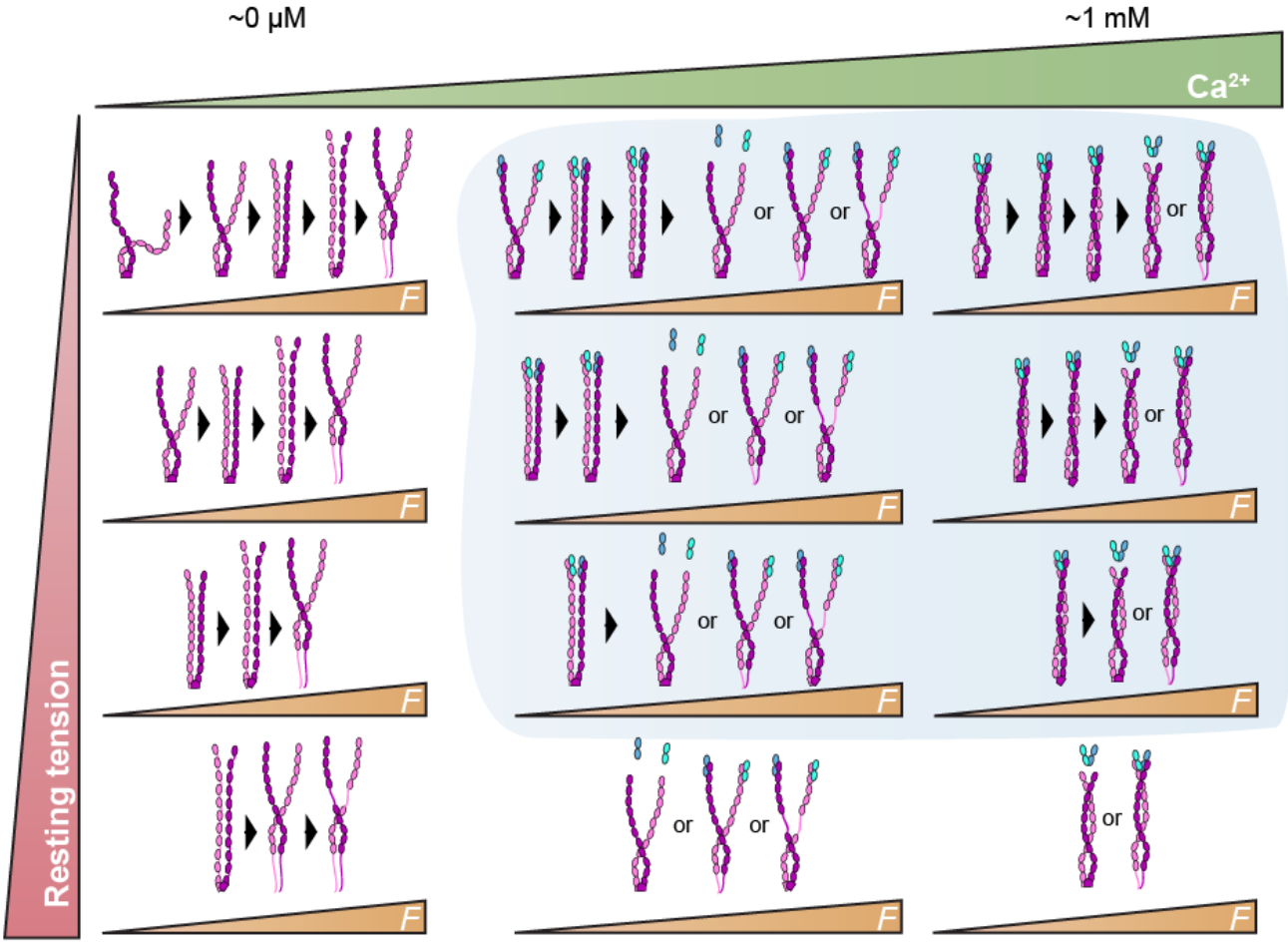

Fig. S16. Elastic response of PCDH15 in the presence of resting tension. Tip links experience a constant resting tension that varies along the cochlea from ~5 to 50 pN (90). This resting tension will pre-stretch the PCDH15 ectodomain, thus conditioning its elastic response to an external stimulus (*F* in the figure).

TABLE S1 STATISTICS FOR STRUCTURES

Data collection	***mm* PCDH15 EC1-2 BAP**	***hs* PCDH15 EC1-3 G16D/N369D/ Q370N**	***hs* PCDH15 EC1-3 G16D /N369D/Q370N + *mm* CDH23 EC1-2 T15E[#]**	***hs* PCDH15 EC2-3**
Space group	$P6_4$	$C222_1$	$P2_1$	$P2_1$
Unit cell parameters				
a, *b*, *c* (Å)	99.62, 99.62, 58.56	87.89, 116.52, 99.89	76.79, 65.40, 190.02	65.76, 147.63, 77.03
α, β, γ (°)	90.0, 90.0, 120.0	90.0, 90.0, 90.0	90.0, 99.1, 90.0	90.0, 101.2, 90.0
Molecules per asymmetric unit	1	1	2 × 2	4
Beam source	APS-24-ID-C	APS-24-ID-C	APS-24-ID-E	APS-24-ID-C
Date of data collection	21-MAR-2015	07-NOV-2017	18-OCT-2018	21-MAR-2015
Wavelength (Å)	0.9792	0.9792	0.9792	0.9792
Resolution limit (Å)	2.40	3.15	2.90	2.64
Unique reflections	13,043	9,312	41,847	42,598
Completeness (%)	100.0 (100.0)	99.4 (99.8)	93.2 (86.5)	96.4 (95.0)
Redundancy	8.8 (7.4)	9.0 (5.2)	5.2 (4.4)	2.6 (2.4)
$I / \sigma(I)$	17.83 (3.00)	6.81 (2.21)	12.33 (2.60)	10.63 (1.70)
R_{merge}	0.13 (0.80)	0.36 (1.38)	0.12 (0.47)	0.10 (0.58)
R_{meas}	0.14 (0.86)	0.38 (1.53)	0.13 (0.53)	0.12 (0.73)
R_{pim}	0.05 (0.31)	0.12 (0.62)	0.06 (0.24)	0.07 (0.44)
$CC_{1/2}$	0.97 (0.90)	0.95 (0.34)	0.98 (0.94)	0.90 (0.65)
*CC**	0.99 (0.97)	0.99 (0.71)	0.99 (0.99)	0.97 (0.89)
Refinement				
Resolution range (Å)	49.86 – 2.40 (2.47 – 2.40)	49.99 – 3.15 (3.20 – 3.15)	49.52 – 2.90 (2.97 – 2.90)	50.00 – 2.64 (2.70 – 2.64)
R_{work} (%)	17.0 (23.0)	21.5 (27.9)	22.5 (29.9)	21.5 (33.6)
R_{free} (%)	23.3 (29.8)	28.8 (36.3)	25.3 (32.4)	24.6 (31.5)
Residues (atoms)	231 (1,842)	333 (2,629)	1099 (8,699)	893 (7,135)
Water molecules	49	5	62	131
Rms deviations				
Bond lengths (Å)	0.011	0.009	0.012	0.015
Bond angles (°)	1.706	1.361	1.639	1.689
B-factor average				
Protein	47.27	77.93	82.54	56.69
Ligand/ion	38.38	57.79	81.57	39.89
Water	42.48	46.60	50.95	37.60
Ramachandran Plot Region (PROCHECK)				
Most favored (%)	89.1	82.4	88.9	90.4
Additionally allowed (%)	10.4	17.2	10.9	9.4
Generously allowed (%)	0.5	0.4	0.2	0.1
Disallowed (%)	0.0	0.0	0.0	0.0
PDB ID	**6N22**	**6MFO**	**6N2E**	**5ULY**

[#] Amplitude-based twin refinement.

TABLE S1 STATISTICS FOR STRUCTURES (continued)

Data collection	***hs* PCDH15 EC2-3 V250N**	***hs* PCDH15 EC3-5 ex12a+[#]**	***mm* PCDH15 EC4-7**	***mm* PCDH15 EC5-7 I582T**
Space group	$P2_1$	$P222_1$	$P4_32_12$	$P4_222$
Unit cell parameters				
a, *b*, *c* (Å)	77.18, 31.95, 115.96	95.74, 95.91, 258.60	78.86, 78.86, 289.47	180.91, 180.91, 127.16
α, β, γ (°)	90.0, 106.4, 90.0	90.0, 90.0, 90.0	90.0, 90.0, 90.0	90.0, 90.0, 90.0
Molecules per asymmetric unit	2	3	1	2
Beam source	APS-24-ID-E	APS-24-ID-C	APS-24-ID-C	APS-24-ID-E
Date of data collection	13-FEB-2018	29-MAR-2018	10-JUL-2015	19-DEC-2016
Wavelength (Å)	0.9792	0.9792	0.9792	0.9792
Resolution limit (Å)	2.60	2.99	3.35	3.79
Unique reflections	17,491	48,387	14,064	21,629
Completeness (%)	95.0 (89.2)	99.9 (99.1)	98.5 (86.4)	97.6 (87.8)
Redundancy	4.2 (2.8)	10.2 (7.9)	11.2 (7.2)	6.4 (4.7)
$I / \sigma(I)$	7.3 (2.9)	9.3 (2.4)	16.9 (2.5)	7.43 (0.55)
R_{merge}	0.19 (0.33)	0.21 (0.81)	0.13 (0.60)	0.23 (2.43)
R_{meas}	0.22 (0.39)	0.22 (0.87)	0.14 (0.64)	0.25 (2.69)
R_{pim}	0.10 (0.20)	0.07 (0.30)	0.04 (0.21)	0.10 (1.12)
$CC_{1/2}$	0.87 (0.90)	0.94 (0.78)	0.99 (0.91)	0.77 (0.27)
*CC**	0.96 (0.972	0.99 (0.94)	0.99 (0.98)	0.91 (0.65)
Refinement				
Resolution range (Å)	39.47 – 2.60 (2.65 – 2.58)	47.95 – 2.99 (3.07 – 2.99)	76.09 – 3.35 (3.44 – 3.35)	180.90 – 3.79 (3.88 – 3.79)
R_{work} (%)	23.2 (31.7)	17.4 (23.4)	22.7 (39.2)	24.0 (37.9)
R_{free} (%)	27.0 (35.1)	21.4 (27.9)	27.9 (44.0)	28.3 (42.8)
Residues (atoms)	457 (3,626)	1021 (7,966)	405 (3,118)	623 (4,756)
Water molecules	40	8	1	-
Rms deviations				
Bond lengths (Å)	0.007	0.007	0.011	0.009
Bond angles (°)	1.198	1.249	1.620	1.486
B-factor average				
Protein	43.08	89.12	124.15	154.78
Ligand/ion	41.04	85.04	107.63	111.88
Water	28.69	58.58	91.23	-
Ramachandran Plot Region (PROCHECK)				
Most favored (%)	90.6	88.1	84.6	86.2
Additionally allowed (%)	8.9	11.7	15.1	13.8
Generously allowed (%)	0.5	0.2	0.3	0.0
Disallowed (%)	0.0	0.0	0.0	0.0
PDB ID	**6EB5**	**6E8F**	**5W1D**	**6BXU**

[#] Amplitude-based twin refinement.

TABLE S1 STATISTICS FOR STRUCTURES (continued)

Data collection	***mm* PCDH15 EC6-7**	***mm* PCDH15 EC7-8 V875A**	***mm* PCDH15 EC9-MAD12**
Space group	$P6_222$	C2	$C222_1$
Unit cell parameters			
a, *b*, *c* (Å)	110.98, 110.98, 206.02	135.80, 22.99, 70.74	129.51, 170.06, 91.53
α, β, γ (°)	90.0, 90.0, 120.0	90.0, 97.3, 90.0	90.0, 90.0, 90.0
Molecules per asymmetric unit	1	1	1
Beam source	APS-24-IDE-E	APS-24-ID-C	APS-24-ID-E
Date of data collection	15-JUN-2017	22-MAR-2015	02-JUL-2018
Wavelength (Å)	0.9792	0.9792	0.9792
Resolution limit (Å)	2.94	2.00	3.23
Unique reflections	16,643	15,280	16,630
Completeness (%)	98.1 (96.9)	96.5 (82.1)	99.5 (94.8)
Redundancy	7.7 (5.2)	3.1 (2.4)	9.8 (4.7)
$I / \sigma(I)$	10.92 (2.00)	23.1 (5.4)	14.5 (2.2)
R_{merge}	0.13 (0.81)	0.05 (0.14)	0.17 (0.81)
R_{meas}	0.14 (0.89)	0.05 (0.18)	0.18 (0.89)
R_{pim}	0.05 (0.37)	0.03 (0.10)	0.05 (0.36)
$CC_{1/2}$	0.98 (0.89)	0.99 (0.97)	1.01 (0.78)
*CC**	0.99 (0.97)	0.99 (0.99)	1.00 (0.94)
Refinement			
Resolution range (Å)	96.11 – 2.94 (3.02 – 2.94)	70.17 – 2.00 (2.05 – 2.00)	45.81 – 3.23 (3.31 – 3.23)
R_{work} (%)	21.7 (40.3)	19.0 (21.1)	17.6 (27.8)
R_{free} (%)	24.2 (42.4)	22.9 (27.5)	23.4 (47.0)
Residues (atoms)	206 (1,594)	202 (1,586)	443 (3,476)
Water molecules	5	121	0
Rms deviations			
Bond lengths (Å)	0.008	0.008	0.008
Bond angles (°)	1.321	1.315	1.397
B-factor average			
Protein	107.22	40.86	97.32
Ligand/ion	82.53	44.45	127.92
Water	74.82	41.45	-
Ramachandran Plot Region (PROCHECK)			
Most favored (%)	87.2	93.8	86.8
Additionally allowed (%)	12.2	5.7	13.0
Generously allowed (%)	0.6	0.6	0.3
Disallowed (%)	0.0	0.0	0.0
PDB ID	**6BWN**	**5TPK**	**6EET**

TABLE S2 List of species and PCDH15 accession numbers used in multiple sequence alignment analysis

Species	Abbreviation	NCBI Accession number
Homo sapiens CD1-1	*Hs1*	NP_001136235.1
Homo sapiens CD2-1	*Hs2*	NP_001136241.1
Tursiops truncatus	*Tt*	XP_019792025.1
Sus scrofa	*Ss*	XP_020929194.1
Canis lupus familiaris	*Clf*	XP_022266127.1
Mus musculus	*Mm*	NP_075604.2
Desmodus rotundus	*Dr2*	XP_024416857.1
Gallus gallus	*Gg*	XP_015143564.1
Columba livia	*Cl*	XP_021147002.1
Lonchura striata domestica	*Lsd*	XP_021391314.1
Corvus brachyrhynchos	*Cb*	XP_017589248.1
Pogona vitticeps	*Pv*	XP_020662251.1
Anolis carolinensis	*Ac*	XP_016851436.1
Crocodylus porosus	*Cp*	XP_019394135.1
Danio rerio	*Dr*	NP_001012500.1
Clupea harengus	*Ch*	XP_012675462.1
Astyanax mexicanus	*Am*	XP_022525074.1
Callorhinchus milii	*Cm*	XP_007897895.1

TABLE S3 Expression, refolding, and purification conditions for bacterially expressed protein fragments

Fragment	Cells	Media	*T* °C	IPTG μM	Refolding	SEC
mm PCDH15 EC1-2BAP	RIPL	TB	30	200	RS1	SB1 pH 7.5
hs PCDH15 EC1-3 G16D/N369D/Q370N	RIPL	TB	30	200	RS1	SB1 pH 8.0
hs PCDH15 EC1-4 ex12a- WT and L306N/V307N	RIPL	TB	30	200	RS2	SB1 pH 8.0
hs PCDH15 EC1-3 WT and L306N/V307N	RIPL	TB	30	200	RS2	SB1 pH 8.0
mm CDH23 EC1-2 T15E	RIPL	LB	30	200	R1	SB1 pH 8.0
hs PCDH15 EC2-3 WT & mutants	RIPL	LB	30	200	R1	SB1 pH 8.0
hs PCDH15 EC3-5 ex12a+	RIPL	LB	30	200	R2	SB2
mm PCDH15 EC4-7	BL21	TB	30	1000	R3	SB3
mm PCDH15 EC5-7 I582T	RIPL	TB	30	1000	R4	SB4
mm PCDH15 EC6-7	Rosetta	TB	30	1000	R5	SB3
mm PCDH15 EC7-8 V875A	RIPL	LB	37	1000	R6	SB4
mm PCDH15 EC9-MAD12	Rosetta	LB	30	1000	R7	SB5

RIPL – *E. coli* BL21 CodonPlus(DE3)-RIPL cells.
BL21 – *E. coli* BL21 cells.
Rosetta – *E. coli* BL21 Rosetta(DE3) cells.

RS1 – Five-step dialysis. Two 24-h dialysis steps against D buffer (20 mM Tris HCl, pH 8.0, 10 mM $CaCl_2$) plus 3 M and 2 M GuHCl, respectively. Last three steps consisted of 12-h dialyses against D buffer with decreasing GuHCl concentration (1, 0.5, and 0 M) plus 400 mM L-Arg and 375 μM GSSG.
RS2 – Five-step dialysis. Two 24-h dialysis steps against D buffer (20 mM Tris HCl, pH 8.0, 10 mM $CaCl_2$) plus 3 M and 2 M GuHCl, respectively. Last three steps consisted of 12-h dialyses against D buffer with decreasing GuHCl concentration (1, 0.5, and 0 M) plus 400 mM L-Arg and 375 μM GSSG. The dialysis buffer having 0 M GuHCl was supplemented with 1 mM GSSG.
R1 – Overnight dialysis in 20 mM Tris HCl, pH 8.0, 150 mM KCl, 50 mM NaCl, 2 mM $CaCl_2$, and 400 mM L-Arg (+10% glycerol for *hs* PCDH15 EC2-3 mutants).
R2 – Overnight dialysis in 20 mM Tris HCl, pH 8.0, 10 mM $CaCl_2$, 400 mM L-Arg, and 1 mM GSSG.
R3 – Overnight dialysis in 20 mM Tris HCl, pH 8.0, 150 mM KCl, 5 mM $CaCl_2$, 400 mM L-Arg, and 2 mM DTT.
R4 – Overnight dialysis in 20 mM Tris HCl, pH 8.0, 150 mM KCl, 50 mM NaCl, 2 mM $CaCl_2$, 400 mM L-Arg, and 2 mM DTT.
R5 – Overnight dialysis in 20 mM Tris HCl, pH 5.2, 150 mM KCl, 50 mM NaCl, 2 mM $CaCl_2$,400 mM L-Arg, and 2 mM DTT.
R6 – Overnight dialysis in 20 mM Tris HCl, pH 8.0, 150 mM KCl, 5 mM $CaCl_2$, and 10% glycerol.
R7 – Drop-by-drop dilution (5) in 20 mM Tris HCl, pH 8.0, 150 mM KCl, 5 mM $CaCl_2$, 400 mM L-Arg, 1 mM TCEP-HCl and 10% glycerol.

SB1 pH 7.5 – 20 mM Tris HCl, pH 7.5, 150 mM KCl, 50 mM NaCl, and 2 mM $CaCl_2$.
SB1 pH 8.0 – 20 mM Tris HCl, pH 8.0, 150 mM KCl, 50 mM NaCl, and 2 mM $CaCl_2$.
SB2 – 20 mM Tris HCl, pH 8.0, 150 mM KCl, 50 mM NaCl, and 5 mM $CaCl_2$ (double purified).
SB3 – 20 mM Tris HCl, pH 8.0, 150 mM NaCl, 50 mM KCl, and 2 mM $CaCl_2$.
SB4 – 20 mM Tris HCl, pH 8.0, 150 mM KCl, and 5 mM $CaCl_2$.
SB5 – 20 mM Tris HCl, pH 8.0, 150 mM KCl, and 5 mM $CaCl_2$, 1 mM TCEP.

TABLE S4 X-ray crystallography experiments (conditions for crystal growth and cryo protection)

Construct	Crystallization conditions	Cryo	P + B (μl)
mm PCDH15 EC1-2BAP	0.02 M $CaCl_2$, 0.1 M Sodium Acetate, 30% MPD		0.6 + 0.6
hs PCDH15 EC1-3 G16D/N369D/Q370N	0.1 M HEPES pH 7.7, 66% MPD, 4% Glycerol		1.0 + 0.5
hs PCDH15 EC1-3 G16D/N369D/Q370N + *mm* CDH23 EC1-2 T15E	0.1 M Imidazole pH 6.8, 46% MPD		0.6 + 0.6
hs PCDH15 EC2-3	0.1 M HEPES pH 7.5, 0.1 M KCl, 15% PEG 6000		0.6 + 0.6
hs PCDH15 EC2-3 V250N	0.1 M MES pH 5.9, 0.15 M $MgCl_2$, 32% PEG 400		0.6 + 0.6
hs PCDH15 EC3-5 ex12a+	40% MPD, 0.2 M Lithium Chloride, 0.01 M ATP Disodium		0.6 + 0.6
mm PCDH15 EC4-7	0.1 M Tris HCl, pH 8.5, 2.0 M Magnesium Acetate	23% PEG 400	0.6 + 0.6
mm PCDH15 EC5-7 I582T	0.2 M Sodium Formate, 40% MPD		0.6 + 0.6
mm PCDH15 EC6-7	30% PEG 1500	10% PEG 400	0.6 + 0.6
mm PCDH15 EC7-8 V875A	10% Ammonium Chloride, 10% PEG3350	25% Glycerol	1.0 + 0.5
mm PCDH15 EC9-MAD12	0.1 M HEPES Sodium Salt, 30% MPD, 5% PEG 4000		0.6 + 0.6

TABLE S5 OLIGOMERIZATION STATE OF PCDH15 FRAGMENTS

System	Predicted Mass Monomer / Dimer kDa	SEC-MALS kDa†	SEC-SAXS kDa†	State
hs PCDH15 EC2-3 WT (*n* = 3)	29.3 / 58.7	57.2 (2.6%)	--	Dimer
hs PCDH15 EC2-3 V250N (*n* = 3)	29.3 / 58.7	32.4 (10.6%)	--	Monomer
hs PCDH15 EC2-3 L306N/V307N (*n* = 3)	29.3 / 58.7	32.7 (11.6%)	--	Monomer
hs PCDH15 EC2-3 V250/L306N/V307N (*n* = 2)	29.3 / 58.7	30.1 (2.7%)	--	Monomer
hs PCDH15 EC1-3 WT (*n* = 1)	43.0 / 86.0	84.3 (2.0%)	--	Dimer
hs PCDH15 EC1-3 L306N/V307N (*n* = 1)	43.0 / 86.0	46.4 (7.9%)	--	Monomer
hs PCDH15 EC1-4 ex12a- WT (*n* = 1)	55.7 / 111.5	106.7 (4.3%)	--	Dimer
hs PCDH15 EC1-4 ex12a- L306N/V307N (*n* = 1)	55.8 / 111.5	57.9 (3.8%)	--	Monomer
mm PCDH15 EC9-MAD12 (*n* = 1)	52.0 / 103.7	--	98.1 (5.6%)	Dimer
*mm** PCDH15 EC1-3 WT (*n* = 1)	43.7 / 87.4	105.4 (20.6%)	--	Dimer
*mm** PCDH15 EC1-4 ex12a- WT (*n* = 2)	56.7 / 113.3	139.6 (21.9%)	--	Dimer
*mm** PCDH15 EC1-4 ex12a- V250N (*n* = 2)	56.7 / 113.3	72.6 (26.7%)	--	Monomer
*mm** PCDH15 EC9-MAD12 WT (*n* = 1)	52.9 / 105.7	111.9 (5.9%)	--	Dimer
*mm** PCDH15 EC1-MAD12 WT (*n* = 2)	152.4 / 304.8	377.1 (23.2%)	--	Dimer
*mm** PCDH15 EC1-MAD12 WT EDTA¶ (*n* = 2)	152.4 / 304.8	355.8 (16.3%)	--	Dimer

† Values in parenthesis indicate percentage deviation from predicted molecular mass.

* Mammalian expressed protein. The predicted mass represents that of the protein sequence without glycosylation. The calculated mass from SEC-MALS experiments is higher due to the presence of sugar moieties on the protein.

¶ EDTA was present in the SEC column but not directly added to the sample.

TABLE S6 Interface areas of PCDH15-CDH23 "handshakes" from various structures as computed by PISA.

PDB	**Chains**	**Area (Å^2)**
4APX	A/B	907.0
4AQ8	B/D	1160.2
4AQ8	A/C	1070.2
4AQA	A/B	958.4
4AQE	A/B	894.6
4XXW	A/D	1143.7
4XXW	B/C	1061.0
6N2E	A/D	1154.8
6N2E	B/C	1209.6

TABLE S7 SAXS data collection and scattering-derived parameters.

Data collection parameters	***mm* PCDH15 EC9-MAD12**
Instrument	SIBYLS beamline
Beam geometry	Point Focus
Wavelength (Å)	1.03
q range (Å^{-1})	0.009198 – 0.5925
Exposure time (min)	40
Frame slicing (s)	3
Concentration (mg/mL)	4.2
Temperature (K)	293.15
Structural parameters	
R_g (Å) [from P(r)]	47.3 ± 0.2
R_g (Å) [from Guinier]	46.7 ± 2.9
R_g (Å) [from 6EET]*	42.01
D_{max} (Å) [from GNOM]	160
Molecular mass determination	
Molecular mass**	98.12
Calculated mass from sequence (monomer)	51.98
Discrepancy (%)	5.62
Oligomeric state	Dimer
Software employed	
Primary data reduction	Beamline software
Data processing	PRIMUS, GNOM, SREFLEX
Computation of model intensities	FoXS

* Estimated using VMD (25).

** Molecular mass estimated using the SAXS MoW2 server with the method described in (18).

TABLE S8 Structures used to build *hs* PCDH15 EC1-MAD12 ex12a- + *hs* CDH23 EC1-2 and *mm* PCDH15 EC1-MAD12 ex12a+ + *mm* CDH23 EC1-3 models.

***hs* PCDH15 EC1-MAD12 ex12a- model**			
EC	**PDB ID (chain)**	**Residues**	**Mutations**
EC1-2	4APX (B)	1-136, 138-200, 203-233	L66M, V100I, V107I, E175D, V193I, Y208F
EC2-3	5ULY (D)	137, 201-202, 234-365	-
EC3-5	5T4M (A)	366-584	-
EC4-7	5W1D (A)	585-694, 722-727	E395D, T401S, P435Q, L459S, V473I, R477Q, S502R, S524T, G531A, K532Q, V536I, V544I, S545T, L552M, Q556R, S565A, H575N, V604I, I610V, I613V, P626S, S650T, V667I, R719K, A760V, H763Y, Y785A
EC7-8	5TPK (A)	695-721, 728-805, 820-834, 873-894	R719K, A760V, H763Y, Y785A, V806L, S816T, F817I, L843F, A875V
EC8-10	4XHZ (A)	806-819, 835-872, 895-1025, 1027-1076, 1078-1113	-
EC10-MAD12	6BXZ (C)	1026, 1077, 1114-1342	A1029T, L1036V, K1058T, A1072G, D1118N, A1140T, A1157V, V1300I
***hs* CDH23 EC1-2 model**			
EC1-2	4APX (A)	1-205	R35Q, P153Q, Q168R, V174T
mm* PCDH15 EC1-MAD12 ex12a+ model			
EC1-3	6N2E (B)	5-265, 270-364	D16G, M66L, I100V, I107V, D175E, I193V, F208Y, I278L, S327T, G359S
EC3-5	6E8F (B)	266-269, 365-585(+7)	D395E, S401T, S411G(+7), Q435P(+7), S459L(+7), I473V(+7), Q477R(+7), R502S(+7), T524S(+7), A531G(+7), Q532K(+7), I536V(+7), I544V(+7), T545S(+7), M550L(+7), R556Q(+7), A565S(+7), N575H(+7), I582T(+7)
EC4-7	5W1D (A)	585-695(+7), 721-741(+7), 764-783(+7)	-
EC7-8	5TPK (A)	703-727(+7), 749-772(+7), 791-809(+7), 823-837(+7), 879-897(+7)	-
EC8-10	4XHZ (A)	810-822(+7), 838-878(+7), 898-909(+7), 936-949(+7), 995-1002(+7)	L813V(+7), F850L(+7), L944M(+7)
EC9-MAD12	6EET (A)	910-935(+7), 950-994(+7), 1003-1348(+7)	-
mm* CDH23 EC1-3 model*			
EC1-2	6N2E (C)	3-116, 125-164, 182-199	E16T, S128P
EC1-3	5W4T (A)	114-121(+3), 162-178(+3), 197-315(+3)	I114V(+3), Q115R(+3), A167E(+3), T172V(+3), I174Q(+3), T200I(+3), I204M(+3), T212I(+3), M221Y(+3), D223H(+3), A224S(+3), Y228T(+3), E229T(+3), K232V(+3), R234T(+3), I236V(+3), L240K(+3), I251V(+3), M258I(+3), S267A(+3), V270L(+3), S271N(+3), Q273L(+3), S283H(+3), I287L(+3), A291G(+3), S302D(+3), T310N(+3), L313V(+3)

* Residue numbering after exon 12a insertion is indicated with (+7).

** Residue numbering of the fish protein is shifted by 3 residues indicated with (+3).

TABLE S9 List of deafness-causing missense mutation sites and in-frame deletions on PCDH15.

Citation	Mutation in *hs*	EC number	Note[a]	Diagnosis
Miyagawa et al., 2013	G79R	EC1	o	Non-syndromic
Geng et al., 2013	I108N	EC1	h	USH1F
Ahmed et al., 2003	R113G	EC1	h	DFNB23
Aller et al., 2010	R113Q	EC1	h	Likely USH1F
Ahmed et al., 2008	D157G	EC2	**D**xD	USH1F
Ahmed et al., 2003	G241D	EC3	i	DFNB23
Miyagawa et al., 2013	R257H	EC3	o	Non-syndromic
Abdi et al., 2016	E272_Q509del	EC3-5	deletion	USH1F
Miyagawa et al., 2013	P294L	EC3	o	Non-syndromic
Yang et al., 2013	L408P	EC4	o	Non-syndromic
Grossman et al., 2010	D414A	EC4	o	Non-syndromic
Doucette et al., 2009	V507D	EC5	i	DFNB23
Zhan et al., 2015	V767del	EC7	deletion	DFNB23
Alagramam et al., 2011	G936_K982del	EC9	deletion	USH1F
Miyagawa et al., 2013	R941C	EC9	o	Non-syndromic
Chen et al., 2015	D989G	EC9	x**D**x	DFNB23
Schrauwen et al., 2018	R1013H	EC10	o	DFNB23
Miyagawa et al., 2013	G1130R	EC11	i	Non-syndromic
Yang et al., 2013	S1267P	EC12	o	Non-syndromic

[a] Notes indicate inward facing residues (i), outward facing residues (o), handshake interface localization (h), and conserved calcium-binding motifs affected.

TABLE S10 Summary of simulations.

Label	System[a]	t_{sim} (ns)	Type	Start	Speed (nm/ns)	Average Peak Force (pN)[c]	Size (#atoms)	Initial Size (nm^3)
S1a	*hs*	11.1	EQ[b]	–	–	–	924,024	71.2 × 9.2 × 14.9
S1b	heterodimer	1.2	SMD[d]	S1a	10	811.6		
S1c		11.2	SMD[d]	S1a	1	447.2		
S1d		191.9	SMD[d]	S1a	0.1	331.2		
S2a	*mm*	11.1	EQ[b]	–	–	–	1,016,888	91.7 × 11.1 × 10.5
S2b	heterodimer	3.3	SMD[d]	S2a	10	751.9		
S2c		30.2	SMD[d]	S2a	1	398.8		
S2d		251.6	SMD[d]	S2a	0.1	355.9		
S2e		3.5	SMD[e]	S2a	10	1023.6		
S2f		30.6	SMD[e]	S2a	1	522.1		
S3a	*hs* short	11.1	EQ[b]	–	–	–	833,064	40.5 × 17.3 × 12.4
S3b	tetramer	2.1	SMD[f]	S3a	10	2195.3		
S3c	3 Ca^{2+} /	12.3	SMD[f]	S3a	1	1288.8		
S3d	linker	95.6	SMD[f]	S3a	0.1	1082.5		
S4a	*hs* short	10.0	EQ[b]	–	–	–	833,037	40.5 × 17.3 × 12.4
S4b	tetramer	1.9	SMD[f]	S4a	10	1940.2		
S4c	2 Ca^{2+} /	13.7	SMD[f]	S4a	1	1175.8		
S4d	linker	99.5	SMD[f]	S4a	0.1	737.7		
S5a	*hs* short	10.0	EQ[b]	–	–	–	832,984	40.5 × 17.3 × 12.4
S5b	tetramer	2.3	SMD[f]	S5a	10	2084.7		
S5c	1 Ca^{2+} /	15.1	SMD[f]	S5a	1	1173.3		
S5d	linker	129.8	SMD[f]	S5a	0.1	833.4		
S6a	*hs* short	10.0	EQ[b]	–	–	–	832,924	40.5 × 17.3 × 12.4
S6b	tetramer	1.9	SMD[f]	S6a	10	1846.3		
S6c	0 Ca^{2+} /	14.5	SMD[f]	S6a	1	1067.2		
S6d	linker	142.9	SMD[f]	S6a	0.1	760.7		
S7a	*mm* short	11.1	EQ[b]	–	–	–	743,064	51.1 × 11.7 × 12.9
S7b	tetramer	3.3	SMD[f]	S7a	10	2064.9		
S7c	3 Ca^{2+} /	11.4	SMD[f]	S7a	1	1003.0		
S7d	linker	88.3	SMD[f]	S7a	0.1	804.5		
S7e		500.3	SMD[f]	S7a	0.02	732.6		
S8a	*hs* long	11.1	EQ[b]	–	–	–	1,178,985	99.4 × 11.4 × 10.9
S8b	tetramer	1.7	SMD[e]	S8a	10	1417.3		
S8c	3 Ca^{2+} /	18.1	SMD[e]	S8a	1	893.6		
S8d	linker	122.3	SMD[e]	S8a	0.1	510.4		
S9a	*mm* long	11.1	EQ[b]	–	–	–	1,292,017	91.5 × 11.8 × 12.5
S9b	tetramer	3.4	SMD[f]	S9a	10	1484.7		
S9c	3 Ca^{2+} /	20.6	SMD[f]	S9a	1	852.6		
S9d	linker	135.5	SMD[f]	S9a	0.1	630.3		
S9e		555.8	SMD[f]	S9a	0.02	519.8		
S9f		3.5	SMD[g]	S9a	10	2036.4		
S9g		22.9	SMD[g]	S9a	1	1275.5		
S10a		95.3	EQ[b]	–	–	–	2,325,962	65.5 × 18.9 × 19.5
S11a	*mm*	11.1	EQ[b]	–	–	–	456,282	27.9 × 12.9 × 12.9
S11b	PCDH15	3.0	SMD[f]	S11a	10	1418.5		
S11c	EC9-12	14.9	SMD[f]	S11a	1	882.8		
S11d	dimer	95.8	SMD[f]	S11a	0.1	604.2		
Total		2,858.9						

[a] S1 *hs* PCDH15 EC1-MAD12 + CDH23 EC1-2 + 3 Ca^{2+}/linker; S2 *mm* PCDH15 EC1-MAD12 + CDH23 EC1-3 + 3 Ca^{2+}/linker; S3 *hs* $(PCDH15\ EC1\text{-}5)_2$ + $(CDH23\ EC1\text{-}2)_2$ + 3 Ca^{2+}/linker; S4 *hs* $(PCDH15\ EC1\text{-}5)_2$ + $(CDH23\ EC1\text{-}2)_2$ + 2 Ca^{2}/linker; S5 *hs* $(PCDH15\ EC1\text{-}5)_2$ + $(CDH23\ EC1\text{-}2)_2$ + 1 Ca^{2}/linker; S6 *hs* $(PCDH15\ EC1\text{-}5)_2$ + $(CDH23\ EC1\text{-}2)_2$ + 0 Ca^{2}/linker; S7 *mm* $(PCDH15\ EC1\text{-}5)_2$ + $(CDH23\ EC1\text{-}3)_2$ + 3 Ca^{2+}/linker; S8 *hs* $(PCDH15\ EC1\text{-}MAD12)_2$ + $(CDH23\ EC1\text{-}2)_2$ + 3 Ca^{2+}/linker; S9 and S10 *mm* $(PCDH15\ EC1\text{-}MAD12)_2$ + $(CDH23\ EC1\text{-}3)_2$ + 3 Ca^{2+}/linker; S11 *mm* $(PCDH15\ EC9\text{-}MAD12)_2$ + 3 Ca^{2+}/linker.

[b] EQ indicates simulations that consisted of 1,000 steps of minimization, 100 ps of dynamics with the protein backbone constrained (k = 1 kcal mol^{-1} Å^{-2}), 1 ns of free dynamics in the *NpT* ensemble (γ = 1 ps^{-1}), and 10 ns of free dynamics in the *NpT* ensemble (γ = 0.1 ps^{-1}).
[c] Average peak force is calculated from the peak force measured on stretched Cα atoms or slabs (using 50-ps running averages).
[d] SMD simulation in which terminal Cα atoms were attached to independent stretching springs.
[e] SMD simulation in which the terminal Cα atom of CDH23 EC3 and the COM of PCDH15 MAD12 Cα atoms were attached to independent stretching springs.
[f] SMD simulation in which force was applied through slabs to protein ends (see *SI Appendix*, Methods).
[g] SMD simulation in which force was applied through slabs to the terminal Cα atom of CDH23 EC3 and the COM of PCDH15 MAD12 Cα atoms (see *SI Appendix,* Methods).

Table S11 Structural comparison among cadherins expressed and purified using different methods (native *vs*. refolded)

Protein	Species	Native (N) / Refolded (R)	Glycosylation (Y/N)	Resolution (Å)	PDB	RMSD (Å)										
						2WHV	3MVS	6MFO	6N2E (A)	6CV7	6BXZ (A)	6C10	6EET	6BX7	6MGA	6VFP
CDH23																
EC1-2	*Hs*	R	N	2.36	2WHV	0.0	2.4									
EC1-2	*Hs*	N	N	1.10	3MVS	2.4	0.0									
PCDH15																
EC1-3*	*Hs*	R	N	3.15	6MFO			0.0	1.3	1.7						
EC1-3*	*Hs*	R	N	2.90	6N2E (A)			1.3	0.0	1.5						
EC1-3	*Mm*	N	Y	1.69	6CV7			1.7	1.5	0.0						
EC10-MAD12	*Ss*	R	N	2.09	6BXZ (A)						0.0	0.6	1.5			
EC11-EL	*Mm*	N	Y	1.39	6C10						0.6	0.0	0.7			
EC9-MAD12	*Mm*	N	Y	3.23	6EET						1.5	0.7	0.0			
PCDH1																
EC1-4	*Hs*	R	N	2.85	6BX7									0.0	0.7	0.7
EC1-4	*Hs*	N	Y	3.15	6MGA									0.7	0.0	0.8
EC1-4	*Hs*	N	Y	3.20	6VFP									0.7	0.8	0.0

* *hs* PCDH15 EC1-3 G16D/N369D/Q370N

Movie S1. Forced unbending, unrolling, and unfolding in a simulation of the *hs* PCDH15 EC1-MAD12 ex12a- + CDH23 EC1-2 model. Stretching of the complex at 0.1 nm/ns (simulation S1d in *SI Appendix,* Table 10, 0 – 191.9 ns) results in straightening of the PCDH15 EC9-10 linker region with a twisting of the PCDH15 monomer. As the trajectory continues the PCDH15 EC5-6 and EC9-10 linker regions stretch without unfolding of the repeats. In the final moments of the simulation, PCDH15 MAD12 peels away (unrolls) from EC11 and begins to unfold from the C-terminus without PCDH15 and CDH23 unbinding. Protein is depicted in cartoon representation with a rough surface envelope (PCDH15 – purple; CDH23 – blue). Ca^{2+} ions are shown as green spheres. Water molecules and other atoms are not shown for clarity.

Movie S2. Forced unbending, unrolling, and unfolding in a simulation of the *mm* PCDH15 EC1-MAD12 ex12a+ + *mm* CDH23 EC1-3 model. Stretching of the complex at 0.1 nm/ns (simulation S2d in *SI Appendix,* Table S10, 0 – 251.6 ns) results in straightening of the PCDH15 EC9-10 linker with a twisting of the PCDH15 monomer. Later in the trajectory the PCDH15 EC5-6 and EC9-10 linkers stretch without unfolding of the repeats. The PCDH15 MAD12 peels away from EC11 and begins to unfold from the C-terminus without PCDH15 and CDH23 unbinding as the simulation ends. System shown as in Movie S1.

Movie S3. Forced unbending, unrolling, and unfolding in a simulation of the *mm* PCDH15 EC9-MAD12 dimer. Stretching of the complex at 0.1 nm/ns (simulation S11d in *SI Appendix,* Table 10, 0 – 95.8 ns) results in straightening of the PCDH15 EC9-10 linker regions, followed by unrolling of MAD12 and unfolding at the C-terminus end of PCDH15. System shown as in Movie S1.

Movie S4. Forced unbinding in a simulation of the *hs* (PCDH15 EC1-5 ex12a-)$_2$ + (CDH23 EC1-2)$_2$ model. Stretching of the complex at 0.1 nm/ns (simulation S3d in *SI Appendix,* Table S10, 0 – 95.6 ns) results in straightening of PCDH15 EC3-5 monomers coming into contact, squeezing of CDH23 monomers, and in unbinding of both CDH23 monomers from PCDH15 without unfolding of any EC repeats. The X-dimer interface mediated by PCDH15 EC2-3 was partially disrupted towards the end of the simulation trajectory. System shown as in Movie S1.

Movie S5. Forced unbinding in a simulation of the *mm* (PCDH15 EC1-5 ex12a+)$_2$ + (CDH23 EC1-3)$_2$ model. Stretching of the complex at 0.02 nm/ns (simulation S7e in *SI Appendix,* Table S10, 0 – 500.3 ns) results in straightening of PCDH15 EC3-5 monomers coming into contact, squeezing of CDH23 monomers, and in unbinding of both CDH23 monomers from PCDH15 without unfolding of any EC repeats. The X-dimer interface mediated by PCDH15 EC2-3 was partially disrupted towards the end of the simulation trajectory. System shown as in Movie S1.

Movie S6. Forced unbinding in a simulation of the *hs* (PCDH15 EC1-5 ex12a-)$_2$ + (CDH23 EC1-2)$_2$ model in the absence of Ca^{2+}. Stretching of the complex at 0.1 nm/ns (simulation S6d in *SI Appendix,* Table S10, 0 – 142.9 ns) first resulted in lengthening of all EC linker regions without unfolding of domains. The X-dimer interface mediated by PCDH15 EC2-3 broke before unbinding of CDH23 from PCDH15. The PCDH15 and CDH23 monomers unbound without unfolding of EC repeats at the end of the trajectory. System shown as in Movie S1.

Movie S7. Tour of the *hs* PCDH15 EC1-MAD12 ex12a- + CDH23 EC1-2 model. System is shown first within the solvation box (PCDH15 – purples; CDH23 – blues; Ca^{2+} ions – green; SMD atoms - red). Zoom in details focus on: The PCDH15 + CDH23 interaction with emphasis on a salt bridge (p.R113:p.E77) important for the maintenance of the handshake complex; the PCDH15 EC2-3 X-dimer; the non-canonical PCDH15 EC5-6 linker region; the straightened Ca^{2+}-free PCDH15 EC9-10 linker region; the PCDH15 EC11-MAD12 *cis* dimer; and the ferredoxin fold of MAD12.

Movie S8. Tour of the *mm* PCDH15 EC1-MAD12 ex12a+ + CDH23 EC1-3 model. System is shown first within the solvation box (PCDH15 – purples; CDH23 – blues; Ca^{2+} ions – green; SMD atoms - red). Zoom in details focus on: The interaction between CDH23 EC1 α helices (between β-strands C and D) with emphasis on the "interlocking" salt bridges (p.R53:p.E50) and residues p.E49 that cap the helix dipoles; and the PCDH15 ex12a+ structure highlighting the enlarged BC loop in EC4 (p.V(414+1)PPGGVP(414+7)).

Movie S9. Forced unbending, unrolling, and unfolding in a simulation of the *hs* (PCDH15 EC1-MAD12 ex12a-)$_2$ + (CDH23 EC1-2)$_2$ model. Stretching of the complex at 0.1 nm/ns (simulation S8d in *SI Appendix,* Table S10, 0 – 122.3 ns) results in straightening of the PCDH15 ectodomains with lengthening of the EC5-6 and EC9-10 linker regions. As the simulation progressed the PCDH15 MAD12s began to unfold from their C-terminal ends. The PCDH15 MAD12s eventually unrolled away from EC11 while unfolding continued. The CDH23 monomers did not unbind from PCDH15. System shown as in Movie S1.

Movie S10. Forced unbending, unrolling, and unfolding in a simulation of the *mm* (PCDH15 EC1-MAD12 ex12a+)$_2$ + (CDH23 EC1-3)$_2$ model. Stretching of the complex at 0.1 nm/ns (simulation S9d in *SI Appendix,* Table S10, 0 – 135.5 ns) results in straightening of the PCDH15 ectodomains with lengthening of the EC5-6 and EC9-10 linker regions. As the simulation progressed the PCDH15 MAD12s began to unfold from their C-terminal ends. The PCDH15 MAD12s eventually unrolled away from EC11 while unfolding continued rather symmetrically. The CDH23 monomers did not unbind from PCDH15. System shown as in Movie S1.

Movie S11. Forced unbending, unrolling, and unfolding in a simulation of the *mm* (PCDH15 EC1-MAD12 ex12a+)$_2$ + (CDH23 EC1-3)$_2$ model. Stretching of the complex at 0.02 nm/ns (simulation S9e in *SI Appendix,* Table S10, 0 – 555.8 ns) results in straightening of the PCDH15 ectodomains with lengthening of the EC5-6 and EC9-10 linker regions. As the simulation progressed the PCDH15 MAD12s began to unfold from their C-terminal ends. The PCDH15 MAD12s eventually unrolled away from EC11 while unfolding continued, with each domain following different unrolling and unfolding pathways (asymmetric). The CDH23 monomers did not unbind from PCDH15. System shown as in Movie S1.

Movie S12. Forced unbending, unrolling, and unbinding in a simulation of the *mm* PCDH15 EC1-MAD12 ex12a+ + CDH23 EC1-3 model. Complex is stretched at 1 nm/ns by applying forces to the center of mass of MAD12 Cα atoms (simulation S2f in *SI Appendix,* Table S10, 0 – 30.6 ns). Straightening of the PCDH15 ectodomains with lengthening of the EC5-6 and EC9-10 linker regions is observed. As the simulation progressed the PCDH15 MAD12 began to unroll, with subsequent unbinding of the CDH23 monomer from PCDH15. C-terminal end of PCDH15 is in a non-physiological orientation at the end of the simulation. System shown as in Movie S1.

Movie S13. Forced unbending, unrolling, and unbinding in a simulation of the *mm* (PCDH15 EC1-MAD12 ex12a+)$_2$ + (CDH23 EC1-3)$_2$ model. Complex is stretched at 1 nm/ns by applying forces to the center of mass of MAD12s Cα atoms (simulation S9g in *SI Appendix,* Table S10, 0 – 22.9 ns). Straightening of the PCDH15 ectodomains with lengthening of the EC5-6 and EC9-10 linker regions is observed. As the simulation progressed the PCDH15 MAD12s began to unroll with subsequent unbinding of the CDH23 monomers from PCDH15. C-terminal ends of PCDH15 are in a non-physiological orientation at the end of the simulation. System shown as in Movie S1.

SI References

1. Otwinowski Z, Minor W (1997) Processing of X-ray diffraction data. *Methods Enzym* 276:307–326.
2. McCoy AJ, et al. (2007) Phaser crystallographic software. *J Appl Crystallogr* 40(4):658–674.
3. Sotomayor M, Weihofen WA, Gaudet R, Corey DP (2012) Structure of a force-conveying cadherin bond essential for inner-ear mechanotransduction. *Nature* 492(7427):128–32.
4. Powers RE, Gaudet R, Sotomayor M (2017) A Partial Calcium-Free Linker Confers Flexibility to Inner-Ear Protocadherin-15. *Structure* 25(3):482–495.
5. De-la-Torre P, Choudhary D, Araya-Secchi R, Narui Y, Sotomayor M (2018) A Mechanically Weak Extracellular Membrane-Adjacent Domain Induces Dimerization of Protocadherin-15. *Biophys J* 115(12):2368–2385.
6. Araya-Secchi R, Neel BL, Sotomayor M (2016) An elastic element in the protocadherin-15 tip link of the inner ear. *Nat Commun* 7:13458.
7. Emsley P, Lohkamp B, Scott WG, Cowtan K (2010) Features and development of Coot. *Acta Crystallogr D Biol Crystallogr* 66(Pt 4):486–501.
8. Murshudov GN, et al. (2011) REFMAC5 for the refinement of macromolecular crystal structures. *Acta Crystallogr Sect D Biol Crystallogr* 67(4):355–367.
9. Laskowski RA, MacArthur MW, Moss DS, Thornton JM, IUCr (1993) PROCHECK: a program to check the stereochemical quality of protein structures. *J Appl Crystallogr* 26(2):283–291.
10. Hooft RWW, Vriend G, Sander C, Abola EE (1996) Errors in protein structures. *Nature* 381(6580):272–272.
11. Zheng H, et al. (2014) Validation of metal-binding sites in macromolecular structures with the CheckMyMetal web server. *Nat Protoc* 9(1):156–170.
12. Dyer KN, et al. (2014) High-throughput SAXS for the characterization of biomolecules in solution: a practical approach. *Methods Mol Biol* 1091:245–258.
13. Classen S, et al. (2013) Implementation and performance of SIBYLS: a dual endstation small-angle X-ray scattering and macromolecular crystallography beamline at the Advanced Light Source. *J Appl Crystallogr* 46(Pt 1):1–13.

14. Rambo RP, Tainer JA (2011) Characterizing flexible and intrinsically unstructured biological macromolecules by SAS using the Porod-Debye law. *Biopolymers* 95(8):559–571.
15. Konarev P V, Volkov V V, Sokolova A V, Koch MHJ, Svergun DI (2003) PRIMUS: A Windows PC-based system for small-angle scattering data analysis. *J Appl Crystallogr* 36(5):1277–1282.
16. Franke D, et al. (2017) *ATSAS 2.8* : a comprehensive data analysis suite for small-angle scattering from macromolecular solutions. *J Appl Crystallogr* 50(4):1212–1225.
17. Svergun DI (1992) Determination of the Regularization Parameter in Indirect- Transform Methods Using Perceptual Criteria. *J Appl Crystallogr* 25(4):495–503.
18. Fischer H, de Oliveira Neto M, Napolitano HB, Polikarpov I, Craievich AF (2010) Determination of the molecular weight of proteins in solution from a single small-angle X-ray scattering measurement on a relative scale. *J Appl Crystallogr* 43(1):101–109.
19. Panjkovich A, Svergun DI (2016) Deciphering conformational transitions of proteins by small angle X-ray scattering and normal mode analysis. *Phys Chem Chem Phys* 18(8):5707–19.
20. Schneidman-Duhovny D, Hammel M, Tainer JA, Sali A (2013) Accurate SAXS profile computation and its assessment by contrast variation experiments. *Biophys J* 105(4):962–974.
21. Dam J, Velikovsky CA, Mariuzza RA, Urbanke C, Schuck P (2005) Sedimentation velocity analysis of heterogeneous protein-protein interactions: Lamm equation modeling and sedimentation coefficient distributions c(s). *Biophys J* 89(1):619–34.
22. Schuck P (2000) Size-Distribution Analysis of Macromolecules by Sedimentation Velocity Ultracentrifugation and Lamm Equation Modeling. *Biophys J* 78(3):1606–1619.
23. Zhao H, Brautigam CA, Ghirlando R, Schuck P (2013) Overview of Current Methods in Sedimentation Velocity and Sedimentation Equilibrium Analytical Ultracentrifugation. *Curr Protoc Protein Sci* 71(1):20.12.1-20.12.49.
24. Brautigam CA (2015) Calculations and Publication-Quality Illustrations for Analytical Ultracentrifugation Data. *Methods in Enzymology*, pp 109–133.
25. Humphrey W, Dalke A, Schulten K (1996) VMD: Visual molecular dynamics. *J Mol Graph* 14(1):33–38.
26. Jaiganesh A, et al. (2018) Zooming in on Cadherin-23: Structural Diversity and Potential Mechanisms of Inherited Deafness. *Structure*. doi:10.1016/j.str.2018.06.003.
27. Bosher SK, Warren RL (1978) Very low calcium content of cochlear endolymph, an extracellular fluid. *Nature* 273(5661):377–378.
28. Salt AN, Inamura N, Thalmann R, Vora A (1989) Calcium gradients in inner ear endolymph. *Am J Otolaryngol* 10(6):371–5.
29. Strimbu CE, Prasad S, Hakizimana P, Fridberger A (2019) Control of hearing sensitivity by tectorial membrane calcium. *Proc Natl Acad Sci*:201805223.
30. Sotomayor M, Weihofen WA, Gaudet R, Corey DP (2010) Structural Determinants of Cadherin-23 Function in Hearing and Deafness. *Neuron* 66(1):85–100.
31. Phillips JC, et al. (2005) Scalable molecular dynamics with NAMD. *J Comput Chem* 26(16):1781–1802.
32. Huang J, MacKerell ADJ (2014) CHARMM36 all-atom additive protein force field: Validation based on comparison to NMR data. *J Comput Chem* 34(25):2135–2145.
33. Isralewitz B, Baudry J, Gullingsrud J, Kosztin D, Schulten K (2001) Steered Molecular Dynamics Investigations of Protein Function. *J Mol Graph Model* 19:13–25.
34. Grubmüller H (2005) Force probe molecular dynamics simulations. *Methods Mol Biol* 305:493–515.
35. Sotomayor M, Schulten K (2007) Single-molecule experiments in vitro and in silico. *Science* 316(5828):1144–1148.
36. Franz F, Daday C, Gräter F (2020) Advances in molecular simulations of protein mechanical properties and function. *Curr Opin Struct Biol* 61:132–138.
37. Larkin MA, et al. (2007) Clustal W and Clustal X version 2.0. *Bioinformatics* 23(21):2947–2948.
38. Kearse M, et al. (2012) Geneious Basic: an integrated and extendable desktop software platform for the organization and analysis of sequence data. *Bioinformatics* 28(12):1647–9.
39. Waterhouse AM, Procter JB, Martin DMA, Clamp M, Barton GJ (2009) Jalview Version 2--a multiple sequence alignment editor and analysis workbench. *Bioinformatics* 25(9):1189–1191.
40. Garcia-Boronat M, Diez-Rivero CM, Reinherz EL, Reche PA (2008) PVS: a web server for protein sequence variability analysis tuned to facilitate conserved epitope discovery. *Nucleic Acids Res* 36(Web Server):W35–W41.
41. Anfinsen CB (1973) Principles that Govern the Folding of Protein Chains. *Science (80-)* 181(4096):223–230.
42. Elledge HM, et al. (2010) Structure of the N terminus of cadherin 23 reveals a new adhesion mechanism for a subset of cadherin superfamily members. *Proc Natl Acad Sci U S A* 107(23):10708–10712.
43. Dionne G, et al. (2018) Mechanotransduction by PCDH15 Relies on a Novel cis-Dimeric Architecture. *Neuron* 99(3):480-492.e5.

44. Modak D, Sotomayor M (2019) Identification of an adhesive interface for the non-clustered δ1 protocadherin-1 involved in respiratory diseases. *Commun Biol* 2(1):354.
45. Harrison OJ, et al. (2020) Family-wide Structural and Biophysical Analysis of Binding Interactions among Non-clustered δ-Protocadherins. *Cell Rep* 30(8):2655-2671.e7.
46. Brasch J, et al. (2011) Structure and binding mechanism of vascular endothelial cadherin: a divergent classical cadherin. *J Mol Biol* 408(1):57–73.
47. Ge J, et al. (2018) Structure of mouse protocadherin 15 of the stereocilia tip link in complex with LHFPL5. *Elife* 7. doi:10.7554/eLife.38770.
48. Zheng QY, et al. (2006) A new spontaneous mutation in the mouse protocadherin 15 gene. *Hear Res* 219(1–2):110–120.
49. Alagramam KN, et al. (2011) Mutations in Protocadherin 15 and Cadherin 23 Affect Tip Links and Mechanotransduction in Mammalian Sensory Hair Cells. *PLoS One* 6(4):e19183.
50. Zhan Y, Liu M, Chen D, Chen K, Jiang H (2015) Novel mutation located in EC7 domain of protocadherin-15 uncovered by targeted massively parallel sequencing in a family segregating non-syndromic deafness DFNB23. *Int J Pediatr Otorhinolaryngol* 79(7):983–6.
51. Bartsch TF, et al. (2019) Elasticity of individual protocadherin 15 molecules implicates tip links as the gating springs for hearing. *Proc Natl Acad Sci* 116(22):11048–11056.
52. Ahmed ZM, et al. (2003) PCDH15 is expressed in the neurosensory epithelium of the eye and ear and mutant alleles are responsible for both USH1F and DFNB23. *Hum Mol Genet* 12(24):3215–23.
53. Kazmierczak P, et al. (2007) Cadherin 23 and protocadherin 15 interact to form tip-link filaments in sensory hair cells. *Nature* 449(7158):87–91.
54. Geng R, et al. (2013) Noddy, a mouse harboring a missense mutation in protocadherin-15, reveals the impact of disrupting a critical interaction site between tip-link cadherins in inner ear hair cells. *J Neurosci* 33(10):4395–404.
55. Ahmed ZM, et al. (2008) Gene structure and mutant alleles of PCDH15: nonsyndromic deafness DFNB23 and type 1 Usher syndrome. *Hum Genet* 124(3):215–223.
56. Hazra JP, et al. (2019) Broken force dispersal network in tip-links by the mutations at the Ca^{2+} -binding residues induces hearing-loss. *Biochem J* 476(16):2411–2425.
57. Chen D, et al. (2015) Mutation in PCDH15 may modify the phenotypic expression of the 7511T>C mutation in MT-TS1 in a Chinese Han family with maternally inherited nonsyndromic hearing loss. *Int J Pediatr Otorhinolaryngol* 79(10):1654–1657.
58. Yang T, Wei X, Chai Y, Li L, Wu H (2013) Genetic etiology study of the non-syndromic deafness in Chinese Hans by targeted next-generation sequencing. *Orphanet J Rare Dis* 8(1):85.
59. Doucette L, et al. (2009) Profound, prelingual nonsyndromic deafness maps to chromosome 10q21 and is caused by a novel missense mutation in the Usher syndrome type IF gene PCDH15. *Eur J Hum Genet* 17(5):554–64.
60. Miyagawa M, Naito T, Nishio S, Kamatani N, Usami S (2013) Targeted exon sequencing successfully discovers rare causative genes and clarifies the molecular epidemiology of Japanese deafness patients. *PLoS One* 8(8):e71381.
61. Schrauwen I, et al. (2018) Novel digenic inheritance of PCDH15 and USH1G underlies profound non-syndromic hearing impairment. *BMC Med Genet* 19(1):122.
62. Grossman SR, et al. (2010) A composite of multiple signals distinguishes causal variants in regions of positive selection. *Science (80-)* 327(5967):883–886.
63. Saleha S, Ajmal M, Jamil M, Nasir M, Hameed A (2016) In silico analysis of a disease-causing mutation in PCDH15 gene in a consanguineous Pakistani family with Usher phenotype. *Int J Ophthalmol* 9(5):662–8.
64. Oroz J, et al. (2019) Nanomechanics of tip-link cadherins. *Sci Rep* 9(1):13306.
65. Sotomayor M, Corey DP, Schulten K (2005) In search of the hair-cell gating spring: Elastic properties of ankyrin and cadherin repeats. *Structure* 13(4):669–682.
66. Sotomayor M, Schulten K (2008) The allosteric role of the Ca2+ switch in adhesion and elasticity of C-cadherin. *Biophys J* 94(12):4621–4633.
67. Howard J, Hudspeth AJ (1988) Compliance of the hair bundle associated with gating of mechanoelectrical transduction channels in the bullfrog's saccular hair cell. *Neuron* 1(3):189–199.
68. Bartsch TF, Hudspeth AJ (2018) A New Twist on Tip Links. *Neuron* 99(3):423–425.
69. Jaramillo F, Hudspeth AJ (1993) Displacement-clamp measurement of the forces exerted by gating springs in the hair bundle. *Proc Natl Acad Sci U S A* 90(4):1330–4.
70. Shepherd GM, Corey DP (1994) The extent of adaptation in bullfrog saccular hair cells. *J Neurosci* 14(10):6217–29.
71. Holt JR, Corey DP, Eatock RA (1997) Mechanoelectrical transduction and adaptation in hair cells of the mouse utricle, a low-frequency vestibular organ. *J Neurosci* 17(22):8739–48.

72. Vollrath MA, Eatock RA (2003) Time course and extent of mechanotransducer adaptation in mouse utricular hair cells: comparison with frog saccular hair cells. *J Neurophysiol* 90(4):2676–89.
73. Corey DP, Sotomayor M (2004) Hearing: Tightrope act. *Nature* 428(6986):901–903.
74. Howard J, Bechstedt S (2004) Hypothesis: A helix of ankyrin repeats of the NOMPC-TRP ion channel is the gating spring of mechanoreceptors. *Curr Biol* 14(6):R224–R226.
75. Lee G, et al. (2006) Nanospring behaviour of ankyrin repeats. *Nature* 440(7081):246–249.
76. Tang Y-Q, et al. (2020) Ankyrin Is An Intracellular Tether for TMC Mechanotransduction Channels. *Neuron*. doi:10.1016/j.neuron.2020.03.026.
77. Cheung ELM, Corey DP (2006) Ca2+ Changes the Force Sensitivity of the Hair-Cell Transduction Channel. *Biophys J* 90(1):124–139.
78. Robles L, Ruggero MA (2001) Mechanics of the mammalian cochlea. *Physiol Rev* 81(3):1305–1352.
79. Lee HY, et al. (2016) Two-Dimensional Cochlear Micromechanics Measured In Vivo Demonstrate Radial Tuning within the Mouse Organ of Corti. *J Neurosci* 36(31):8160–73.
80. Fridberger A, Tomo I, Ulfendahl M, Boutet de Monvel J (2006) Imaging hair cell transduction at the speed of sound: Dynamic behavior of mammalian stereocilia. *Proc Natl Acad Sci* 103(6):1918–1923.
81. Wang Y, Puria S, Steele CR, Ricci AJ (2018) Inner hair cell stereocilia movements captured in-situ by a high-speed camera with subpixel image processing. *AIP Conference Proceedings* (AIP Publishing LLC), p 120004.
82. Evans E, Ritchie K (1997) Dynamic strength of molecular adhesion bonds. *Biophys J* 72(4):1541–1555.
83. Lee EH, Hsin J, Sotomayor M, Comellas G, Schulten K (2009) Discovery through the computational microscope. *Structure* 17(10):1295–306.
84. Rico F, Gonzalez L, Casuso I, Puig-Vidal M, Scheuring S (2013) High-speed force spectroscopy unfolds titin at the velocity of molecular dynamics simulations. *Science* 342(6159):741–743.
85. Dudko OK (2015) Decoding the mechanical fingerprints of biomolecules. *Q Rev Biophys*:1–14.
86. Sheridan S, Gräter F, Daday C (2019) How Fast Is Too Fast in Force-Probe Molecular Dynamics Simulations? *J Phys Chem B* 123(17):3658–3664.
87. Rzadzinska AK, Steel KP (2009) Presence of interstereocilial links in waltzer mutants suggests Cdh23 is not essential for tip Link formation. *Neuroscience* 158(2):365–368.
88. Indzhykulian AA, et al. (2013) Molecular Remodeling of Tip Links Underlies Mechanosensory Regeneration in Auditory Hair Cells. *PLoS Biol* 11(6):e1001583.
89. Narui Y, Sotomayor M (2018) Tuning Inner-Ear Tip-Link Affinity Through Alternatively Spliced Variants of Protocadherin-15. *Biochemistry* 57(11):acs.biochem.7b01075.
90. Tobin M, Chaiyasitdhi A, Michel V, Michalski N, Martin P (2019) Stiffness and tension gradients of the hair cell's tip-link complex in the mammalian cochlea. *Elife* 8. doi:10.7554/eLife.43473.